We shall not cease from exploration
And the end of our exploring
Will be to arrive where we started
And know the place for the first time.

What we call the beginning is often the end
And to make an end is to make a beginning
The end is where we start from.

T. S. Eliot,
Little Gidding

THE USE OF EMISSION-TRANSMISSION COMPUTED TOMOGRAPHY FOR IMPROVED QUANTIFICATION IN SPECT

Mercedes Rodríguez Villafuerte

UNIVERSITY COLLEGE LONDON

Submitted for
The Degree of Doctor of Philosophy
The University of London

June 1994

Abstract

The attenuation of photons within the body has been recognised as the major limiting factor hindering the ability of single photon emission computed tomography (SPECT) as a quantitative technique. This thesis investigates several aspects of an emission-transmission SPECT system using the Monte Carlo method and experimental techniques. The system was based on a rotating gamma camera fitted with a parallel hole collimator.

The simulation of a transmission study was performed using a simple non-uniform mathematical phantom with two different external sources, a collimated line source and a flood source. The results showed that the attenuation maps were highly dependent on the geometry and photon energy of the source. The collimated line source produced improved image quality with lower statistical noise than the flood source. The results showed that, when high atomic number elements are present in the tissue composition, the attenuation coefficients at different energies are related through a second order polynomial transformation. If the object under study is formed of soft tissue equivalent materials, a linear transformation holds.

The attenuation maps generated in the transmission study were used to correct for non-uniform attenuation compensation of an emission phantom. The results showed that non-uniform attenuation compensation improved image quality and reduced noise when compared to data without attenuation compensation. The presence of scattered photons in the emission data reduced the quality of the images and precluded accurate quantification. Absolute quantification was performed using the percent air sensitivity criterion. The largest difference between the theoretical and the Monte Carlo simulated images was approximately 8%.

An emission-transmission myocardial perfusion study was simulated using an anthropomorphic phantom. Two photon energies of clinical interest were used, 75 keV and 140 keV, corresponding to the main photon emission energies of ^{201}Tl and ^{99m}Tc. The results showed that ^{99m}Tc provided better image quality than ^{201}Tl. Non-uniform attenuation compensation produced a very good agreement between the theoretical prediction and the simulation when scatter-free data were considered.

The results presented in this thesis indicate that it is not possible to accomplish accurate attenuation compensation in general situations if scatter correction is not applied.

Errata

p.17	l.34	for "data is" read "data are"
p.23	l.20	for "septa" read "septum"
p.27	l.14	for "no a preferential" read "no preferred"
p.28	l.8	for "type interaction" read "type of interaction"
p.29	l.27	and elsewhere for "*et at*" read "*et al*"
p.34	l.29	for "interactive" read "iterative"
p.38	l.30	for "indexes" read "indices"
p.41	l.1	for "there is not analytic" read "there is no analytical"
p.43	eq.1.13	should read $A_{ij}^{km} = \exp\left(- \sum_{b_{ij}}^{\text{detector}} \mu_{i'j'} l_{i'j'}^{km} \right)$
	l.13, l.14	should read "attenuation compensation is not requested, the attenuation factors in equation 1.13 are set as unity as μ_{ij}=0"
	l.16	for "constrains" read "constraints"
p.44	l.1, l.2	for "constrain" read "constraint"
p.48	l.12, l.13	for "data is" read "data are"
p.51	l.2	for "algorithms before" read "algorithms described before"
p.52	l.12	for "with" read "within"
p.67	l.31	for "than the" read "than that"
p.73	l.4	for "FWHM" read "FWHMs"
p.79	l.16	for "in less" read "by less"
p.80	l.12	for "does no" read "does not"
p.86	l.5	for "on the energy of the" read "on the"
	l.9, l.10	for "in detected primary photons in" read "of detected primary photons by"
p.95	l.15	for "mean free path" read "free path length"
p.110	l.8	delete last sentence starting at "According to ..."
p.113	l.5	for "which characterise" read "which are characterised"
p.120	l.12	for "indication on" read "indication of"
p.126	l.10	for "to scale the" read "the scaling of"
p.150	l.21	for "in approximately" read "by approximately"
p.156	f.6.2	coordinates have been interchanged
p.174	l.17	for "investigation on" read "investigation of"
p.175	l.19	for "to register the" read "registration of the"
p.188	l.25	for "Adison" read "Addison"
p.190	l.30	for "EUR" read "*EUR*"
p.191	l.28	for "EUR" read "*EUR*"

Figures

CHAPTER 1

CHAPTER 2

CHAPTER 3

CHAPTER 4

CHAPTER 5

CHAPTER 6

APPENDIX 1

APPENDIX 2

Tables

CHAPTER 1

CHAPTER 2

CHAPTER 3

CHAPTER 4

CHAPTER 5

CHAPTER 6

Acknowledgements

I would like to thank Dr. Robert Speller for his supervision over the duration of this project. I am very much indebted to Dr. Ian Cullum for his helpful suggestions and advice. Thanks also to my numerous colleagues Mike Mooney, Nia Harrison, Gary Royle, Mike Doherty and Cephas Mubata, most of them doctors now, for their friendship and help during my stay in England. Many thanks to Dave Plummer for providing the software for image display and analysis and for all his helpful computing suggestions.

I very much appreciate the help I received from, and the useful discussions with Dr. Benjamin Tsui, Dr. David Lalush and Dr. Eric Frey of the University of North Carolina at Chapel Hill. Thanks also to them for providing the reconstruction programs used in this thesis.

Thanks to my parents Cecilio y Maria de Lourdes for all their effort and continuous support throughout the duration of my 20 years of study.

I must also thank Arnulfo for his encouragement and loving care during the most important years of my life.

Finally, I would like to thank the National Autonomous University of Mexico for the scholarship I received during my graduate studies.

Introduction

Single photon emission computed tomography, SPECT, is a well-established diagnostic technique in nuclear medicine departments. SPECT produces three-dimensional tomographic images of *in-vivo* radionuclide distributions by detecting the decay products (γ or x-ray photons) at different positions around the patient. Image reconstruction of selected planes within the patient is performed using sophisticated mathematical algorithms. The most important characteristic of this technique is its ability to provide information on the metabolic processes taking place within the organ or organ system where the radionuclide uptake occurs.

The ultimate goal of SPECT imaging is to produce cross sectional images with picture element values (pixels, each of which represents a small part of the image) directly proportional to the activity concentration in the corresponding region of the patient. The accurate determination of activity concentrations would lead to a better determination of the dimensions of regions of interest and radioactive uptake; these are necessary to improve clinical diagnosis. Unfortunately, this is difficult to achieve in practice since several physical and technical factors degrade the acquired data usually resulting in reconstructed images whose pixel values do not represent the true activity concentrations.

One of the most important factors that hinders the ability of SPECT imaging to produce quantitative data is the loss of primary photon flux reaching the detector due to absorption or scatter within the patient. This phenomenon is known as photon attenuation and it results in a decreased number of counts and, in some cases, artefacts within the reconstructed images. The degree of attenuation depends on the energy of the emitted photons, the location of the source and the anatomy of the body where the source is embedded. Unfortunately, deterioration of the images due to photon attenuation is difficult to correct because the location and intensity of the source distribution and the structure and composition of the attenuating medium are usually unknown.

Several attenuation compensation methods that correct very accurately for this phenomenon have been developed previously for objects which are both uniform and symmetric (Budinger and Gullberg 1974, Kay and Keyes 1975, Chang 1978, Budinger

et al 1979). In order to apply these algorithms, it is necessary to determine first the geometry of the patient (calculated from an assumed or measured body contour) and the value of the linear attenuation coefficient which is assumed to be constant through the patient. Compensation algorithms for uniform-attenuation have been applied to study regions of the body where the assumption of uniformity holds (like the brain or abdomen) with a great deal of success.

Photon attenuation in regions with large variations in attenuation coefficients (like the thorax) can produce seriously distorted images leading to difficult or erroneous interpretation. It is clear that attenuation correction algorithms for uniform attenuation cannot be used in these cases and more appropriate methods must be used. Thallium 201 SPECT myocardial imaging is a non-invasive nuclear medicine technique to diagnose the presence of lesions in the myocardium and to specify their location. This type of examination is one of the imaging techniques most affected by photon attenuation, because:

a) Thallium-201 is the most suitable isotope to use as it is efficiently extracted by the myocardium due to its biochemical properties which are similar to potassium. On decay, the major emissions of ^{201}Tl are x-rays of the daughter product mercury-201, with an energy range of 69 to 81 keV. At these low energies, only 3.4 cm of soft tissue are necessary to reduce the photon intensity to half its initial value. Therefore, it is expected that a large fraction of photons would be absorbed within the patient before detection.

b) The thorax contains several tissues arranged in a complex structure which have a large variation in attenuation coefficients. Photon absorption and scatter are phenomena highly dependent on the atomic number and density of the elements forming the tissues. These effects produce different degrees of attenuation not only as function of source depth but also as function of tissue composition.

These two factors increase the effects of photon attenuation in the thorax and the use of a suitable attenuation compensation technique is highly desirable.

Non-uniform attenuation compensation methods have also been developed (Huesman *et al* 1977, Chang 1978, Lange and Carson 1984) and are still under investigation. In order to apply any of these methods, it is necessary first to determine the location, size and composition of the attenuating media. This requires acquisition of two tomographic studies; a transmission study (to determine the attenuation coefficients) and an emission study (to determine the source distribution). The transmission data is

used to correct the emission image for attenuation. The transmission study can be performed with a rotating gamma camera and an external source using a standard transmission computed tomographic (CT) technique. The geometry of the external source can be such as to generate attenuation coefficients with or without scatter contribution (normally referred to as broad or narrow beam geometry). The attenuation coefficients can be produced with a different photon energy to the emission study. However, if this is the case, a transformation must be applied to generate the appropriate attenuation coefficients at the required emission energy. To date, mainly experimental work has been done to assess the performance of non-uniform attenuation compensation methods. Theoretical approaches have been avoided largely due to the extensive computational effort and difficulty required to perform such studies.

This thesis investigates the theoretical assessment of several aspects of an emission-transmission computed tomography system using both the Monte Carlo method and experimental techniques. Photon interactions with matter are processes well understood either theoretically and/or experimentally and the probability laws that govern their occurrence are well known. The Monte Carlo method is a mathematical technique that makes use of these probabilities and, in conjunction with a large supply of random numbers, simulates what occurs in nature. In the Monte Carlo method each photon can be traced from its point of origin to its detection and photon interactions within the medium can be simulated accurately. The major advantage of this technique is that it allows the accurate investigation of certain phenomena which are difficult, if not impossible, to study experimentally.

The major aims of this thesis can be summarised as follows:

i) Development and testing of a Monte Carlo simulation of an emission-transmission tomographic system based on a rotating gamma camera fitted with a parallel hole collimator of hexagonal holes.

ii) Investigation of the performance of different external radioactive sources used in the determination of attenuation maps.

iii) Determination of the attenuation coefficients of several media as a function of photon energy.

iv) Assessment of the performance of an iterative non-uniform attenuation correction algorithm with a simulated phantom study.

v) Assessment of the performance of an iterative non-uniform attenuation correction algorithm with a Monte Carlo simulation of a myocardial study.

The organisation of the thesis is as follows:

Chapter one reviews the basic aspects of SPECT imaging performed with an Anger gamma camera. The factors that affect quantification in SPECT are described, paying particular attention to the photon attenuation problem. Attenuation compensation techniques for uniform and non-uniform objects are discussed and reviewed. Some of the methodology used throughout the thesis is also presented in this chapter.

The detection process of the gamma camera was not included in the Monte Carlo code; instead an analytical approach was used and implemented in the simulation of the tomographic system. To achieve this, the energy response was characterised with an analytical expression and the intrinsic spatial resolution with a digital representation of the point spread function. These two approaches were based on experimental measurements of the intrinsic response of the gamma camera and are described in Chapter two.

The Monte Carlo simulation of a parallel hole collimator of hexagonal holes is described in Chapter three. As any Monte Carlo simulation is subject to programming errors it is very important to validate the code either theoretically or experimentally. In order to achieve this, results of the Monte Carlo program assuming an ideal detector response are compared with the analytical expressions for the collimator spatial resolution and geometric response. The simulation of photon transport within a phantom and collimator is also shown and the results are compared with experimental measurements.

Chapter four describes the Monte Carlo simulation of a transmission tomographic system combining the techniques described in Chapters two and three. Two external source geometries are simulated and a simple phantom is used to investigate the type of attenuation coefficients they can generate. A mathematical relationship between the attenuation coefficients at different energies is found.

Chapter five presents the simulation of an emission study based on the phantom used in Chapter four. Assessment of non-uniform attenuation compensation is presented in terms of relative and absolute quantification of activity concentrations.

A simulation of a tomographic myocardial study based on a realistic human geometry is presented in Chapter six. Transmission and emission simulations are presented and the results combined to correct for non-uniform attenuation compensation. Relative quantification is performed to assess the attenuation compensation algorithm.

Finally, Chapter seven presents the conclusions drawn from the present work together with a discussion of suggested future work.

CHAPTER 1

The Principles of SPECT Imaging

This chapter reviews the basic aspects of single photon emission computed tomography (SPECT) performed with a rotating gamma camera. The factors degrading the acquired information, the mathematical formulation of the image acquisition and the solutions proposed to obtain quantitative data are briefly described. Some of the methodology used throughout the thesis is also developed in this chapter.

1.1. Radionuclide Imaging

Radionuclide imaging arose as a novel technique in the late 1950s with the appearance of the Anger camera (Anger 1958). The success of this clinical tool can be explained in terms of its potential of demonstrating function rather than anatomy. Images are formed with electromagnetic radiation (mainly gamma rays) emitted from radionuclides in the patients' body. The radionuclides are incorporated into radiopharmaceuticals and administered to the patient through injection or inhalation; they are then metabolised or incorporated into the human tissue under study. The technique enables the metabolic pathway of the pharmaceutical to which the radionuclide has been attached (labelled) to be followed.

Two methods of data acquisition have evolved since the introduction of the gamma camera:

Planar imaging refers to the acquisition of single view images consisting of two-dimensional representations or projections of the three-dimensional activity distribution onto the detector field of view. Planar imaging presents the difficulty of determining clearly the function of a tissue in the body mainly due to the superposition of information in a single planar view. This effect results in a reduced tissue (or object) contrast due to the sum of overlying and underlying activity around the tissue of interest.

Single photon emission computed tomography (SPECT) produces images of source distributions in a cross section or slice through the body long axis. SPECT overcomes the problem encountered in planar imaging by providing a true three-dimensional representation of the object under study. The tissue contrast is preserved except for the degrading factors of spatial resolution, scatter, attenuation and noise. The most commonly used SPECT device is a rotating gamma camera fitted with a parallel hole collimator. The image acquisition is performed by rotating the camera around a point (centre of rotation) located within a stationary patient. The multi-view image acquisition is normally achieved by covering an angular range of 360° or 180° (at equal angular steps) in a circular, elliptical or body contour orbit. Transverse tomographic images perpendicular to the gamma camera are then reconstructed by using mathematical algorithms normally adapted from transmission tomography techniques. SPECT imaging with a gamma camera produces multiple slices from just one data acquisition sequence due to the large field of view of the detector.

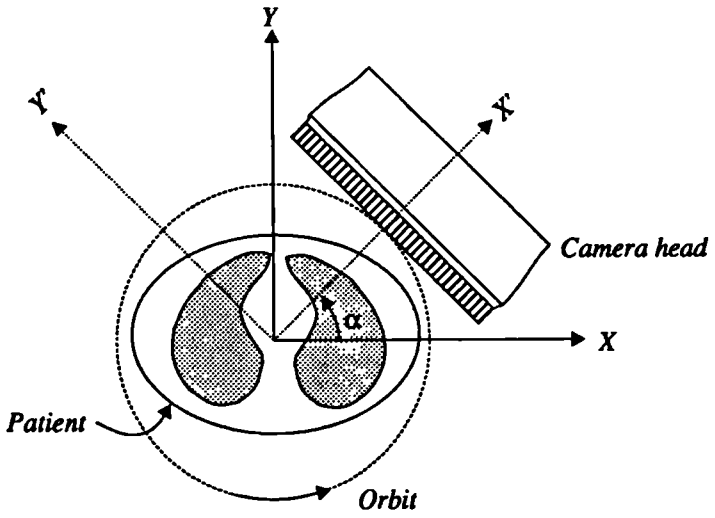

Figure 1.1. Positioning of the gamma camera during tomographic data acquisition.

1.1.1. The Gamma Camera

The Anger gamma camera has been the most successful detector during the last three decades for performing radioisotope imaging. The first camera design included a lead shield with a pinhole aperture, a flat thallium-activated sodium iodide crystal, seven photomultiplier tubes and suitable electronics to convert the signals from the photomultipliers into point flashes of light displayed on a cathode-ray oscilloscope (Anger 1958). Modern gamma cameras still rely on the same principles as Anger's

original design. Technological advances have permitted considerable improvements in the performance of gamma camera components and, at the same time, have allowed the inclusion of a computer system to process the data.

The gamma camera provides essentially two functions: detection of single photon events and determination of their position and energy. Photons emitted during radionuclide decay are converted into a light pulse and subsequently into a voltage signal. This signal is used to form a two-dimensional image (or projection) of the three-dimensional spatial distribution of the radionuclide. The basic components of the gamma camera system are (see figure 1.2): collimator, scintillation crystal, an array of photomultiplier tubes (PMTs), a pulse height analyser and analogue electronics for position encoding.

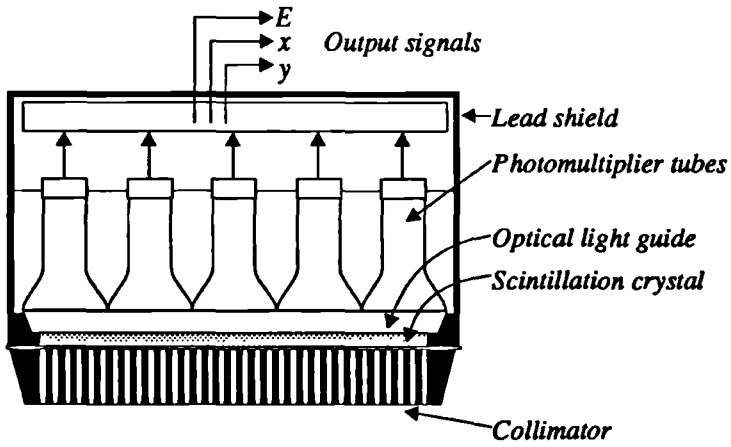

Figure 1.2. Schematic diagram of Anger gamma camera.

Because photon emission is isotropic, there is no preferential photon direction during radioactive decay. However, the formation of an image requires that the photons emitted in the source arrive at the detector in a predictable manner. This is achieved by placing a collimator between the patient and the scintillation crystal. The function of the collimator is to select only those photons travelling towards the detector in a particular direction. Collimators are plates of very high atomic material (e.g. lead) with holes through it; the wall of material between the holes is referred to as septa. Ideally, only those photons that travel along the collimator hole orientation will be detected by the scintillation crystal, while those that approach from any other direction will hit the septa and be absorbed. Therefore, the construction of the collimator requires the use of a high atomic number material to assure high photoelectric absorption efficiency. Septal thickness is chosen to prevent gamma rays from crossing from one hole to the next, keeping penetration to a minimum level. Unfortunately, this technique is an

inherently inefficient method for utilising radiation because most of the potentially useful photons travelling towards the detector are stopped by the collimator.

The scintillation detector converts the energy from an incident gamma photon to visible light. This light, whose yield is proportional to the energy absorbed from the incident photon, is then used to eject photoelectrons from the photocathode of the PMT to generate a signal. The scintillation crystal is a single, large area block (up to 60 cm diameter) of Thallium-activated Sodium Iodide (NaI(Tl)); its high atomic number and density make this crystal a very good photon absorber. Besides, it gives high light output per unit input energy giving good energy resolution properties and, because the crystal is highly transparent to its own light emission, the light losses due to absorption are minimal. NaI(Tl) suffers the drawbacks of being expensive to produce as a large crystal, fragile and so needing protection from both thermal and mechanical stresses. The crystal is also hygroscopic requiring it to be canned to prevent contact with moisture. Due to its high refractive index (1.85), it is necessary to provide a light guide (optical window or quartz glass) to interface the scintillation crystal to the photomultiplier.

The photomultipliers convert the light photons to an electronic signal through the production of photoelectrons in the photocathode. The electron multiplier section in a PM tube amplifies the electronic signal to give a current sufficiently large to be handled by conventional electronic circuits. The PMTs are usually arranged in a close-packed hexagonal array to ensure that the smallest possible gaps are left between the tubes. Typically the number of tubes used is 37, 61 or 91 depending upon the size of the photocathodes and diameter of crystal. The scintillation crystal and electronics are surrounded by a large lead shield to minimise the detection of unwanted radiation from outside the collimator field of view. The pulse height analyser discards the signals from background and scattered radiation or radiation from interfering isotopes so that only photons known to come from the photopeak of the radioisotope being imaged are recorded. In practice, a large fraction of primary photons is scattered within the patient and is recorded due to the finite energy resolution of the gamma camera. This will be reviewed in more detail in section 1.2.3.

1.2. Factors Affecting SPECT Imaging

The main goal of SPECT imaging is to produce a source distribution map in which the number of counts in a region of interest is directly proportional to the true activity

concentration in the same region within the patient. This represents, however, an ideal situation since the quantitative accuracy of the technique is limited by several factors that degrade the information obtained during image acquisition. These factors depend on the patient, physical radiation phenomena and technical considerations (Tsui *et al* 1994). The two first factors can be considered together since the size of the patient and the region of the body where the study is taking place will determine the magnitude of photon attenuation (absorption and scatter). The possibility of creating image artefacts increases as the magnitude of the attenuation increases (DePuey and Garcia 1989). The biokinetics of the radiopharmaceutical within the patient establishes its time distribution and uptake within several organs. This limits the acquisition time and therefore the statistics of the SPECT images. Even if the radioisotope allows long acquisition times, they should be restricted to avoid patient motion that can result in image artefacts.

Technical factors affecting SPECT include instrumentation (detector response, efficiency, dead time, energy resolution, uniformity, linearity and system alignment), acquisition parameters (angular sampling, radius of rotation, shape of the orbit, acquisition time per projection) and the details of image reconstruction (including image processing techniques). The most important aspects affecting quantification in SPECT imaging are reviewed in the following sections.

1.2.1. Detector Response

A very important characteristic of an imaging system is its spatial response. This is characterised by the system point spread function (or modulation response function in the frequency domain) that gives the response of the system to an infinitely narrow impulse of radiation. The gamma camera response is a combination of the collimator response and the intrinsic response of the detector. However, the collimator geometric response dominates the overall response of the system for most of the photon energies used in nuclear medicine for most realistic source to detector distances. The width of the collimator geometric response of a typical low-energy general-purpose collimator at 10 cm from the collimator face is approximately 8 mm.

The most important characteristic of the collimator response is its loss of resolution with increasing distance. Figure 1.3 shows this effect for a single view of the gamma camera with a parallel hole collimator and two source-collimator distances represented by x_a and x_b. Although there is practically no loss of efficiency with increasing distance

(due to the increase in exposed area in the detector) the corresponding images of the point sources onto the image plane clearly show the spread or blurring of intensity as the source moves away from the detector.

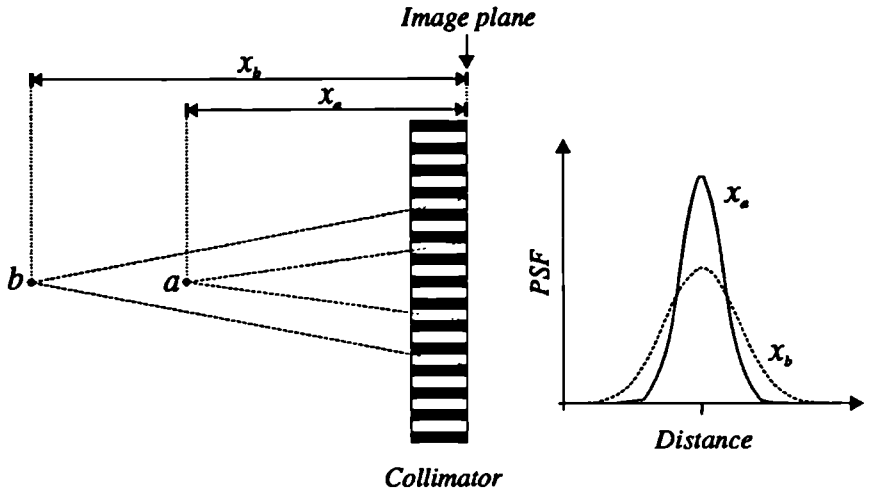

Figure 1.3. Schematic diagram showing the effect of collimator blurring with increasing source-collimator distance. Point sources at positions x_a and x_b produce different images in the image plane. Profiles across the images, passing through the maximum intensity of the image, are also shown.

The effect of loss of resolution with depth on a reconstructed image depends on several factors such as: angular sampling, orbit shape used during the image acquisition and reconstruction algorithm. An important consequence of loss of resolution with depth is the production of artefacts in the reconstructed images. Knešaurek *et al* (1989) have reported that detector blurring produces more geometric distortions when using a 180° angular sampling than when using a 360° angular sampling. The use of a 360° sampling in conjunction with arithmetic or geometric mean of opposite projections compensates for the loss of resolution with depth and thus reduces geometric distortions.

Detector blurring limits the capability of the system to separate regions of interest close to each other and hinders accurate delineation of object edges. This fact restricts the accurate measurement of areas or volumes of interest and therefore of specific activity (activity per unit mass of material). This is particularly important when determining the activity concentration in organs with dimensions smaller than or with same magnitude as the resolution of the system. It also affects the accuracy in the determination of activity concentration in small regions close to the boundary of large organs (Axelsson *et al* 1987).

1.2.2. Noise

The quantitative capability of SPECT is limited by noise since the accurate determination of any physical property (number of counts, volume, area) requires minimum noise fluctuations. The images obtained with a SPECT system have very poor statistics: typically only 10^6 events are detected during any image acquisition. The volume of interest and the number of detected events determine the statistical properties of SPECT images. The main factors that determine the total number of events in a SPECT study are:

- Dose to the patient, which should be kept as low as possible.
- Image acquisition times which should be reasonably small to avoid motion of the patient (up to 30 minutes).
- A major limitation on SPECT statistics is the very low collimator efficiency: typically, only 1 in $1x10^4$ emitted photons reach the detector. Photon decay is isotropic and therefore there is no a preferential photon direction during the decay. These effects limit the efficiency of the detector system to a great extent.

The factors mentioned above are inherent to both planar and SPECT modalities. Besides these factors, an important aspect affecting the statistical properties of SPECT imaging is that the noise propagates during image reconstruction leading to a reduction of signal to noise ratio. Budinger *et al* (1977) obtained the dependence of the root mean squared uncertainty on the number of resolution cells and the total number of events for a uniform source distribution as:

$$rms\% = \frac{k(\text{number of resolution cells})^{1/4}}{(\text{total number of events})^{1/2}} \times 100 \qquad (1.1)$$

where k is a factor that depends on the algorithm used to reconstruct the image (k is approximately 1.2 when using an iterative reconstruction algorithm).

It is important to note that the meaning of resolution cell appears to be obscure. Muehllehner (1985) defined the resolution cell as the region of interest that contains the smallest tissue to be visualised in the image. Gillen (1992) defined the number of resolution cells as the number of pixels in the reconstruction matrix that contain information. In this context, the resolution cell is assumed to be as large as, or larger than, the resolution of the imaging system. It is clear from equation 1.1 that the larger

the number of resolution cells in the image, the larger the uncertainty. It is also evident that an increase in the total number of events will lead to a lower uncertainty. This can be achieved by increasing the collimator efficiency, although at the expense of a loss of resolution (Moore *et al* 1992).

1.2.3. Scatter

Scatter of radiation within the patient is another important factor that affects the quantitative potential of SPECT imaging. This phenomenon is of considerable significance since Compton scattering is the most important type interaction for body tissues over most of the energy range used in nuclear medicine. Compton scattering involves the transfer of photon energy to a recoil electron resulting in a deflection of the original photon direction. The probability of Compton scatter as a function of the deflecting angle θ is given by the Klein-Nishina formula. For photon energies below 100 keV the direction of the scattered photons is preferentially in the forward and backward directions whereas for high photon energies the deflection of the original trajectory tends to be in the forward direction. Compton scattered photons have lower energy than the primary photons.

An important characteristic of the gamma camera is its energy response which is measured in terms of the energy resolution. This is defined as the full width at half maximum (FWHM) of the photopeak expressed as a percentage of the photopeak mean energy. Modern gamma cameras have energy resolutions of the order of 10% at 140 keV. Because the energy resolution of the gamma camera is finite, Compton scattered photons can be detected as unscattered events and are associated with a direction, and hence position, that does not correspond with the original photon emission.

The most common technique to reject scattered photons makes use of pulse height analysis and is called spectral windowing. It consists in setting an energy interval normally around the photopeak in which detected photons are accepted if their energy lies within this interval; otherwise they are rejected. A compromise must exist, however, so as to reject as large a fraction of scattered photons as possible whilst maximising the detection of primary photons. Typical energy windows, expressed as a percentage of the incident photon energy, range between 10% and 20%.

To understand the importance of using a spectral window in the loss of primary photons assume , for example, that the photopeak can be modelled with a Gaussian function and that the energy resolution is approximately 10%. A 10% energy window will discard approximately 23.8% of the total number of primary photons whereas a 20% energy window will discard only 1.9%. As the energy resolution of the gamma camera worsens, the fraction of rejected primary photons will increase. The fraction of detected scattered photons cannot easily be calculated due to the complexity of their spatial and energy distributions but will reduce with reducing energy window.

Scatter is a phenomenon that depends on primary photon energy, source depth and composition and structure of the attenuating medium. In planar imaging the scatter fraction, defined as the ratio of scattered to primary detected events, can be of the order of 0.5 or larger, depending on the type of study (Manglos *et al* 1987a). Floyd *et at* (1988) performed a detailed study using Monte Carlo simulation of scatter detection in SPECT as a function of three variables: depth, energy window and photon energy. Their results show, as expected, an increase in scatter fraction for an increased window width. On the other hand, an increase in the scatter fraction was observed for an increase in source depth, reaching a plateau as the source reached the centre of rotation. Finally, the scatter fraction for a given depth and energy window increased as the primary photon energy decreased. Representative values for a 20% energy window and a source depth of 10 cm (using a cylindrical water phantom of 22 cm diameter and 18 cm length) produced a scatter fraction of the order of 0.9 for 70 keV photons and of 0.5 for 140 keV photons. These figures show the large proportion of scattered photons that can be present in a SPECT study.

The presence of scattered photons in SPECT images results in a loss of contrast and a blurring of fine detail. These factors can limit the accurate determination of the physical dimensions of regions of interest. In addition, it produces extraneous activity in regions where originally there was no activity at all.

1.2.4. Photon Attenuation

Attenuation of photons within the body has been recognised as the single, most important factor limiting the quantitative potential of SPECT imaging (Malko *et al* 1986, Frey *et al* 1992). Photon attenuation is a very important phenomenon for the range of photon energies encountered in nuclear medicine (50 to 360 keV). Photoelectric absorption and Compton scattering are the predominant types of photon

interaction for this range of photon energies and the net effect of their occurrence is a loss of photon flux reaching the detector. Photoelectric interaction results in the absorption of the primary photon by an atom. As discussed in section 1.2.3, a Compton interaction produces a change in the direction and energy of an incident photon. Typical photon trajectories within the patient are shown in figure 1.4.

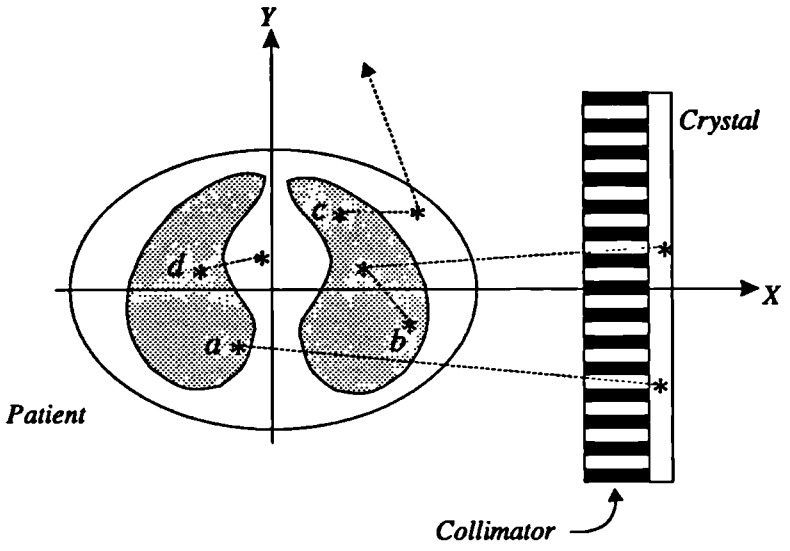

Figure 1.4. Possible photon trajectories within the patient: a) detection of a primary photon, b) detection of a scattered photon, c) scattered photon deflected and not detected, d) absorbed photon.

In order to fully understand the effects of photon attenuation in SPECT imaging, the mathematical formulation of both emission and transmission computed tomography will be reviewed in the next sections, followed by a brief description of the methods used to compensate for this phenomenon.

1.2.4.1. Transmission Computed Tomography

The mathematical framework to reconstruct tomographic images from projections was developed by Radon in 1917. However, this technique was not applied in medicine until the beginning of the 1970s when the first CT scanner was set up in clinical practice by Hounsfield (1973). The goal of transmission tomography is to produce a two-dimensional distribution of attenuation coefficients from a large number of transmission measurements through the object of interest. The measurements are obtained by rotating (and, in some older scanners, also translating) the source-detector system around the patient. CT is generally used to delineate anatomy and has the advantage over SPECT of controlling the statistics of the image acquisition. It has the

ability to discriminate differences in tissue density above 0.5% when the number of counts per pixel reaches $4x10^4$ (Cho *et al* 1974) and spatial resolutions of 1 mm can be achieved for high contrast objects (Barrett and Swindell 1981).

To understand the technique of CT, let $\mu(x,y)$ represent a spatial distribution of attenuating material. (Strictly speaking, the attenuation distribution is a three-dimensional function $\mu(x,y,z)$. However, this distribution can be represented by a two-dimensional function because the mathematical algorithms of image reconstruction produce cross sectional images.) Let us assume a fixed system of coordinates XY centred in the object distribution and $X'Y'$ a rotating system (also centred in the object) defining the orientation of the detector at angle α.

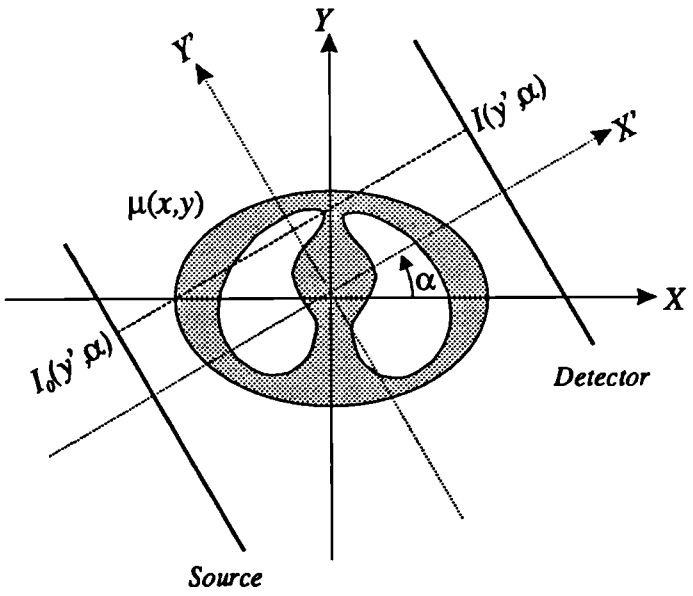

Figure 1.5. Cartesian systems of coordinates that define the acquisition process in transmission computed tomography.

The transmitted beam intensity, $I(y',\alpha)$, can be calculated by using Beer's law of photon attenuation, resulting in the following expression:

$$I(y',\alpha) = I_0(y',\alpha)\exp\left\{-\iint \mu(x,y)\kappa(x,y,y',\alpha)dxdy\right\} \qquad (1.2)$$

where $I_0(y',\alpha)$ is the incident beam intensity. The integration within the exponential term is performed along a path given by the function $\kappa(x,y,y',\alpha)$ which is defined by the physical properties of the detector system (geometry and spatial resolution). For parallel beam geometry and an ideal detector spatial response, this path is equal to a line defined by the equation $y' + x\sin\alpha - y\cos\alpha = 0$.

The integral of $\mu(x,y)$ along a ray is called the projection of $\mu(x,y)$, ray integral or the Radon transform[1]. Assuming a parallel beam geometry, the Radon transform can be easily obtained from equation 1.2 as:

$$P(y',\alpha)=\ln\left(\frac{I_0(y',\alpha)}{I(y',\alpha)}\right)=\iint\mu(x,y)\delta(y'+x\sin\alpha-y\cos\alpha)dxdy \qquad (1.3)$$

where δ is the delta function which defines the path of integration along the line $y'+x\sin\alpha-y\cos\alpha=0$. The aim of transmission computed tomography is to invert the Radon transform to obtain the distribution of attenuation coefficients $\mu(x,y)$.

Several analytic methods have been developed to estimate the attenuation distribution from its projections. Back-projection is the simplest image reconstruction algorithm: reconstruction is achieved by back-projecting each projection across the plane. Although simple in nature, it does not represent the true inverse of the projection operation (Barrett and Swindell 1981, Budinger and Gullberg 1974). However, back-projection has proved to be a very useful mathematical tool that in conjunction with Fourier or convolution techniques (called filtered back-projection algorithms) can produce an estimate of the attenuation distribution at a high level of accuracy. This type of reconstruction is used in most of the applications mainly due to its speed and ease of implementation.

Iterative algorithms have also been applied to obtain an estimate of $\mu(x,y)$. The algebraic reconstruction techniques try to invert a system of equations that represent the acquired projections (Rosenfeld and Kak 1982). A second approach is to produce an estimate of the object distribution whose projections are as close as possible to the measured data (Budinger *et al* 1979, Lange and Carson 1984). Although these algorithms may present certain advantages over the analytic methods, their use has been limited because their implementation can be cumbersome and time consuming.

1.2.4.2. Single Photon Emission Computed Tomography

In contrast to CT, emission computed tomography, ECT, seeks to produce the location and intensity of sources of emitted photons (radioisotopes) within an attenuating medium. The concentration of a radiopharmaceutical within a region of the

[1] The transform which maps a two dimensional function into a set of its line integrals is called the Radon transform.

body changes with time due to: radioactive decay, flow and biochemical kinetics within the body. This important characteristic allows the assessment of the metabolic function of several organs. This fact makes ECT an invaluable technique in diagnostic medicine.

Following the same reasoning as in transmission tomography, a spatial source distribution $\rho(x,y)$ is estimated by measuring a large number of projections around the patient. However, in this case the mathematical representation of the projections is different. Consider a source distribution $\rho(x,y)$ embedded within an attenuating medium $\mu(x,y)$ (see figure 1.6).

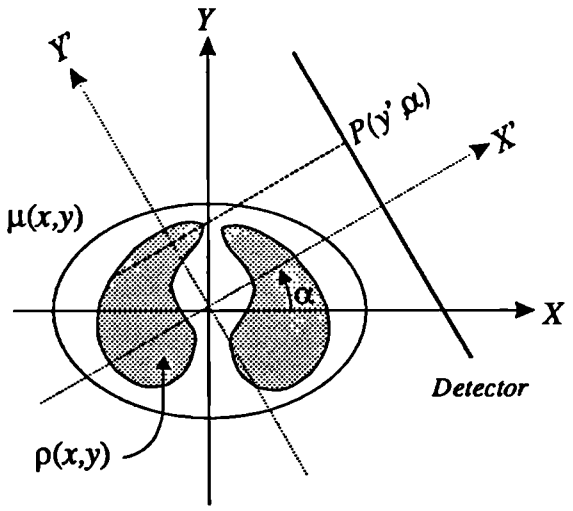

Figure 1.6. Systems of coordinates that define the acquisition process in single photon emission computed tomography.

The projections are produced according to the following expression:

$$P(y',\alpha) = \iint \rho(x,y)a(x,y,y',\alpha)\kappa(x,y,y',\alpha)dxdy \qquad (1.4)$$

where

$$a(x,y,y',\alpha) = \exp\left\{\int_{x,y}^{det} \mu(x,y)\kappa(x,y,y',\alpha)dxdy\right\} \qquad (1.5)$$

It can be seen that the contribution of the isotope concentration $\rho(x,y)$ to projection $P(y',\alpha)$ is weighted by the line integral of attenuation coefficients $a(x,y,y',\alpha)$ from the point (x,y) to the detector along the path defined by $\kappa(x,y,y',\alpha)$. Once again, for parallel beam geometry and a detector of ideal spatial resolution, the function $\kappa(x,y,y',\alpha)$ is equal to a line defined by the equation $y'+x\sin\alpha-y\cos\alpha=0$. The influence of the weighting function $a(x,y,y',\alpha)$ cannot be neglected because the

attenuation coefficients are normally large for the range of photon energies used in nuclear medicine (Budinger and Gullberg 1974, Budinger *et al* 1979). It is clear from equations 1.4 and 1.5 that the measured projections cannot provide an estimation of the source distribution unless some a priori information of photon attenuation is introduced. The integral transform depicted in equation 1.4 is a generalisation of the Radon transform, called the attenuated Radon transform.

A typical example of the effect of photon attenuation is given for a uniform source distribution within an object of constant attenuation coefficient. The photons originating from the centre of the object will be more attenuated than photons originating in its boundary. The composition of the attenuating material and the photon energy dictates the degree of attenuation, being greater for low photon energies. The effect of image reconstruction without compensation for photon attenuation produces a cupping or depression of reconstructed central values.

The main consequence of neglecting photon attenuation in objects of variable attenuation is the production of artefacts in the reconstructed images (Knešaurek *et al* 1989). Manglos *et al* (1987) have shown that the reconstruction of line sources within a volume containing variable attenuating media using filtered back-projection algorithms leads to distortions in the images. These distortions are caused by the effect of filtering the projection data which causes either an apparent spread of the peak (producing large tails) or over cancellation (leading to negative values in the image).

It is difficult to obtain an analytic solution to equation 1.4 because the true activity distribution and the structure and dimensions of the attenuating material are usually unknown. Because of this, approximations or iterative techniques are normally employed to compensate for photon attenuation. In the former case, correction can be applied to the projections before reconstruction or to the reconstructed image itself. Although simple to implement, these algorithms normally involve simplistic assumptions such as: attenuating medium of constant attenuation coefficient, small uniform source distributions concentrated in a single area or uniformly distributed over a whole area. In the interactive techniques the weighting factors in equation 1.5 can be incorporated into the reconstruction process. The reconstruction algorithms will be reviewed in the following sections.

1.3. Attenuation Compensation

It has been shown in the previous section that the mathematical formulation of emission imaging requires the use of reconstruction algorithms that can compensate for the photon attenuation inside the body. Reconstruction algorithms for three-dimensional nuclear medicine imaging can be classified in two main categories: analytic and iterative algorithms (Budinger *et al* 1979). However, it appears more natural for the purpose of this work to classify them as reconstruction algorithms for uniform and non-uniform attenuation compensation.

1.3.1. Uniform Attenuation Compensation Algorithms

The most important characteristics of this type of algorithms are that the attenuating medium is assumed to be constant throughout the body and that the source distribution is normally assumed to be uniform within a region. There exist three main categories of reconstruction methods for uniform attenuation compensation, depending on how the emission data are modified.

Pre-processing or multiplicative first order methods. In these methods the projection data are modified before reconstruction. Reconstruction is performed (normally with filtered back-projection) assuming that the modified projections represent the unattenuated data. Pre-processing methods assume a single region of uniform activity within a large absorbing medium of constant attenuation. Some of these methods are presented in table 1.1. The parameters involved in the modified projections in table 1.1 represent:

- μ linear attenuation coefficient assumed constant through the object. It can be set as the linear attenuation of water at the corresponding photon energy.
- L body thickness along the ray at angle α. This parameter can be calculated from an assumed or measured body contour, or from an initial reconstruction using a threshold fraction of the maximum image counts. The latter method assumes that detected scattered photons from the patient will produce a significant background activity level in the transverse images.
- f fraction of the total length along the ray at angle α that corresponds to the dimension of the source. It can be estimated from an initial reconstruction without attenuation compensation.

Table 1.1. Multiplicative first order attenuation compensation methods. In all cases μ is the linear attenuation coefficient and L is the body thickness along the ray at angle α. The parameter f is the fractional thickness of the source along the ray at angle α.

Method	Modified projections	Reference
Geometric mean	$\sqrt{P(y',\alpha)P(-y',\alpha+\pi)}\cdot e^{\mu L/2}$	Sorenson and Phelps (1987).
Hyperbolic sine	$\sqrt{P(y',\alpha)P(-y',\alpha+\pi)}\,\frac{\mu f L e^{\mu L/2}}{2\sinh(\mu f L/2)}$	Budinger and Gullberg (1974).
Average of minimum and maximum exponential factor	$[P(y',\alpha)+P(-y',\alpha+\pi)]\,\frac{2}{1+e^{-\mu L}+2e^{-\mu L/2}}$	Kay and Keyes (1975).
Average of exponential factor	$[P(y',\alpha)+P(-y',\alpha+\pi)]\,\frac{\mu L}{4e^{-\mu L/2}\sinh(\mu L/2)}$	Budinger *et al* (1979).

An important characteristic of the modified projections is that they involve the use of the geometric (squared root of the product of the conjugate projections) or arithmetic mean (average of the sum of the conjugate projections) which partially compensates for the loss of gamma camera resolution with increasing depth (Kay and Keyes 1975, Sorenson and Phelps 1987). Several disadvantages on the use of these algorithms arise when the assumptions are not fulfilled. For example, the geometric mean algorithm tends to overestimate the source intensity when several source distributions are present in the object (Barrett and Swindell 1981); the hyperbolic sine correction gives reasonably good results within an accuracy of approximately 10% when imaging small uniform sources of roughly the same strengths but there is an overestimation of the source distribution for extended sources (Moore 1982).

These pre-processing methods produce reasonably good results for relatively uniform and symmetric body sections like the head or the abdomen but they are less successful when applied to regions containing tissues with different attenuation coefficients. The most important characteristic of these analytic methods is their speed and ease of implementation. Most commercial manufacturers implement this type of algorithm in the software package of the gamma camera but their use is limited to regions of the body where the assumption of uniform attenuation holds.

Intrinsic compensation methods. These methods try to invert the attenuated Radon transform for uniform source distributions embedded in a uniform attenuating medium. The shape of the object is assumed to be convex. The correction is carried out by multiplying the projections with an exponential function that depends on the distance between the axis of rotation and the boundary of the object. This boundary can be calculated by assuming a particular shape for the object. A corrected image is obtained by using filtered back-projection with a modified ramp filter. Because the image can have significant noise levels, it can further be processed to smooth the noise (Moore 1982).

Post-processing methods. These methods compensate for photon attenuation by multiplying the reconstructed image, obtained for instance with filtered back-projection, with an attenuation correction matrix. Chang (1978) proposed an exact solution to the reconstruction of a point source within a medium of uniform attenuation coefficient. The correction matrix proposed by Chang is:

$$C(x,y)=\left[\frac{1}{M}\sum_{i=1}^{M}\exp\left(-\mu l(x,y,\alpha_i)\right)\right]^{-1} \qquad (1.6)$$

where $l(x,y,\alpha_i)$ is the distance from point (x,y) to the boundary of the attenuating material along the ray defined by the angle α_i and M is the total number of angles used during the tomographic acquisition. $l(x,y,\alpha_i)$ can be calculated from an assumed or measured body contour. The correction factors of equation 1.6 represent the average attenuation of a source at a point (x,y) over all projection angles.

This reconstruction algorithm produces good quality images when the source is concentrated in a small area. However, the reconstruction of extended sources results in an over correction or under correction in some parts of the image. To overcome this problem, an iterative process was also proposed that involves the re-projection of the estimated source distribution (that is, the corrected image). An error projection set is formed by subtracting the projection estimates from the measured projections. A corrected error image is reconstructed with the latter projections and multiplied with the correction matrix of equation 1.6. Finally, the corrected error image is added to the first source estimate. This process can be carried out iteratively. Chang (1978) performed computer test reconstructions and showed image quality improvement over

those obtained with the average of maximum and minimum exponential factor and the hyperbolic sine correction algorithms.

Attenuation compensation methods for uniform attenuation distributions can be applied to SPECT studies of regions of the body where the attenuation coefficients do not have very large variations, as in the brain or the abdomen. They produce reasonably accurate images. However, when they are applied to regions of spatially varying attenuation (like the thorax) the errors introduced are larger than those produced when no attenuation compensation is applied. Because of this, attenuation compensation is normally not applied in these cases.

1.3.2. Non-uniform Attenuation Compensation Algorithms

Modified Iterative Chang. Equation 1.6 can be modified to account for spatially varying attenuation coefficients in the medium (Chang 1978). The algorithm is relatively easy to implement and can be very fast. The modified Chang algorithm has been used by a number of researchers to correct for non-uniform attenuation and their results show that the algorithm produces good quality images when used with one or two iterations leading to easier interpretation (Bailey *et al* 1987, Manglos *et al* 1987b, Bailey *et al* 1988, Gilland *et al* 1991). However, Tsui *et al* (1988) showed that image quality and quantitative accuracy are degraded in the presence of noise and that Chang's algorithm is particularly susceptible to noise. In particular, the reconstructed images tend to become distorted when increasing the number of iterations (Tsui *et al* 1989). It is therefore important to use this algorithm with caution, especially with studies with very poor statistics.

Iterative methods. Non-uniform attenuation compensation can be performed using iterative reconstruction methods. The most interesting feature of the iterative algorithms is that they can introduce the physical processes involved in the creation of the projection data, such as: noise, attenuation, scatter and detector response. There is, however, a major limitation in their implementation due to the great computational effort to find an appropriate solution. The first step to reconstruct the image is to divide the object of interest into picture elements (pixels). The location of each pixel is defined by the indexes (i,j). The projections are also divided into bins, each projection bin k at angle m is denoted by p_{km}. These concepts are illustrated in figure 1.7.

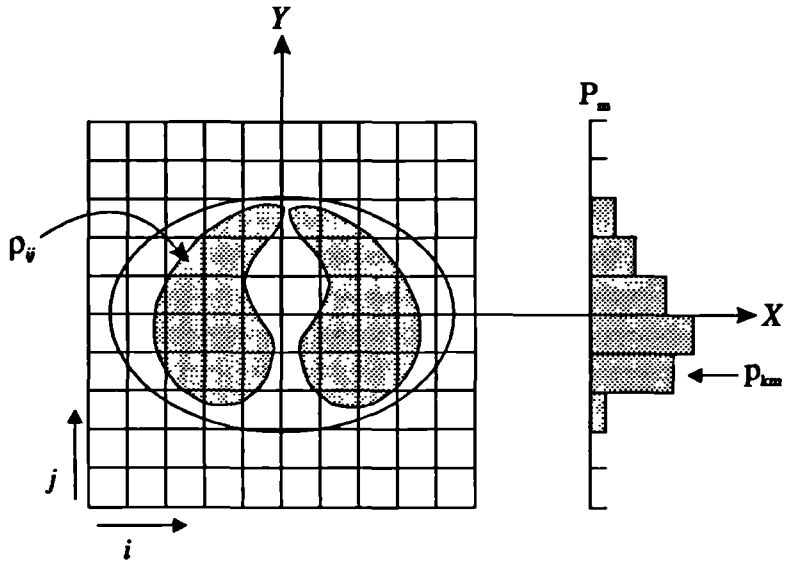

Figure 1.7. Discrete representation of the activity distribution ρ_{ij}. Projection data are represented by p_{km} where k indicates the projection bin and m the projection angle.

In this diagram ρ_{ij} represents the mean activity distribution at pixel (i,j), which is the parameter to estimate, and p_{km} are the projection data at the m^{th} angle and bin k. The relationship between the original source distribution and the measured projections can be expressed in terms of an operator or transition matrix W, whose w_{ij}^{km} components represent the probability that a photon emitted in pixel (i,j) with mean ρ_{ij} is detected at projection bin p_{km}. Mathematically, the formation of a projection bin p_{km} can be expressed by the following equation (in an analogous manner to equation 1.4):

$$p_{km} = \sum_{i,j} w_{ij}^{km} \rho_{ij} \tag{1.7}$$

The matrix W may contain all the physical features of the acquisition process such as: radioactive decay of the source material, attenuation, scatter, detector geometry and detector response. A model for photon attenuation can be introduced in the calculation of the matrix elements w_{ij}^{km} by computing the line integral of attenuation coefficients from pixel (i,j) to the detector at projection bin k and angle m.

The aim of the iterative reconstruction methods is to obtain an estimate of the source distribution ρ_{ij} such that when these values are projected the resultant projections are as close as possible to the measured data. The iterative algorithms are based on three steps: a model of the photon count statistics, description of the physical phenomena during image formation and an algorithm to find the solution. The photon statistics can

be modelled by assuming a constant level, Poisson (Lange and Carson 1984) or Gaussian noise (Huesman *et al* 1977). The physical phenomena can include models for photon attenuation, scatter and detector response (Malko *et al* 1986, Floyd *et al* 1986, Tsui *et al* 1988, Tsui *et al* 1989, Lang *et al* 1992, Frey *et al* 1992). The algorithm to find the solution can be based on the minimisation of a similarity criterion (Huesman *et al* 1977) or maximisation of a likelihood function (Lange and Carson 1984).

An example of an iterative method is the weighted least squares (WLS) method that tries to minimise the function:

$$\chi^2(\rho) = \sum_{km} \frac{\left[\sum_{ij} w_{ij}^{km} \rho_{ij} - p'_{km}\right]^2}{\sigma_{km}^2} \qquad (1.8)$$

where ρ_{ij} and w_{ij}^{km} are as defined above, p'_{km} is the measured projection data at bin k and angle m and σ_{km}^2 is the variance associated with the measure of the projection data. Several methods have been proposed to minimise equation 1.8 depending on the algorithm that determines the direction of minimisation (Huesman *et al* 1977). Webb *et al* (1983) compared the performance of a filtered back-projection algorithm with uniform attenuation compensation (average of minimum and maximum exponential factor) and weighted least squares. Their findings show that the WLS algorithms are normally time consuming but are more accurate.

The maximum likelihood-expectation maximisation (ML-EM) algorithm was used in this work to compensate for non-uniform photon attenuation. This algorithm has excellent properties for handling noise, especially at lower iteration numbers. In addition, it produces superior image quality when compared to other non-uniform attenuation compensation methods (Tsui *et al* 1988, Tsui *et al* 1989). This algorithm is reviewed in the following section.

1.4. The ML-EM Algorithm

The maximum likelihood-expectation maximisation algorithm models the photon counting according to a Poisson distribution and makes use of the expectation maximisation method to find the solution. Shepp and Vardi (1982) and subsequently Lange and Carson (1984) were the first to derive independently the algorithm for emission tomography. The distribution of activity in the object is chosen such that it

has the maximum likelihood of producing the observed projection data. As there is not analytic solution to the problem, the reconstruction must be carried out iteratively. Because the ML-EM can be implemented to incorporate compensation for physical factors of the acquisition system, it is expected to provide a more realistic model for handling the photon noise during reconstruction (Liow and Strother 1991).

1.4.1. The Poisson Distribution

The ML-EM algorithm assumes that the phenomenon of photon counting follows a Poisson statistics, a reasonable assumption due to the nature of radioactive decay in which a large number of emissions can take place and only a small fraction of these contributes to the recorded counts. A non-negative integer random variable Z with mean λ ($\lambda \geq 0$) follows a Poisson distribution if:

$$P(Z=k)=e^{-\lambda}\frac{\lambda^{k}}{k!} \tag{1.9}$$

The mean and variance of the Poisson distribution must be equal to the parameter λ.

1.4.2. The Algorithm

Because photon disintegration (quantified by ρ_{ij}) is a phenomenon that follows a Poisson distribution, the projection data p_{km} also obey the same statistics. Therefore, it follows from equation 1.9 that the probability of occurrence of projection bin p_{km} is given by:

$$P\left(p_{km}=\sum_{i,j}w_{ij}^{km}\rho_{ij}\right)=\exp\left(-\sum_{i,j}w_{ij}^{km}\rho_{ij}\right)\frac{\left[\sum_{i,j}w_{ij}^{km}\rho_{ij}\right]^{p_{km}}}{p_{km}!} \tag{1.10}$$

Lange and Carson (1984) calculated the joint probability of p_{km}, that is, the probability of recording all the projection bins at all angles, based on this equation. The logarithm of the joint probability is called the log-likelihood and it can be shown that it presents a maximum value for a given set of parameters ρ_{ij}. Lange and Carson (1984) calculated the expectation value of the log-likelihood and maximised it with respect to the set of parameters ρ_{ij}. They found the following expression for the mean activity distribution at pixel (i,j):

$$\rho_{ij}^{n+1} = \frac{\rho_{ij}^{n}}{\sum_{k,m} w_{ij}^{km}} \sum_{k,m} \frac{w_{ij}^{km} p_{km}}{\sum_{i,j} w_{ij}^{km} \rho_{ij}^{n}} = \frac{\rho_{ij}^{n}}{\sum_{k,m} w_{ij}^{km}} \sum_{k,m} w_{ij}^{km} \frac{p_{km}}{p_{km}^{n}} \qquad (1.11)$$

where: ρ_{ij}^{n} is the estimate of image pixel (i,j) after the n^{th} iteration,

w_{ij}^{km} is the transfer matrix from image pixel (i,j) to projection bin k at angle m,

p_{km} is the measured projection data at bin k and angle m,

$\sum_{k,m} w_{ij}^{km} p_{km}$ is defined as the back-projection operation of the array p_{km},

$\sum_{i,j} w_{ij}^{km} \rho_{ij}$ is the projection of the n^{th} image estimate ρ_{ij}^{n}.

The solution for the activity distribution in equation 1.11 represents an iterative process in which each iteration requires to calculate a projection and a back-projection operation. This process can be very time consuming, especially when the transition matrix elements w_{ij}^{km} are calculated during the operation of the program. In practice, the initial estimate is calculated as an average of the total number of counts in the projections over the total number of pixels in the reconstructed image.

1.4.3. The Attenuated Projector-Backprojector Algorithm

The ML-EM program used in this thesis was developed by the University of North Carolina Imaging Research Laboratory Group. Non-uniform attenuation compensation is included in the program by calculating the transition matrix elements w_{ij}^{km} according to an attenuated projector-backprojector algorithm developed by Gullberg *et al* (1985). This model assumes that all the detected photons originate from emissions along rays perpendicular to the detector which are not absorbed or scattered within the patient. It is also assumed that the detector has a perfect geometric response. The transition matrix elements in equation 1.7 are given by

$$w_{ij}^{km} = \begin{cases} \frac{A_{ij}^{km}}{\mu_{ij}} \left[1 - \exp\left(-\mu_{ij} l_{ij}^{km}\right)\right] & \text{if } \mu_{ij} > 0 \\ l_{ij}^{km} A_{ij}^{km} & \text{if } \mu_{ij} = 0 \end{cases} \qquad (1.12)$$

where:

$$A_{ij}^{km} = \sum_{b_{ij}}^{detector} \exp\left(-\mu_{i'j'} l_{i'j'}^{km}\right) \tag{1.13}$$

In these equations, μ_{ij} is the average of the attenuation coefficient of pixel (i,j), l_{ij}^{km} is the ray length within pixel (i,j) projecting into projection bin k at angle m, b_{ij} is the location at which the k^{th} ray intersects the pixel (i,j) on the right and the attenuation factor A_{ij}^{km} represents the probability that a photon at position b_{ij} will reach the detector at projection k and angle m. Figure 1.8 shows schematically the geometry used in the derivation of equations 1.12 and 1.13

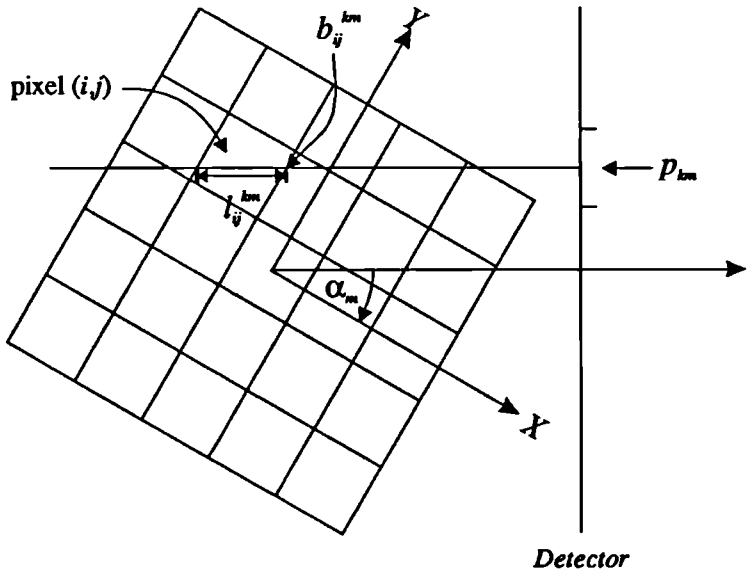

Figure 1.8. Schematic diagram showing the formation of a projection p_{km}.

The inclusion of attenuation compensation during image reconstruction requires to determine first the attenuation map of the object under investigation, μ_{ij}. When attenuation compensation is not requested, the transition matrix elements in equation 1.12 are set as unity.

1.4.4. Characteristics of the ML-EM

Positivity constrains. The parameter to be estimated in the ML-EM algorithm is positive by nature. The iterative approach to determine the activity distribution

(equation 1.11) satisfies this physical constrain. That is, the ML-EM imposes a positivity constrain in all the estimated values of ρ_{ij}.

Convergence. The ML-EM converges very slowly. Typically 20-40 iterations are needed to obtain an optimal reconstruction.

Reconstruction performance. The activity estimates appear to have better resolution, signal to noise ratio, and contrast compared to reconstructions produced from the same measurements with filtered back-projection algorithms used for SPECT (Snyder *et al* 1987).

Noise and image artefacts. The solution to the expectation value of the log-likelihood is given by its maximum value, which may occur after a very large number of iterations. It has been recognised that the images produced in emission tomography with the ML-EM algorithm become noisy and might present large distortions near their edges as iterations proceed and the images converge toward the maximum-likelihood solution (Snyder *et al* 1987). Therefore, some sort of stopping rule must be applied during the reconstruction process to obtain reasonable signal to noise ratio.

ML-EM for transmission tomography. The ML-EM algorithm has been used in the past for the reconstruction of transmission maps (Tsui *et al* 1989, Frey *et al* 1992). The model of photon counting statistics does not apply to the transmission data since a logarithmic transformation is applied in order to obtain the projections. However, it has been shown that the ML-EM algorithm produces less noisy transmission images than filtered back-projection (FBP) algorithms despite the modelling problems (Lalush and Tsui 1993). One of the most important advantages of the ML-EM algorithm over FBP is its ability to account for truncation artefacts (Frey *et al* 1992) which can be a serious problem when imaging very large patients.

1.5. Determination of Attenuation Maps

It is recognised that in order to obtain quantitative data in SPECT studies of regions of variable attenuation coefficient it is necessary to use reconstruction algorithms that can introduce attenuation maps into the attenuation compensation procedure. The use of transmission scanning to produce the attenuation maps has been suggested by a number of researchers since the advent of emission tomography studies. For example, Budinger *et al* (1979) proposed to use a 10-20 mCi source placed 3.5 metres from the detector to perform the transmission study. In practice, this procedure resulted in a

very inefficient process of data collection (reflected in the poor statistics of the attenuation maps) due to the isotropic nature of radioisotope decay, the large distance between the source and detector and the low counting rate capability of the gamma camera at the time. This effect, combined with the poor statistics characteristic of emission images and the noise propagation during image reconstruction produced corrected emission images of very poor quality. An interesting approach to limit propagation of errors during reconstruction involved the use of the transmission data to define tissue boundaries such as soft tissue, lung and heart. These boundaries define regions where known attenuation coefficients can be assigned (Budinger 1980).

Renewed interest in measuring attenuation maps for variable attenuation compensation arose in the middle 1980s. This interest was concentrated on studies of the body where large differences in attenuation coefficient exist, like the liver (Malko *et al* 1986) or heart (Tsui *et al* 1989, Manglos *et al* 1993). The possibility of performing attenuation measurements in conjunction with emission studies became feasible due to great advances in performance and optimisation of the components of the rotating gamma camera. New collimator designs have lead to an increase in sensitivity and improved resolution, the intrinsic resolution of the gamma camera has also been improved and its counting rate capability has been enhanced.

The possibility of using attenuation maps produced with a CT scanner has also been considered. However, this solution presents some disadvantages due to the high dose delivered to the patient, high cost of the examination and problems of image registration between the transmission and emission images. Developments of new imaging detectors are also under investigation to allow simultaneous image acquisitions of x-ray transmission and emission data (Lang *et al* 1992).

New developments such as multihead gamma cameras and their use with focusing collimators could represent an important step in SPECT imaging. The improved sensitivity and resolution of these systems would allow transmission-emission protocols to be performed with reasonable acquisition times and improved image quality when compared with the single rotating gamma camera. However, this technique has certain limitations mainly related with data truncation, limited axial sampling and complex image reconstruction algorithms. These areas are the subject of current investigation (Manglos *et al* 1992, Gullberg *et al* 1992, Jaszczak *et al* 1992, Manglos *et al* 1993).

The transmission maps can be measured in a manner analogous to x-ray CT using an external source coupled to the rotating gamma camera and measuring the photon flux

intensities at regular angular intervals over an arc of 180°. The image reconstruction algorithms developed for x-ray CT can be applied directly to obtain the attenuation maps.

Emission and transmission studies with a rotating gamma camera can be accomplished by performing simultaneous or non-simultaneous protocols. In both cases the transmission procedure can be carried out with an extended source (flood or sheet), a collimated extended source or a collimated line source scanned across the field of view of the detector. In the latter case, collimation can be restricted to one or two directions. The collimation of the external source will determine the type of transmission maps obtained with the gamma camera. If the external source and detector are collimated the attenuation coefficients determined are referred to as narrow beam attenuation coefficients. The use of an uncollimated external source results in the detection of scattered photons and the attenuation coefficients are then referred to as broad beam or effective attenuation coefficients.

Extended sources. These sources were initially used in emission-transmission SPECT, ET-SPECT, studies because of their availability in any nuclear medicine department. The major advantage in using this type of source is that its mounting (opposite to the gamma camera) requires only a minor modification in the detector gantry. However, the use of an extended source has been limited for several reasons:

- high dose to the patient when compared with a collimated external source (Cao and Tsui 1992),
- inevitable radiation exposure to staff,
- it provides broad beam geometry attenuation coefficients which cannot be used with scatter corrected SPECT data (Bailey *et at* 1987).

The use of broad beam geometry to determine the attenuation map can be of interest in situations where scatter compensation is not applied to the data before reconstruction. It is important to note with respect to this point that data collection in emission tomography is one of the worst possible cases of broad beam geometry (Harris *et al* 1984). It is expected that the use of attenuation coefficients measured under broad beam geometry can partially compensate for both attenuation and scatter effects.

Extended collimated sources. In this case, the flood or sheet source is fitted with a multihole parallel collimator. The collimator can be any of the collimators normally used for the gamma camera, or can be a modified version (for instance, a low-energy general-purpose collimator with half the collimator length). The modification of the

detector gantry to place this source is slightly more difficult because the weight of the source collimator can be as large as the gamma camera collimator. Systems using an extended collimated source and a rotating gamma camera have been assessed in terms of spatial resolution, sensitivity and patient dose (Cao and Tsui 1992). These authors recommend the use of a high active source fitted with a high resolution collimator to ensure reduction of statistical noise and dose to the patient. Attenuation coefficients predicted with these sources are referred to as narrow beam values and their use is restricted to the correction of scatter-free emission data.

Collimated line source. This source consists of a line source of radioactive material fitted with a slit collimator of sufficiently thick walls to restrict the photon direction to a small aperture angle. The back of the source is shielded with a high atomic number material to prevent photons travelling in directions of no clinical utility. The advantages of a scanning line source over the extended sources (collimated or uncollimated) include:

- the line source produces narrow beam attenuation coefficients, suitable for the correction of scatter-free emission data,
- radiation exposure to staff is kept to a minimum by shielding the source,
- fraction of photons scattered within the patient which are subsequently detected is very low,
- very high activities can be used for the line source resulting in an improved quality of attenuation maps,
- radionuclide used for the production of the transmission map can be the same as the emission study.

The use of the line source for transmission measurements requires, however, a major modification of the detector gantry. Stepper motors are used in order to scan the source across the field of view of the gamma camera. This scan has to be synchronised with the acquisition of the emission study. One approach to perform simultaneous ET-SPECT requires modification of the gamma camera electronics to allow the recording of the transmission events within a moving spatial window opposite to the line source.

1.5.1. Simultaneous ET-SPECT

A simultaneous ET-SPECT protocol offers the great advantages of avoiding problems of image registration and may not involve significant extra image acquisition time.

Simultaneous ET-SPECT requires the information of the transmission and emission studies to be separated. This separation can be achieved, for example, by using different radioisotopes for the transmission and emission studies and pulse height analysis. Although simple to implement, this method suffers from the drawback of having to correct for cross-talk between the collected data. Furthermore, the attenuation values have to be adjusted to account for the difference in photon energy. Simultaneous ET-SPECT can be classified according to the photon energy of the radionuclides involved in the transmission and emission studies (E_T and E_E, respectively):

a) $E_T<E_E$. This combination of photon energies requires that the difference between E_T and E_E be sufficiently large as to separate the mixed information by pulse height analysis. The emission data is not disturbed by the presence of the lower energy photons. On the contrary, the transmission data is contaminated with scattered photons arising from the emission study and, because their contribution is normally very large, they have to be corrected for if quantitative data are to be generated. The attenuation coefficients obtained with a photon energy E_T have to be scaled to produce the corresponding attenuation map at energy E_E.

Bailey *et at* (1987, 1988) used a ^{153}Gd (98 and 103 keV, $t_{1/2}$=242 days) flood source for the measurement of the attenuation map and ^{99m}Tc (140 keV, $t_{1/2}$=6 hours) for the emission study. The transmission data contamination was removed by estimating the scatter contribution from the emission data through a convolution subtraction technique. The scaling of the attenuation maps was based on a linear relationship between the attenuation coefficients at the different energies. Non-uniform attenuation compensation was performed using a modified iterative Chang algorithm. Their results showed improved quantification with both phantom and patient studies. Predicted activities were within 5% of the measured activities when using a simple geometric arrangement containing only two materials.

A set of 4 line sources equidistantly separated by 40 mm has also been used to perform simultaneous ET-SPECT studies (Larsson *et al* 1993). The protocol involves the use a transmission photon energy lower than the photon energy for the emission study (such as ^{99m}Tc, ^{57}Co, ^{153} Gd or ^{241}Am). A cross-talk correction is achieved by closing the collimated line sources for a short period and acquiring an image with only emission data using the transmission window. This procedure is repeated for every projection angle. The correction involves subtracting the latter image, normalised by the fraction

of time spent during the transmission and the cross-talk acquisitions, from the transmission images at each projection.

b) $E_T=E_E$. The use of equal energies for simultaneous ET-SPECT requires the use of a scanning line source and a major modification of the gamma camera to electronically window the spatial *X-Y* gamma camera signals. The most successful implementation of this type of acquisition has been reported by Tan *et al* (1993) in which a collimated line source scans in synchrony with a spatial window on the gamma camera in order to separate the emission and transmission data. There are several important characteristics regarding this system: the transmission data is generated with very little scatter (below 5%) producing negligible contamination into the emission data, loss of emission counts is below 10% and any combination of energies of the emission and transmission studies can be used. The protocol provides high quality data in a practical time interval.

c) $E_T>E_E$. The method also requires separation of the transmission-emission data using spectral analysis. This combination of photon energies is of particular importance when imaging low energy emission photons (e.g. ^{201}Tl). Cross contamination also occurs in this case due to scattered photons originating from the transmission photons into the lower emission energy window. Frey *et al* (1992) performed phantom and patient studies using ^{201}Tl for the emission study and ^{99m}Tc for the transmission study using a collimated sheet source. The contamination of the emission study, due to scattered photons within the patient and characteristic x-rays produced in the collimator, was removed by using post-acquisition image processing. The inclusion of the variable attenuation map into an iterative reconstruction algorithm showed improved image quality as compared with the use of an algorithm without attenuation compensation.

1.5.2. Non-simultaneous ET-SPECT

Non-simultaneous ET-SPECT offers several advantages:

- neither the transmission and emission data are cross contaminated (as long as transmission is performed before emission),
- separation of the information is inherent,
- transmission and emission photon energies are not restricted,
- more control in the gamma camera pile up can be achieved.

The use of the same photon energies for both studies allows the transmission data to be used directly without scaling. In some cases it is useful, however, to use different

energies due to the availability of some sources. In the latter case it is necessary to transform the attenuation map to the energy used in the emission study. The major drawback in this technique is the extra imaging time required to perform the transmission study which may lead to possible patient motion and problems of misregistration.

Tsui *et al* (1989) performed a detailed experimental study using a collimated sheet source (12 mCi of ^{99m}Tc), ^{201}Tl for the emission study and iterative techniques to include variable attenuation compensation. A heart-lung phantom study and a patient study were performed using four reconstruction algorithms: FBP without attenuation compensation, ML-EM without attenuation compensation, modified iterative Chang and ML-EM with attenuation compensation. Their results show that the ML-EM algorithm with attenuation compensation provided the best image quality in terms of reduced artefacts, better spatial resolution and reduced distortions. This algorithm provided reconstructed images with regions of uniform activity distributions where uniformity existed.

Ljungberg and Strand (1990a, 1990b) used a ^{57}Co (122 keV, $t_{1/2}$=272 days) for the transmission source and three different radionuclides (^{99m}Tc, ^{201}Tl and ^{111}In) for a phantom emission study. The transmission measurement aimed to produce density maps rather than attenuation coefficients. For this, it was assumed that the variation with energy of the mass attenuation coefficients for the different tissues of the phantom is not significant. Therefore, the photon energy used for the flood source was irrelevant. The density maps were used to compensate for both attenuation and scatter effects using a pre-processing algorithm based on the calculation of build up factors. The compensation algorithm required a modification of the projections before image reconstruction. Their results show improved quantitative data within 10% uncertainty. Image resolution and contrast were also improved.

Gilland *et al* (1991) have also shown improved image quantification and reported less noisy data when applying a non-uniform attenuation compensation algorithm. The attenuation maps were obtained with a ^{99m}Tc flood source. An ^{111}In source was employed for the emission study. A Chang reconstruction algorithm for uniform attenuation compensation and a modified iterative Chang for non-uniform attenuation compensation were used. Their results show that non-uniform attenuation compensation provided improved image quality with lower noise. Quantitative accuracy within 15% was achieved.

1.5.3. Other methods

A method which cannot really be classified among the algorithms before was suggested initially by Budinger (1980) and tested by Galt *et al* (1992). This method uses tissue contours determined from segmentation of a transmission scan to assign a priori determined attenuation coefficients to different regions of the image. The attenuation map obtained in this form reduces the errors caused with the introduction of noisy transmission distributions into the emission data. The implementation of this method presents several advantages:

- segmented images are not affected by Poisson noise,
- the protocol involves separate image acquisitions for the emission and transmission studies and no cross contamination occurs,
- there is no need to scale the attenuation maps,
- dose to the patient can be kept to a minimum level since high statistical accuracy in the determination of the attenuation map is not required.

The attenuation map has been used in a variable attenuation compensation algorithm. Galt *et al* (1992) have shown that the application of this method in combination with a modified Chang reconstruction algorithm produces improved contrast and image quality. This method has also been used to compensate for photon attenuation in positron emission tomography (Meikle *et al* 1993).

A completely new approach to obtain the attenuation map has been suggested by Madsen *et al* (1993) by using only an emission study. Image segmentation is also used in this technique. However, image contours are determined using ^{99m}Tc-macro aggregated albumin to locate the lungs and an external source wrapped around the patient to determine the chest boundary. Attenuation coefficients can then be assigned to the segmented regions. The authors claim that the technique offers a feasible solution for attenuation compensation in clinical applications. However, a further investigation is necessary concerning the dose delivered to the patient and the accuracy of the method as compared with other techniques.

1.6. Monte Carlo Simulation of an ET-SPECT System

This thesis looks at several properties of a transmission-emission tomographic system based on a rotating gamma camera using Monte Carlo techniques and experimental

methods. Some of the methodology used throughout the development of this work is described in the following sections.

1.6.1. General Description of the Tomographic System

The tomographic system consisted of a rotating gamma camera fitted with a low-energy general-purpose (LEGP) collimator. Two phantoms were used in the present thesis, a geometric and an anthropomorphic phantom. These phantoms will be described in detail in the following chapters. The source distribution was considered either external to the phantom (for the transmission study) or within the phantom (for the emission study). The description of the simulated system is illustrated in figure 1.9. The Monte Carlo method (see Appendix 2) was used to perform the photon transport from the location of the source through the phantom and collimator. The photon detection process with the gamma camera was implemented as an additional procedure after the photon transport had been performed using a semi-empirical approach (presented in Chapter 2). This approach used experimental data which characterised the intrinsic resolution of the gamma camera in terms of its energy resolution and spatial response. The camera was modelled as a plane with the same dimensions as the collimator. The procedure included, for every photon hitting the camera, the sampling of the energy resolution from a Gaussian function with FWHM as a function of the incident photon energy. The effect of spatial resolution was introduced via digital convolution using the intrinsic gamma camera point spread function with a FWHM of 3.5 mm.

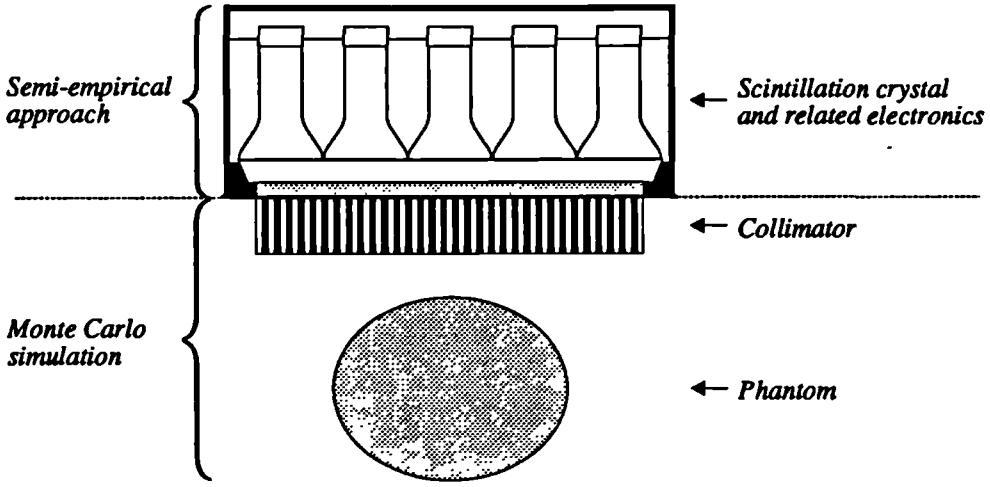

Figure 1.9. Characterisation of the system within the simulation.

The Electron-Gamma-Shower Monte Carlo code (Nelson *et al* 1985), EGS4, was used in this thesis to perform all the simulations. In the Monte Carlo simulation the geometry of the system was defined using simple objects such as planes, cylinders (circular or elliptical in cross section) and spheres. Complex shapes could be modelled using combinations of these objects to define regions which were associated with particular media. The Monte Carlo method performed the photon transport through the different regions that formed the system considering three types of photon interactions: photoelectric effect, Compton and Rayleigh scattering. Photon interactions with matter are briefly reviewed in Appendix 1.

The history of every single photon was traced until the photon was either absorbed or its energy fell below a cut-off energy or it crossed the geometric boundary of the system. The selection of the cut-off energy, illustrated in figure 1.10, was based on the energy resolution of the gamma camera. Assuming that for a monoenergetic beam of radiation the photopeak could be represented by a Gaussian function with standard deviation σ and primary energy E_p, the cut-off energy was chosen as $E_{cut\text{-}off}=E_p-5\sigma$. It was calculated that the detection probability of a scattered photon with an energy below the cut-off energy as defined above would be less than 1% for the range of energies considered in this project.

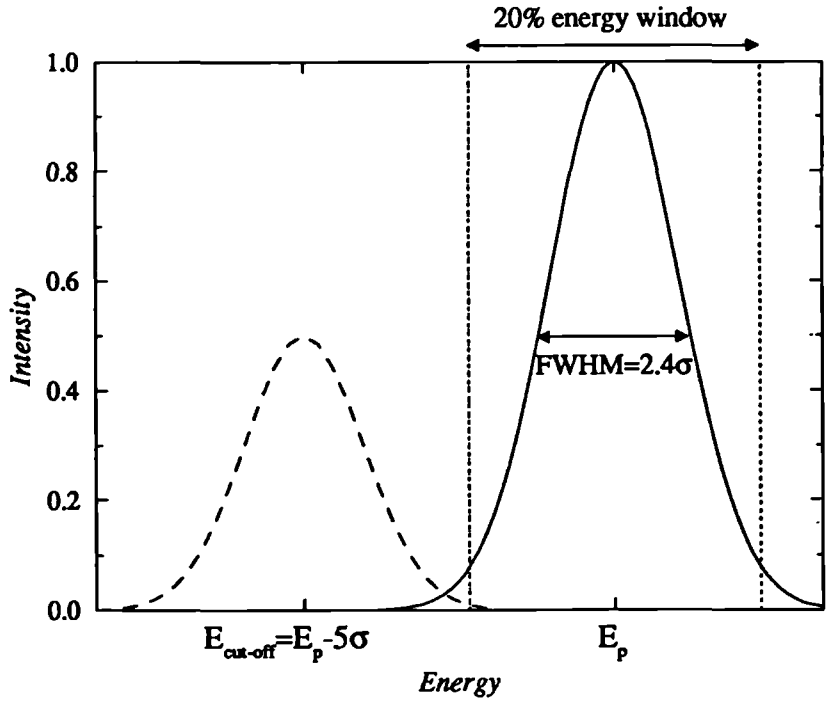

Figure 1.10. Selection of the cut-off energy in the Monte Carlo simulation.

A 20% spectral window centred on the photopeak was considered in all the simulations. In this thesis, no attempt was made to compensate for the presence of scattered photons in the reconstructed images. However, because the Monte Carlo program allowed to separate primary and scattered photons, the analysis was performed with either only primaries or primary plus scattered events (referred to as total). In this way it was possible to investigate the effects of photon attenuation and the performance of an attenuation compensation algorithm in the absence of other degrading factors. The images were simulated in a 128x128 or 64x64 format corresponding to a physical pixel size of 0.32 cm or 0.64 cm, respectively.

1.6.2. Transmission CT

The transmission tomographic system consisted of an external source (flood or collimated line source), a non-uniform phantom, a LEGP collimator and the semi-empirical approach to account for the detection of the photons with the gamma camera. The geometry of the system is shown in figure 1.11.

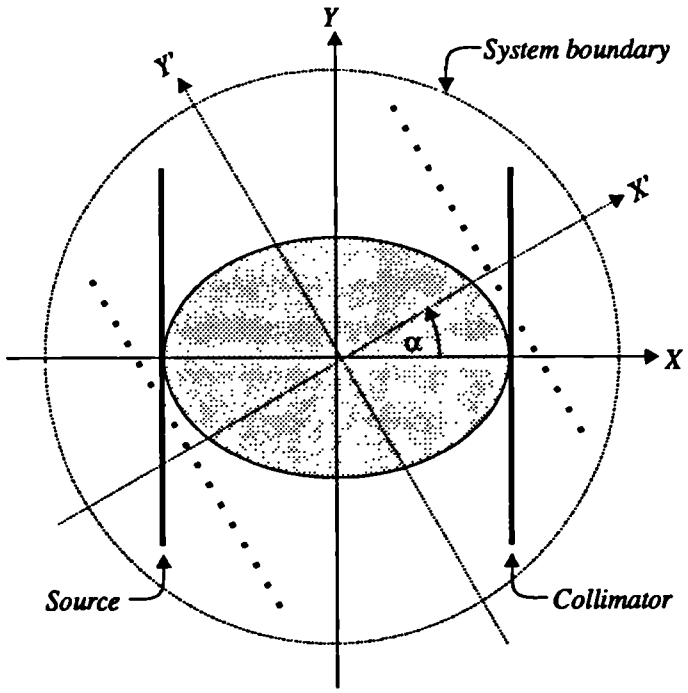

Figure 1.11. Geometry of the system used in the simulation of the transmission study.

Two separate Monte Carlo programs were written to simulate the tomographic system corresponding to a phantom simulation and a collimator program. The first program

simulated the production of photons in an external source and their transport through a phantom. If the photons reached the front plane of the collimator their parameters were stored on magnetic tape. The recorded photon parameters were then used as input data for the simulation of the LEGP collimator. The collimator program included the detection process as an additional procedure.

The formation of the projections required the simulation of a blank image (that is, with the phantom removed) to calculate the incident beam intensity $I_0(y',\alpha)$ (see equation 1.3). Thirty-two projections were simulated over an angular range of 180° assuming a circular orbit.

1.6.2.1. Simulation of the External Source

To simulate the projections at different angles α, the photon position and direction cosines were initially generated in a fixed system of coordinates XY (projection at α=0° in figure 1.11) and subsequently rotated an angle α about the Z axis using the transformation:

$$\mathbf{R}_\alpha = \begin{bmatrix} \cos\alpha & -\sin\alpha \\ \sin\alpha & \cos\alpha \end{bmatrix} \tag{1.14}$$

The direction of emission, which is defined in spherical coordinates by the polar angle θ ($0 \le \theta \le \pi$) and the azimuthal angle φ ($0 \le \varphi \le 2\pi$), was generated according to an isotropic angular distribution. Figure 1.12 shows the angles θ and φ that define an arbitrary photon direction represented by vector $\mathbf{u}=(u,v,w)$.

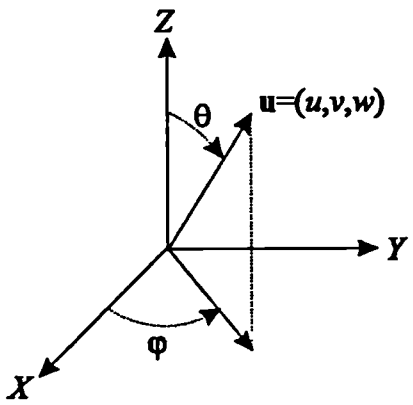

Figure 1.12. The photon direction is defined completely by the polar angle θ and the azimuthal angle φ.

For an isotropic distribution, the probability that a photon will be emitted into the element of solid angle $d\Omega$ is equal to the fraction of the solid angle element in a 4π geometry. The probability density function for an isotropic source in polar coordinates is (Chan and Doi 1988)

$$P(\theta,\varphi)d\theta d\varphi = \frac{d\Omega}{4\pi} = \frac{\sin\theta d\theta d\varphi}{4\pi} \quad 0 \le \theta \le \pi,\ 0 \le \varphi \le 2\pi \tag{1.15}$$

Since $P(\theta,\varphi)$ is a function of the independent variables θ and φ, the probability that a photon will be emitted at an angle θ is obtained by integrating equation 1.15 over φ, obtaining:

$$P(\theta) = \frac{\sin\theta}{2} \tag{1.16}$$

Similarly, the probability that a photon will be emitted at an angle φ is:

$$P(\varphi) = \frac{1}{2\pi} \tag{1.17}$$

These probabilities were used to generate the angles θ and φ by using the inversion method (see Appendix 2). The photon direction cosines were obtained using these angles and the expression of unit vector components in spherical coordinates:

$$\mathbf{u} = (\sin\theta\cos\varphi, \sin\theta\sin\varphi, \cos\theta) \tag{1.18}$$

The simulation of the flood and collimated line sources was based on restricting the values taken by the azimuthal angle φ of the emitted photons. To show this, assume that a point source is located at the origin of the system of coordinates shown in figure 1.13 and that the collimator is placed at a distance H from the origin with its face parallel to the YZ plane. If the photon's polar angle θ takes a value $0 \le \theta \le \pi$ but its azimuthal angle α lies within the range $-\Delta\varphi \le \varphi \le \Delta\varphi$, $\Delta\varphi > 0$, then only a segment of a sphere centred in the origin of coordinates will be encompassed by the emitted photons.

Therefore, a flood source can be simulated by generating photons uniformly on a section of a plane parallel to the YZ plane and sampling the emission angles by setting $0 \le \theta \le \pi$ and $-\pi/2 \le \varphi \le \pi/2$ (this is an efficient process as only photons heading

towards the collimator plane are generated). Similarly, a collimated line source can be simulated by generating photons along a segment of a line parallel to the Z axis and sampling the emission angles by setting $0 \leq \theta \leq \pi$ and $-\Delta\varphi \leq \varphi \leq \Delta\varphi, \Delta\varphi > 0$. The parameter $\Delta\varphi$ defines the collimation of the source. In practice, a collimated line source is a line source fitted with a slit collimator with sufficiently thick walls to restrict the photon flux direction within a small aperture angle. For each projection angle, the slit source scans across the field of view of the gamma camera. In the Monte Carlo simulation this scan was equivalent to generating photon positions uniformly on a section of a plane parallel to YZ and sampling their directions as described before. It is important to note that once the photon direction (u,v,w) was generated, it had to be rotated to correspond to the particular projection at angle α.

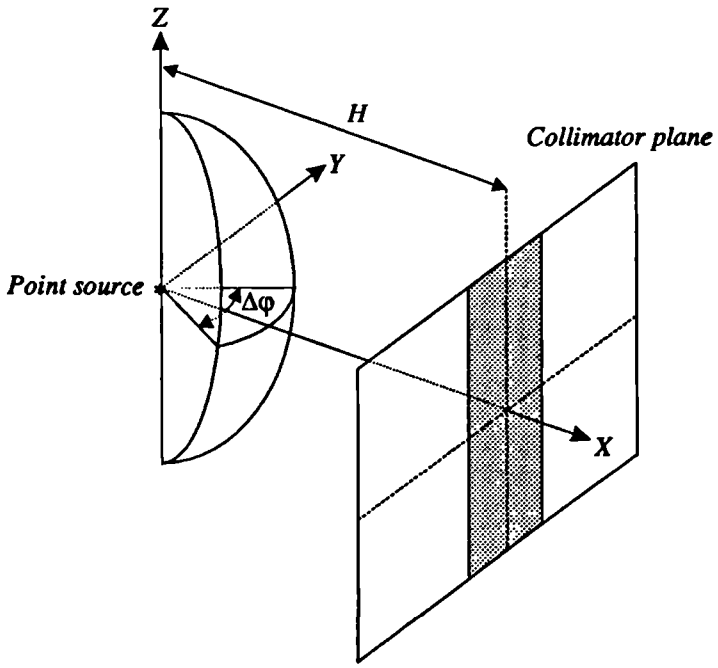

Figure 1.13. Segment of a sphere covered by emitted photons whose azimuthal angles have been restricted to take the values $-\Delta\varphi \leq \varphi \leq \Delta\varphi$. The shaded area on the collimator plane indicates the region hit by the emitted photons.

1.6.3. Emission CT

The tomographic system for the emission study is shown in figure 1.14. It consisted of a non-uniform phantom, a LEGP collimator and the semi-empirical approach to account for the detection of the photons with the gamma camera.

The simulation of the system was performed in a similar manner as the simulation of the transmission CT system. A program simulated the photon transport through the phantom and if the photons reached a cylinder (defined as system boundary 1 in the figure) centred in the origin of coordinates and with a radius equal to the radius of rotation, their parameters were stored on magnetic tape. The recorded photon parameters were then used for the simulation of the LEGP collimator. The collimator program was slightly modified such that every photon reaching the system boundary 1 could contribute to several projections. Sixty-four projections were simulated over 360° assuming a circular orbit.

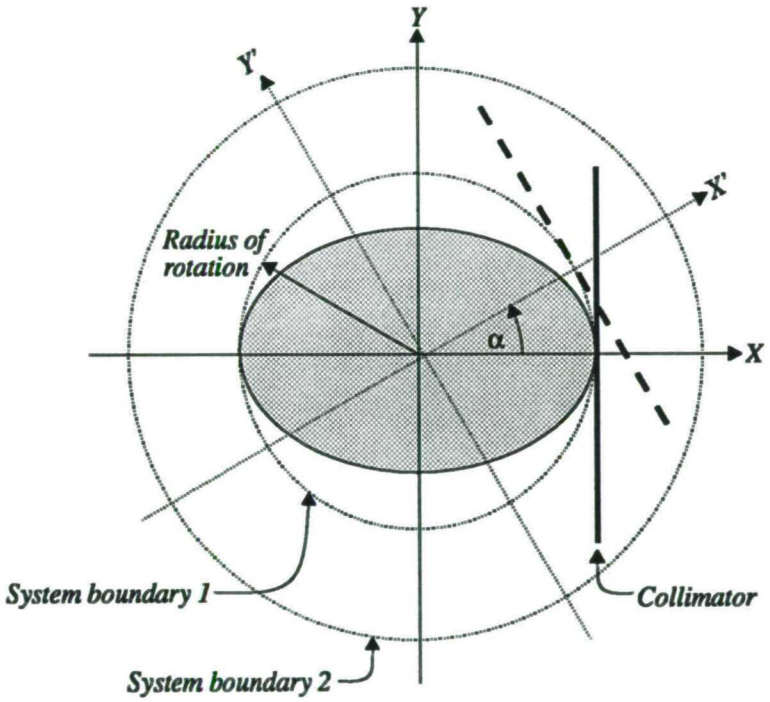

Figure 1.14. Geometry of the system used in the simulation of the emission study.

1.6.3.1. Modification of the Collimator Program

The collimator simulation read as input data the photon vectors created with the phantom simulation. In order to maximise the number of detected events per projection, an algorithm was developed in which a single photon history contributed to several projections. To illustrate the procedure, figure 1.15 shows a cross section of a phantom, the system boundary 1 considered in the phantom program and several collimator positions at angles α_1, α_2, α_3 and α_4. The figure also shows a photon emitted within the phantom travelling towards the circular cylinder and hitting the collimator face at different positions represented by A, B and C for the projections α_1,

α_2, and α_3, respectively. For a given photon trajectory the program calculated all projections that the photon would intercept and, for each successful event, the projection number and intersection point were stored in an array. Afterwards, photon transport through the collimator was performed for all those projections intercepted by the photon trajectory. In this hypothetical example, the photon would be transported through the collimator at projections α_1, α_2 and α_3 but not through projection α_4. This process was repeated for all the photon histories produced by the phantom program.

This method allowed the contribution of the emitted photons to the final image to be maximised and it improved the image statistics without a substantial increase in CPU time. It also allowed the size of the data files generated by the phantom program to be kept to a minimum (as less input photons were needed for the collimator program).

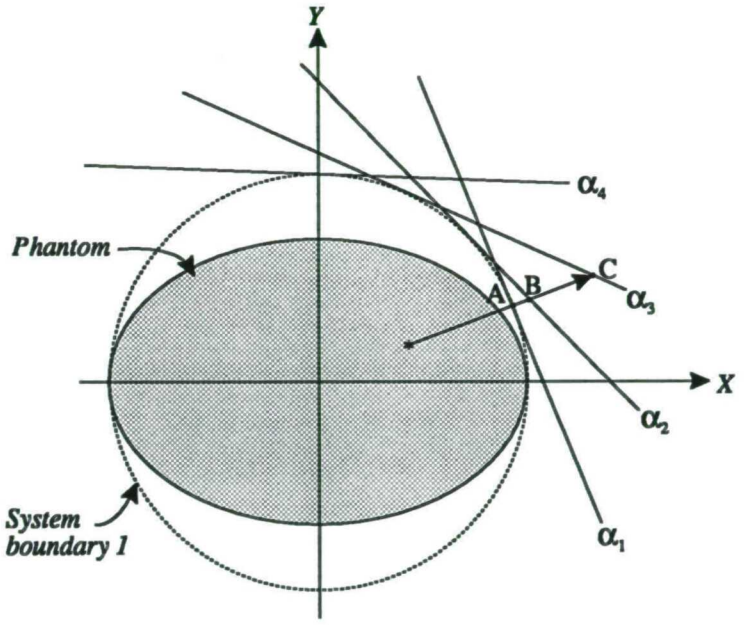

Figure 1.15. Schematic diagram showing the positioning of the phantom, the location of the circular cylinder used as the geometric boundary of the phantom program and several collimator positions at angles α_1, α_2, α_3 and α_4. An emitted photon can contribute to several projections.

1.6.4. Image Reconstruction

1.6.4.1. Emission Study

Image reconstruction for the emission study was performed using the ML-EM reconstruction algorithm with and without attenuation compensation. This algorithm has been used in the past to improve quantification in SPECT imaging (Tsui *et al*

1988, Tsui *et al* 1989, Frey *et al* 1992, Lang *et al* 1992). This method produces improved image quality and reduced image noise when compared with other reconstruction methods (Tsui *et al* 1988, Tsui *et al* 1989). Fifty iterations of the ML-EM algorithm were used for the image reconstruction.

In addition to the ML-EM reconstruction algorithm, and for comparison purposes, the emission study with an anthropomorphic phantom (presented in Chapter 6) also included the image reconstruction with a filtered back-projection (FBP) algorithm using a Ramp-Hanning filter. This filter is commonly used in cardiovascular nuclear imaging (Jarritt and Ell 1984). The Ramp-Hanning filter is defined in frequency space as the multiplication of the Ramp function, $|f|$, and the Hanning window according to the following expression:

$$\tilde{c}(f)=\begin{cases}0.5|f|\{1+\cos(\pi f/f_m)\} & \text{if } |f|\le f_m \\ 0 & \text{if } |f|>f_m\end{cases} \qquad (1.19)$$

where f_m is referred to as the cut-off frequency and represents the frequency at which the filter reaches zero gain. Both frequencies f and f_m are measured in cycles / cm. The cut-off frequency, f_m, was chosen as 0.8 cycles / cm. This frequency gives adequate resolution with limited image noise.

1.6.4.2. Transmission Study

It has been mentioned in section 1.4.4 that the ML-EM algorithm can be used to reconstruct attenuation maps. Lalush and Tsui (1993) have reported that the ML-EM algorithm performs similarly to FBP. However, the ML-EM algorithm produces less noisy images than the FBP algorithm and suppresses streaking artefacts. On this basis, the ML-EM algorithm was used to reconstruct the attenuation maps. Fifty iterations were used for the image reconstruction. The images produced with the ML-EM program represent the linear attenuation coefficient times the physical size of the pixel. Therefore, to calculate the linear attenuation coefficient in a region of interest, μ_{ROI}, the following expression was used:

$$\mu_{ROI}=\frac{\text{mean pixel value in the region}}{\text{physical pixel size}}\ \text{cm}^{-1} \qquad (1.20)$$

1.7. Image Comparison

The experimental validation of the collimator simulation (presented in Chapter 3) required comparison between the simulated and experimental images. The image comparison theory used in Chapter 3 is briefly developed in the following sections.

1.7.1. Image Registration

An appropriate comparison of two images requires first a registration step in one of the images in order to correct for the differences in data collection. Image registration normally considers a geometrical and a grey map transformation. The geometrical registration can incorporate translational shifts, rotation and spatial scaling of one image with respect to the other. A grey map transformation accounts for the differences that might exist between the image intensities and backgrounds.

In order to formalise these concepts, let $f_1(i,j)$ and $f_2(i,j)$ represent the two images to be compared, where $i,j=1,..,N$ are the coordinates of the discrete image plane within a range of interest (image region). Assuming that these images were acquired under different circumstances and that $f_1(i,j)$ is taken as a reference, a general geometric registration procedure implies application of a sequence of operators acting on $f_2(i,j)$. These operators include: align the images by shifting $f_2(i,j)$ Dx and Dy pixels ($-k \le Dx \le k$ and $-l \le Dy \le l$, $k,l \ge 0$), rotate $f_2(i,j)$ an angle R with respect to a reference point on the image and, finally, scale $f_2(i,j)$ by a factor S to make a correspondence of one to one with $f_1(i,j)$.

The geometric registration can then be expressed by the equation:

$$f_2'(i,j) = \mathbf{S}\cdot\mathbf{R}\cdot(\mathbf{D_x}\mathbf{D_y})\cdot f_2(i,j) \qquad (1.21)$$

where **S**, **R** and $\mathbf{D_x}\mathbf{D_y}$ represent the scaling, rotation and translation operators, respectively. A grey map transformation is a linear operator that is applied in conjunction with the geometric registration. It is normally of the form:

$$f_2''(i,j) = NF\left(\mathbf{S}\cdot\mathbf{R}\cdot(\mathbf{D_x}\mathbf{D_y})\cdot f_2(i,j)\right) + BG \qquad (1.22)$$

where *NF* is a normalisation factor that accounts for differences in intensity and *BG* is a parameter that reflects the differences in background (Venot *et al* 1986). The values of *NF* and *BG* can be found on the basis of an optimisation of similarity criteria such as the classical methods of correlation coefficient, correlation function and sum of absolute values of the differences (Pratt 1974, Svedlow *et al* 1978, Appledorn *et al* 1980, Gonzalez and Wintz 1987). More sophisticated similarity criteria like the stochastic sign change and the deterministic sign change (Venot *et al* 1984) can also be used. The choice of any of these criteria depends on the characteristics of the images and on the feasibility on the implementation of the algorithm.

1.7.2. The Correlation Coefficient

The correlation coefficient is the most common criterion used to determine the similarity between two images (Gonzalez and Wintz 1987). It is given by:

$$r=\frac{\sum f_1(i,j)f_2''(i,j)-\sum f_1(i,j)\sum f_2''(i,j)/N^2}{\left[\left\{\sum f_1^2(i,j)-\left(\sum f_1(i,j)\right)^2/N^2\right\}\left\{\sum\left(f_2''(i,j)\right)^2-\left(\sum f_2''(i,j)\right)^2/N^2\right\}\right]^{1/2}} \quad (1.23)$$

where $f_1(i,j)$ and $f_2''(i,j)$ are as defined above and N^2 represents the total number of pixels in the image region. A perfect matching between the images implies $|r|=1$, whereas completely uncorrelated images yields $r=0$.

1.8. Myocardial Imaging

Myocardial perfusion imaging is a non-invasive nuclear medicine technique used to diagnose the presence of lesions in the myocardium and to specify their location. Despite the quantitative potentials of SPECT imaging, this technique is normally used only qualitatively since the problem of photon attenuation within the thorax (amongst other factors) limits the accurate determination of activity concentrations. The following sections outline the most relevant aspects related to this technique.

1.8.1. Anatomy of the Heart

The heart, a muscular organ situated between the lungs, is considered the centre of the cardiovascular system. The function of the heart is to act as a pump to distribute oxygenated blood to the whole body and to redirect the deoxygenated blood towards the lungs for its oxygenation. The human heart is divided by a septum into two halves, right and left, and each half is further divided into two cavities, the atrium and the ventricle. The left ventricle is regarded as the cavity that plays the most important part when distributing the oxygenated blood to all the parts of the body and forms the largest part of the heart. The wall of the heart is divided into three layers:

- Epicardium is the thin, transparent outer layer of the wall and is composed of serous tissue and mesothelium,
- Myocardium is a cardiac muscle tissue which constitutes the bulk of the heart. It is responsible for the heart contraction.
- Endocardium is a thin layer of endothelium overlying a thin layer of connective tissue and it lines the inside of the myocardium.

The walls of the left ventricle are much thicker than those of the right ventricle, the proportion being approximately 3 to 1 (Gray 1988). As with any other tissue, the wall of the heart has its own blood vessels. The flood of blood that runs through the myocardium is known as the coronary circulation. The left and right coronary arteries are responsible for providing blood to the myocardium. The major branches of these vessels and the parts of the heart supplied by them with oxygenated blood are listed in table 1.2.

Table 1.2. Vessels that supply pure blood to the heart, their branches and places of irrigation.

Coronary vessels	Branches	Irrigation
Left Coronary Artery	Anterior Inter ventricular	Walls of both ventricles
	Circumflex	Walls of the left ventricle and left atrium
Right Coronary Artery	Posterior Inter ventricular	Walls of both ventricles
	Circumflex	Myocardium of the right ventricle

As expected, the left ventricle receives the most abundant blood supply because of the enormous work it must perform. When there is a reduced oxygen supply to any part of

the myocardium the cells can weaken producing a condition called myocardial ischemia. A most serious situation arises when the oxygen supply is completely interrupted (for instance due to a thrombus or embolus in one of the coronary arteries) and the cells die producing myocardial infarction. Either of these two conditions in which the heart receives an inadequate amount of blood because of an interruption of its blood supply is known as coronary artery disease (CAD). The symptoms of CAD can range from a mild chest pain to a much more serious problem as cardiac arrest. Therefore, it is very important to diagnose CAD in a very early stage to avoid fatal consequences to the patient.

1.8.2. Cardiovascular Nuclear Imaging

Among the techniques currently used to diagnose CAD, cardiovascular nuclear imaging has gained particular importance due to its non-invasive evaluation of cardiovascular physiology and function. Three types of procedure are normally performed in cardiac imaging: evaluation of coronary artery perfusion with ^{201}Tl or ^{99m}Tc, acute myocardial infarction imaging with ^{99m}Tc pyrophosphate and tests of ventricular pump performance. The last two procedures are normally used in a planar imaging protocol and they will not be described in this thesis.

1.8.3. Myocardial Perfusion Imaging with Thallium 201

Myocardial perfusion imaging is performed by applying a technique called stress-redistribution thallium imaging and its success relies on the fact that it might identify up to 80%-90% of cases with coronary artery disease. This technique has been used for the past 15 years with thallium 201 in the form of thallous chloride that concentrates in the myocardium by the process of the sodium/potassium pump. Thallium 201 is a radionuclide that decays by electron capture to mercury 201 with a half-life of 75 hours. The decay process leaves the mercury atom in an excited state with an inner electron orbit empty which is filled by another electron from an outer orbit. The electron transition produces characteristic x-rays with energies from 68 to 80 keV (94.5%). Thallium 201 is extracted by the myocardial cells after its injection in the venous bloodstream.

This process is followed by a redistribution (or equilibrium) period in which there is a continuous extraction and washout of thallium from the myocardium. The initial distribution of thallium depends on the regional coronary blood flow and on the

capability of myocardial cells to extract the radiopharmaceutical. Myocardial uptake is proportional to regional blood blow. This means that with normal patients the myocardial uptake must increase in direct proportion to oxygen demand. This situation arises when the patient is subjected to exercise or when the patient is injected with a pharmaceutical to simulate the physiologic effects of exercise. With patients presenting CAD there is usually normal myocardial blood flow at rest. However, when there is an increased demand for oxygen, the ability of the coronary vessels to increase blood flow is limited. This effect produces a varying thallium uptake in different regions of the myocardium. An area of regional ischemia or necrotic tissue creates a region in the image with diminished thallium uptake.

Thallium uptake also takes place in other tissues like the gastrointestinal tract, skeletal muscle, kidneys and lungs. The washout of thallium from these tissues allows the radiopharmaceutical to be re-extracted by the myocardium to produce the equilibrium stage. Lung uptake has provided guidance to clinicians to indirectly determine the likelihood of a patient with CAD. In normal subjects the lung uptake of thallium can approach a lung-to-heart activity ratio of about 30%. This index remains the same for the initial stress and redistribution studies. However, there has been reported an increased pulmonary ^{201}Tl activity post-exercise in patients with CAD. A patient is reported to present abnormalities when the lung-to-heart activity is greater than 37% (Mahmood *et at* 1992). The detection of an abnormal lung-to-heart ratio on stress improves the detection of CAD.

Myocardial perfusion imaging is normally carried out using the exercise-redistribution imaging technique in which the radionuclide is injected into the patient at peak exercise and images acquired. A rest study is performed approximately 3 hours post-stress with identical conditions as in the first acquisition. A comparison between the two sets of images is then carried out to detect CAD and determine its localisation and severity. Two modalities exist in this technique: planar and tomographic imaging.

1.8.3.1. Planar Imaging

Planar imaging requires a dose of approximately 70 MBq. The protocol includes the following projections: anterior view, left anterior oblique (LAO) view usually at 45°, and a left lateral oblique view, usually at 70°. Three patterns can be recognised in an abnormal thallium distribution: a) reversible abnormality caused by stress-induced ischemia, b) non-reversible or fixed abnormalities caused by acute or remote myocardial infarction, c) rapid washout or reverse redistribution that presents normal

stress images and abnormal rest images. Erroneous diagnoses of CAD with ^{201}Tl can be due to artefacts caused by photon attenuation (for instance in breast or adipose tissue) or patient motion. Thallium stress-redistribution planar imaging has proved to be a sensitive and a successful technique for determining the presence of CAD. However, it cannot determine the extent of disease in many patients due to the superposition of myocardial structures inherent to planar imaging.

1.8.3.2. Tomographic Imaging

SPECT imaging has replaced planar imaging due to its ability to identify the presence of CAD correctly, in particular for the identification of specific vessel (or multi-vessel) disease. SPECT thallium imaging requires an injected activity between 100 and 150 MBq. The marked photon attenuation within the thorax has led to many centres using 180° rather than conventional 360° rotational arc for myocardial tomographic studies. A 180° rotational arc is preferred over 360° so that more time is spent on the part of the body where a greater count rate from the heart is detectable. The patient is typically imaged with the gamma camera fitted with a LEGP collimator using a 64x64 matrix, 32 frames, 30 seconds per frame starting at 45° right anterior oblique (RAO) and ending at 45° left posterior oblique LPO.

1.8.3.3. Image Artefacts

Some artefacts can appear in the images due to the following parameters: soft tissue attenuation, overlying abdominal visceral activity, myocardial hot spots, apical variations, non-coronary disease, patient motion, reconstruction errors, centre of rotation errors and flood field non-uniformity (DePuey and Garcia 1989). Some of these artefacts can be corrected by the careful examination of the projections, by the application of very strict quality control protocol or by delaying image acquisition post-exercise.

Soft tissue attenuation results in areas of apparently decreased myocardial activity (referred to as defects). The most common soft tissue attenuation in women is the left breast. The location of a defect and its count density will depend on the size of the breast and on the positioning of the patient. Men with gynecomastia may also show this artefact. In obese patients the accumulation of adipose tissue in the chest may cause an increased lateral chest wall density. This accumulation results in an artificial fixed lateral wall perfusion defect. Patients with abdominal protuberance may cause attenuation showing a decrease in activity in the inferior wall. Artefacts due to tissue

attenuation have found no simple solution and more complicated schemes have to be applied. In this context, it is important to develop and to assess the feasibility of attenuation compensation methods to improve quantification. However, it has been recognised that attenuation corrections applied to studies in the thoracic region is a difficult task due to the large range of tissue attenuation coefficients within the thorax.

Relative quantification in myocardial perfusion imaging is normally performed by comparing the myocardial images with a library of myocardial perfusion images. The image library is created with normal patients diagnosed with non-coronary artery disease. This type of comparison partly compensates for the lack of corrections for scattering, variable attenuation and partial volume effects (DePuey and Garcia 1989).

1.8.4. New Radiopharmaceuticals

An important factor that enhances the effect of photon attenuation in myocardial perfusion imaging with ^{201}Tl is the low energy of the emitted x-ray photons which can be attenuated to half the original intensity with only 3.4 cm of soft tissue. This fact has lead a number of researchers to produce radio-labelled agents more suitable for myocardial imaging with the gamma camera. Technetium 99m is the radionuclide mostly used in nuclear medicine imaging due to its excellent properties: it emits monoenergetic gamma rays without particulate emission, has a relatively short half-life and, what it is more important, most of the gamma cameras are optimised to 140 keV photons.

New ^{99m}Tc-labelled agents have been developed and are currently undergoing clinical testing. The use of this radionuclide for myocardial perfusion imaging offers the advantage of emitting more energetic photons than thallium 201 and, therefore, less photon attenuation will occur within the thorax (e.g. a 140 keV photon beam is attenuated to half its original intensity with 4.3 cm of soft tissue). ^{99m}Tc isonitriles and boronic acid adducts of technetium oximes (BATOs) are radiopharmaceuticals which appear to behave similarly to ^{201}Tl, that is, the initial myocardial uptake is directly proportional to the regional blood flow. However, redistribution post-stress in the myocardium does not occur and a second injection is necessary for the rest study. Because ^{99m}Tc has a short half-life and there is a rapid washout from the body, a higher administered dose to the patient (which can be ten times larger than the utilised for ^{201}Tl) can be injected resulting in a higher image quality (Maddahi *et al* 1991).

CHAPTER 2

The Intrinsic Response of the Gamma Camera

The energy and spatial responses are the most important parameters that characterise a radiation detector. This project did not include the Monte Carlo simulation of the crystal, photomultipliers and related electronics of the gamma camera. However, their response had to be taken into account if quantitative data were to be generated. A procedure was implemented as a final step in the photon transport process to include the intrinsic response of the gamma camera based on experimental data. This chapter describes the experiments carried out to measure the intrinsic response of the gamma camera and the implementation of the algorithms in the Monte Carlo simulations.

2.1. Energy Response

A very important property of a detector in radiation spectroscopy is its response to a monoenergetic source of that radiation. The detection of x-ray or gamma-ray photons depends on the different photon interactions taking place within the material, because electromagnetic radiation does not ionize or excite directly the atoms of the material through which it passes. During these interactions, the photons transfer energy to the electrons in the absorbing material. These electrons, known as secondary electrons, start travelling through the medium losing energy through ionization and excitation of atoms or through bremsstrahlung emission. It is through the interaction of these electrons that the energy of the incident photon beam can be found.

A beam of monoenergetic photons impinging on the crystal of the gamma camera produces secondary electrons of many energies due to the different photon interactions taking place in the medium. As described previously, the electrons ionize or excite the atoms of the crystal producing isotropic emission of visible light, the number of visible photons being proportional to the energy deposited by the electrons. These scintillations give rise to a continuous distribution of pulse heights that is further broadened by statistical fluctuations. The scintillations are converted into an electrical

pulse using a photomultiplier tube, a device consisting of a photosensitive layer (photocathode) coupled to an electron multiplier structure. The photocathode converts light photons into electrons through the process of photoemission. The electron current generated is then amplified proportionally to the number of original photoelectrons and collected to generate a signal. A pulse-height spectrum can be formed by collecting the amplitude signals from different photon interactions independently and measuring the rate at which they occur.

The main characteristic of a typical pulse-height spectrum is the photopeak, that contains those events where the total energy of the incoming photons is absorbed in the scintillator. In the case of an incident photon energy lower than 1.02 MeV the photopeak includes primary photoelectric events accompanied by absorption within the scintillator of the resulting x-rays and Auger electrons and a primary Compton event accompanied by absorption of the Compton-scattered photon (Evans 1968).

In addition to the photopeak, a continuous distribution of lower photon energies is present. This part of the spectrum includes those events where the photons have been scattered with a subsequent loss of the scattered photon. The energy deposited in this case is lower than the mean photopeak energy and the statistical fluctuations associated with the production of light photons increase. The photon energies normally used in SPECT are within the ranges 50 to 360 keV and the features of more complex spectra produced with higher photon energies will not be described here.

The energy response of a detector is measured in terms of the energy resolution, R, defined as the full width at half maximum, FWHM, of the photopeak expressed as a percentage of the photopeak mean energy, that is:

$$\text{Energy Resolution } (\%) = R = \frac{\text{FWHM of the photopeak} \times 100}{\text{Peak Energy}} \qquad (2.1)$$

Clearly, a broadening of the photopeak at a given energy deteriorates the energy resolution, and vice versa. A scintillation detector has a poor energy resolution due to the combination of several factors that can be summarised as follows:

i) statistical noise arising from the discrete nature of photon emission,
ii) variation in production and collection of visible light over the detector active volume,
iii) charge collection statistics,

iv) electronic noise,

v) fluctuations in PM tube gain from event to event.

The statistical noise due to the discrete nature of photon emission will always be present independently of how good the detector response is and it fixes a minimum amount of fluctuation in the detector output. The combination of the factors *ii)* and *iii)* produce the most important loss of resolution in the detector. Assuming that these phenomena obey Poisson statistics, their overall contribution also obeys Poisson statistics. The statistical variations in the production of an output signal are photon energy dependent and it is expected that the standard deviation of the photopeak will be related to the incident photon energy, E_{in}, through the relationship:

$$\sigma = k\sqrt{E_{in}} \tag{2.2}$$

where k is a constant that depends on the characteristics of the detector (that is scintillator-PM combination). Assuming that the photopeak can be represented by a Gaussian function, the FWHM is:

$$FWHM = 2.35\sigma \tag{2.3}$$

By combining expressions 2.1, 2.2 and 2.3, the energy resolution can be written as:

$$R = \frac{FWHM}{E_{in}} = \frac{2.35k}{\sqrt{E_{in}}} \tag{2.4}$$

This relationship, although simple, cannot completely characterise experimental data due to the presence of non statistical sources of peak broadening. A more adequate representation of measured data that can include this effect is (Knoll 1989):

$$R = \frac{(\alpha + \beta E_{in})^{1/2}}{E_{in}} \tag{2.5}$$

The parameters α and β must also be determined for each scintillator-PM combination.

Equation 2.4 has been previously used to represent the broadening of the photopeak assuming a Gaussian shape (Manglos *et al* 1987a, Floyd *et al* 1984, Yanch *et al* 1992). In this thesis it was considered, however, that equation 2.5 would provide a better representation for the photopeak than equation 2.4. Equation 2.5 was therefore used in

this thesis to model the energy response of the gamma camera after the photon transport within the object and collimator had been performed.

Energy resolution is measured in the conventional manner using a multichannel analyser that has to be calibrated with standard γ-ray sources. Unfortunately, the energy resolution of the gamma camera depends, amongst other factors, on the position of the incoming gamma ray across the detector. Shifts in the position of the locally computed energy signal occur and normally energy corrections have to be applied. Results are presented in the following sections on the measurement of the parameters α and β to be used in the energy response implementation together with a study on the variation of the energy resolution across the gamma camera field of view. All the experiments were carried out at the Institute of Nuclear Medicine of UCL Medical School using an International General Electric (IGE) XCT gamma camera.

2.1.1. Measurement of the Energy Response

The intrinsic energy response of the gamma camera was measured for five radionuclides with photon emission energies between 73 keV and 159 keV. Table 2.1 lists the sources used in the experiment together with their main radiation characteristics (Mettler and Guiberteau 1991). Some of these sources were truly monoenergetic (^{99m}Tc and ^{123}I) but others had contributions from several energies (^{201}Tl, ^{67}Ga and ^{57}Co).

Each source was placed approximately 2 metres above the crystal with the gamma camera working in a pulse height analysis mode with the collimator removed. The maximum number of counts in the photopeak position was set as 30,000 and a cut-off energy appeared by default at 50 keV. Five spectra were recorded, one for each radionuclide, and then transferred to a Sun workstation for further analysis. The spectra (shown in figure 2.1) were calibrated using the ^{57}Co and ^{99m}Tc sources.

Table 2.1. Radionuclides used in the measurement of the energy response of the gamma camera.

Nuclide	Symbol	Half-Life	Decay Mode[a]	Major Radiations (MeV)[b]
Thallium 201	^{201}Tl	73.0 hr	E.C.	γ 0.135 (2%)[c]
				γ 0.167 (8%)
				x-ray Kα_2 0.069 (27.4%)[d]
				x-ray Kα_1 0.071 (46.6%)
				x-ray Kβ_1 0.080 (80.3%)
Gallium 67	^{67}Ga	78.1 hr	E.C.	γ 0.093 (38%)
				γ 0.184 (24%)
				γ 0.296 (16%)
Cobalt 57	^{57}Co	270.0 days	E.C.	γ 0.122 (86%)
				γ 0.136 (11%)
Technetium 99m	^{99m}Tc	6.0 hr	I.T.	γ 0.140 (88%)
Iodine 123	^{123}I	13.0 hr	E.C.	γ 0.159 (83%)

[a] E.C. = electron capture. I.T. = isomeric transition.
[b] Mean energy.
[c] Percentages of emission per disintegration.
[d] [Hg daughter x-rays 0.069-0.081, with mean at 0.073 MeV (94.4%/disintegration)]

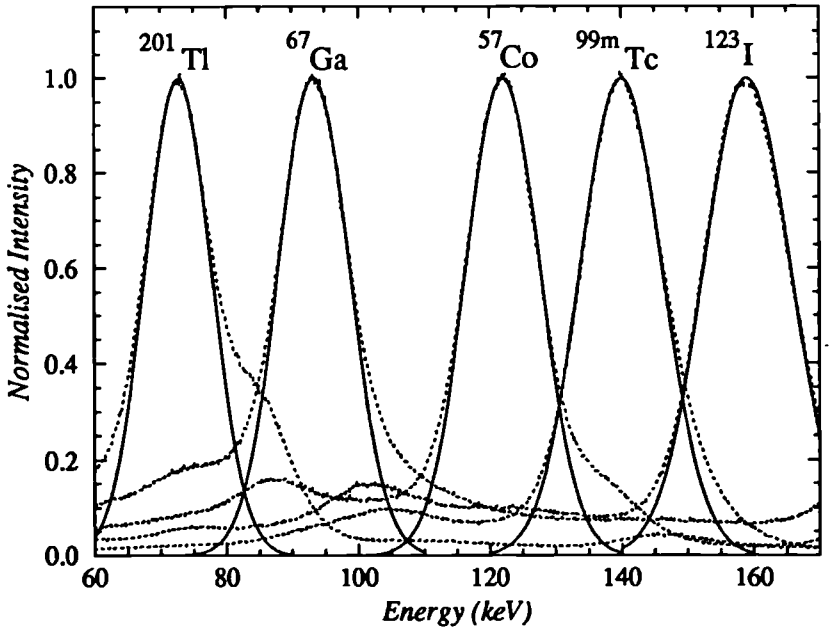

Figure 2.1. Plot of experimentally measured energy distributions for different radioisotopes. Gaussian fits to the photopeaks are shown in solid lines.

2.1.1.1. Sampling of the Energy Response

In order to find the parameters α and β from equation 2.5, the photopeaks were fitted with Gaussian functions, giving as results the values of photopeak mean energy and FWHM shown in table 2.2 for each radionuclide.

Table 2.2. Parameters found in the Gaussian fits to the photopeaks.

Nuclide	Mean (keV)	FWHM (keV)	Resolution (%)
Thallium 201	72.7	11.7	16.0
Gallium 67	93.3	12.6	13.5
Cobalt 57	122.1	13.9	11.4
Technetium 99m	140.0	14.5	10.4
Iodine 123	159.1	15.5	9.7

The FWHMs^2 were plotted against the photon mean energy and the data fitted with a straight line. The parameters α and β were obtained from the intercept and slope of the straight line that resulted from this plot; in this case $\alpha = 49 \pm 6$ and $\beta = 1.18 \pm 0.05$.

These parameters were used to determine a detected energy, E_{det}, for every photon hitting the crystal plane by assuming a Gaussian shape for the photopeak and using the direct sampling method (see Appendix 2). The procedure to determine E_{det} can be summarised as follows:

1.- The cumulative probability function, $F(E')$, for a normalised Gaussian distribution of the form:

$$f(E') = \frac{1}{\sqrt{\pi}} \exp\left(-E'^2\right) \qquad (2.6)$$

was evaluated within the interval $-4\sigma \leq E' \leq 4\sigma$ and stored in an array. In this equation E' is simply a dummy variable. With this single function any other Gaussian distribution with mean E_{in} and standard deviation σ was then generated by applying the transformation:

$$E' = \frac{\left(E_{det} - E_{in}\right)}{\sqrt{2}\sigma} \qquad (2.7)$$

where E_{in} is identified as the incident energy of the photon hitting the crystal plane and σ is the standard deviation which had to be selected according to the value of E_{in} using equation 2.5. With this procedure there was no need to generate a cumulative probability distribution for each incident photon energy.

2.- The dummy variable E' was sampled from $F(E')$ using the direct sampling method.

3.- The detected signal, E_{det}, was then obtained from equation 2.7 as:

$$E_{det} = \sqrt{2}\sigma E' + E_{in} \tag{2.8}$$

where:

$$\sigma = \frac{FWHM}{2.35} = \frac{\sqrt{\alpha + \beta E_{in}}}{2.35} \tag{2.9}$$

2.1.2. Variation of the Energy Response with Position

An experiment to assess the variability of the energy response as function of position on the surface of the gamma camera was carried out. In order to ensure reasonable statistics in the collected data, a ^{57}Co point source was used in the experiment due to its long half-life. A ^{99m}Tc energy correction was used during the experiment. This energy correction was used instead of the one for ^{57}Co because the latter has two main photon radiations, one at 122 keV (86%) and the other at 136 keV (11%). The photon emission at 136 keV causes the photopeak to appear asymmetric, making it very difficult to find an appropriate energy correction matrix.

The source was placed at approximately 2 metres above the uncollimated crystal to obtain near parallel beam conditions. A set of 25 images was acquired in a 64x64 format setting different energy window centres (ranging between 80.5 and 139 keV) and fixing a narrow window width. A fixed image acquisition time of 144 minutes was used and no correction due to the exponential decay of the source was applied. The energy responses of 2472 pixels contained in the geometric field of view, GFOV, were obtained by plotting the number of counts contained in each pixel as a function of window centres.

To clarify this idea, figure 2.2 shows the "averaged" gamma camera energy response measured for ^{57}Co by taking into account the response of all the pixels in the GFOV. The vertical dotted lines indicate the lower and upper limits of the windows used during the image acquisition. Since the gamma camera allowed only integer values for the upper and lower window limits, it was not possible to set a constant window width for all the acquisitions. The energy window width took the values of 2 or 3 keV depending on the value of the window centre.

Typical energy spectra for individual pixels obtained with these measurements are shown in figure 2.3. All the photopeaks were asymmetric with respect to the photopeak mean energy. This was in part expected because of the presence of a second gamma ray emitted with an energy of 136 keV.

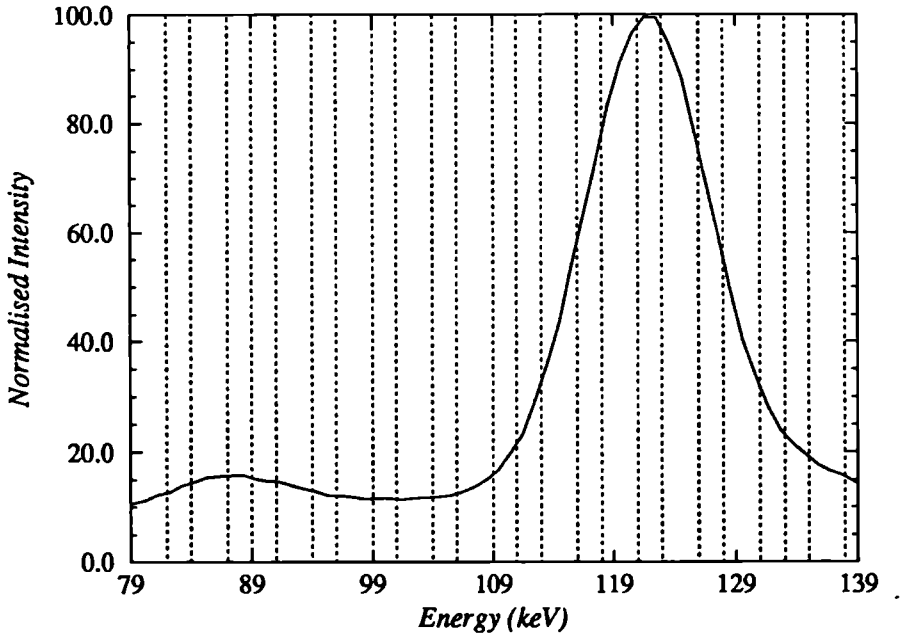

Figure 2.2. Averaged energy response of the gamma camera to ^{57}Co. The vertical dotted lines indicate the lower and upper limits of the windows used during the image acquisition.

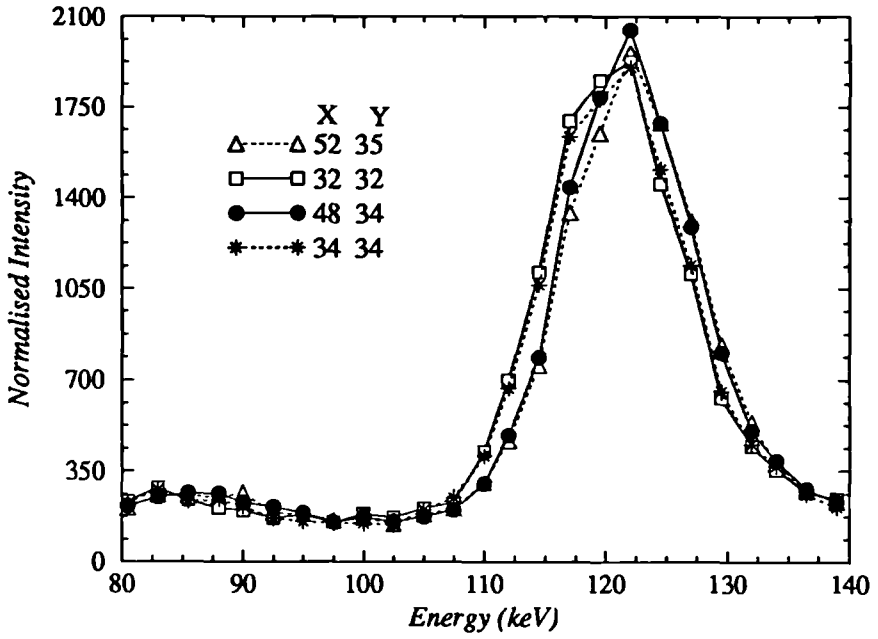

Figure 2.3. Typical examples of the energy response of the gamma camera to ^{57}Co for several pixels. The *X* and *Y* pixel numbers in the graph give the location of the pixel in the image where the energy distribution was measured.

2.1.2.1. Determination of Energy Resolution.

A Gaussian function was fitted to the photopeak of the energy spectrum of each pixel on the basis of the minimisation of the χ^2 criterion for data within the range 110 keV and 140 keV. Several parameters which characterise the photopeaks were obtained: photopeak mean value, FWHM and energy resolution. Figures 2.4a, 2.4b and 2.4c show the histograms of the number of pixels exhibiting a given value as a functior of photopeak mean value, FWHM and energy resolution, respectively.

It can be observed that more than 90% of the pixels can be classified into two groups referred to as class A and class B. Class A is composed of those pixels with photopeak mean values around 121.4 keV. These pixels present not only lower photopeak values, but wider FWHM (mean value around 14.2 keV). The energy resolutions associated with these pixels have a mean value of 11.7%. The pixels of class B present photopeak mean values around 121.9 keV, FWHM of the order of 13.4 keV and energy resolutions around 11.0%. It is clear that the energy response of the detector is better for pixels in class B.

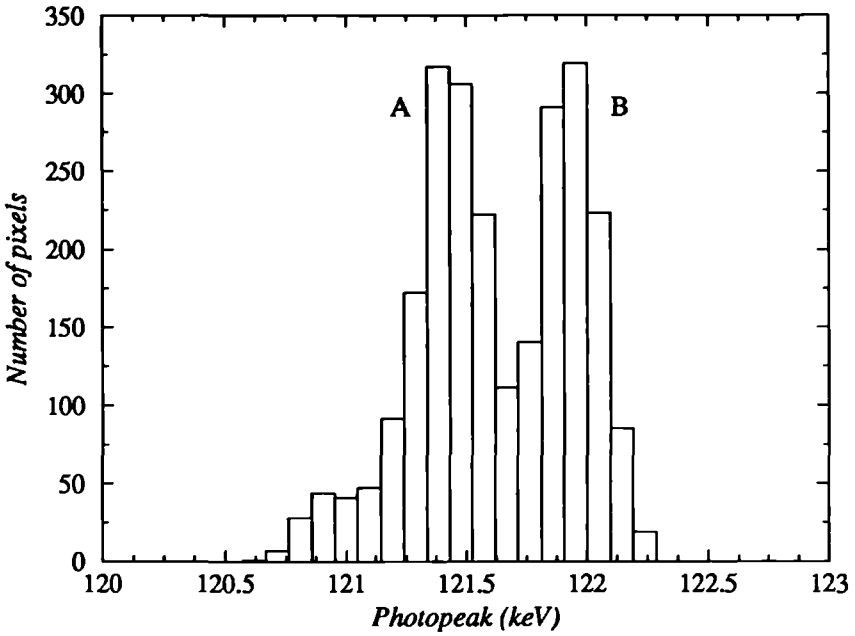

Figure 2.4a. Histogram of the mean photopeak values. Two peaks are clearly differentiated. They are labelled as class A and class B.

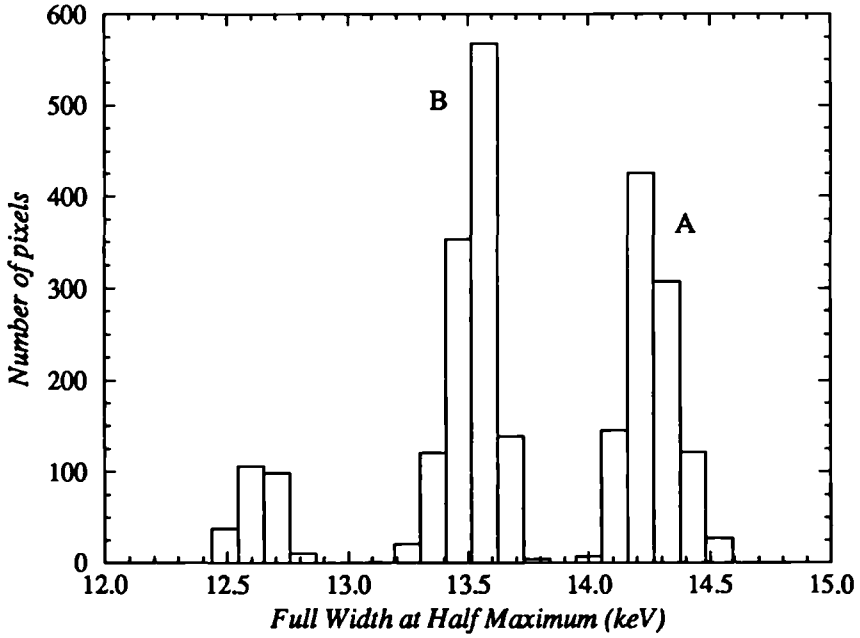

Figure 2.4b. Histogram of the FWHMs.

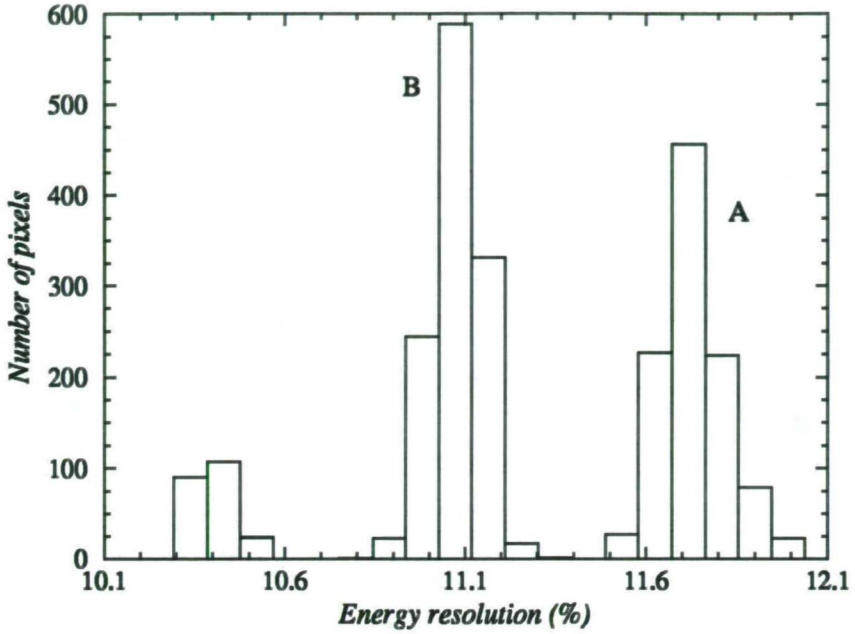

Figure 2.4c. Histogram of the energy resolutions.

It is interesting to note that the class A pixels lie within the central and outer regions of the gamma camera. This is shown in figure 2.5 where the grey scale image represents the spatial distribution of the energy resolutions over the surface of the gamma camera. In this image, the black pixels are associated to good energy response whereas the white pixels are related to poor energy response of the gamma camera. This particular distribution might be an effect of using an energy correction matrix for 140 keV instead of the one required for 122 keV.

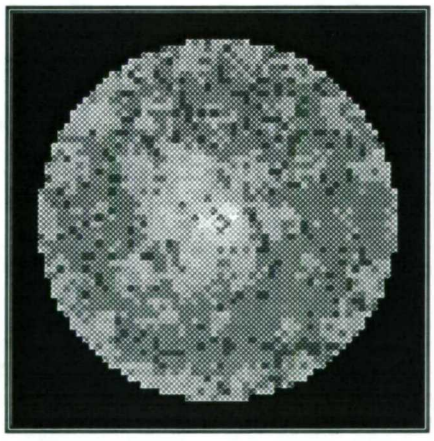

Figure 2.5. Spatial distribution of the pixels as function of energy resolution. The white pixels represent poorer and the black pixels better energy response of the gamma camera to ^{57}Co.

2.1.2.2. Discussion

The results from the previous section show that variations in the photopeak mean value occur over the gamma camera GFOV and are of the order of 0.5 keV for ^{57}Co. The energy resolution is therefore affected and it also changes as a function of position. Strictly speaking, the matrix used in the energy correction for a given nuclear medicine study must be measured specifically for the photon energy used. However, this procedure is sometimes difficult to accomplish because there are very few monoenergetic sources available and the normal practice is to use the energy correction for ^{99m}Tc whenever possible. A more complex situation arises in imaging an extended object because a whole distribution of photon energies hit the detector due to scattered radiation.

The ideal energy response to be included in the Monte Carlo simulation would imply measurement of the energy response of the gamma camera for a whole range of photon energies as function of position. However, it is not possible to implement this sort of correction due to experimental limitations. Furthermore, it was calculated that a shift in the photopeak mean energy of 0.5 keV reduces the number of detected photons in less than 0.5% when using either a 10% or a 20% energy window. The loss in detection efficiency can therefore be considered negligible. For this reason, it was assumed in the Monte Carlo simulations that the gamma camera energy response is uniform across its field of view.

2.2. Intrinsic Spatial Response

It has already been pointed out that the conversion of energy of the incoming photons into an electronic signal is a complicated process. The photons interact with the crystal and deposit energy. This energy is transformed into visible light that then reaches the photomultiplier tubes and is converted into suitable electronic signals. Statistical fluctuations in the distribution of light photons between the photomultiplier tubes from one scintillation event to the next, light losses in the transport of light to the photomultipliers and misplacement of events due to multiple scattering of photons within the crystal are examples of what can happen in the process of energy conversion that affect the overall spatial resolution of the system. Because of this, it is not unexpected that the detector produces blurred rather than sharp images of sharp edges or small point objects.

The intrinsic spatial resolution of a gamma camera refers to the limitation of the crystal and related electronics to resolve point sources placed close to each other. The intrinsic resolution depends on the crystal thickness because with thicker detectors there is greater spreading of scintillation light before it reaches the photomultiplier tubes. At the same time, the intrinsic resolution becomes worse with decreasing energy of the incoming photons; lower energy photons produce fewer light photons per scintillation event and a smaller number of light photons results in larger relative statistical fluctuation in their distribution.

Intrinsic resolution is normally characterised by the measurement of the detector response to a radioactive line source. This is referred to as the line spread function, LSF, and it is normally quoted in terms of full width at half maximum. The latter figure does no characterise completely the LSF and often the full width at tenth maximum, FWTM, is also given. This is particularly important when the line spread function is measured in the presence of a scattering medium since scattered radiation causes a broadening of the line spread function tails.

2.2.1. From LSF to PSF

The spatial response of an imaging system is characterised by the point spread function in the spatial domain or the modulation transfer function in the frequency domain. The point spread function is defined as the radiation intensity distribution in the image plane of a point source radiating with unit intensity (Rossmann 1969). An ideal system should produce a sharp image of a point source, which can be represented with a delta function. However, ideal systems do not exist and the images of point sources are blurred intensity distributions, the degree of blurring will depend on the characteristics of the system.

Any source distribution can be thought of as resulting from the sum of unit point sources. If the imaging system is linear and shift invariant, an image of this distribution can be represented by the sum of all the corresponding point spread functions over the entire image plane. This is known as the superposition principle of linear imaging. One can make use of this principle and introduce the intrinsic spatial response of the gamma camera into the Monte Carlo simulations as an additional procedure. In order to achieve this it is necessary to know the point spread function of the gamma camera. If the PSF is known, it is then straightforward to predict how the process of detecting one photon will produce a blurred intensity distribution in the image plane.

The measure of the point spread function is difficult to carry out in practice because of limitations with the instrumentation. An alternative characterisation of the spatial response can be obtained through the line spread function which is simply the integration of the PSF along one direction. The line spread function completely characterises a rotationally symmetrical and shift invariant imaging system. Because the gamma camera meets the latter requirements (to a good approximation), the line spread function is normally used to characterise its intrinsic spatial response.

The derivation of the PSF from the LSF is a complicated process, especially for systems without rotational symmetry. Marchand in 1964 depicted a method to obtain the PSF of a system that has rotational symmetry from the corresponding LSF by solving an integral equation. The method consisted of the mathematical manipulation of the equation that relates the LSF with the PSF. This algorithm was used in this thesis to obtain the gamma camera PSF from experimental measurements of the LSF.

As an example of the use of this algorithm, figure 2.6 shows both the line spread function measured for 140 keV photons and the point spread function calculated using Marchand's algorithm. The three-dimensional representation of the PSF is also shown in figure 2.7. The implementation of the intrinsic spatial response of the detector into the simulations was carried out through the digital convolution of the three-dimensional representation of the PSF with the Monte Carlo generated images.

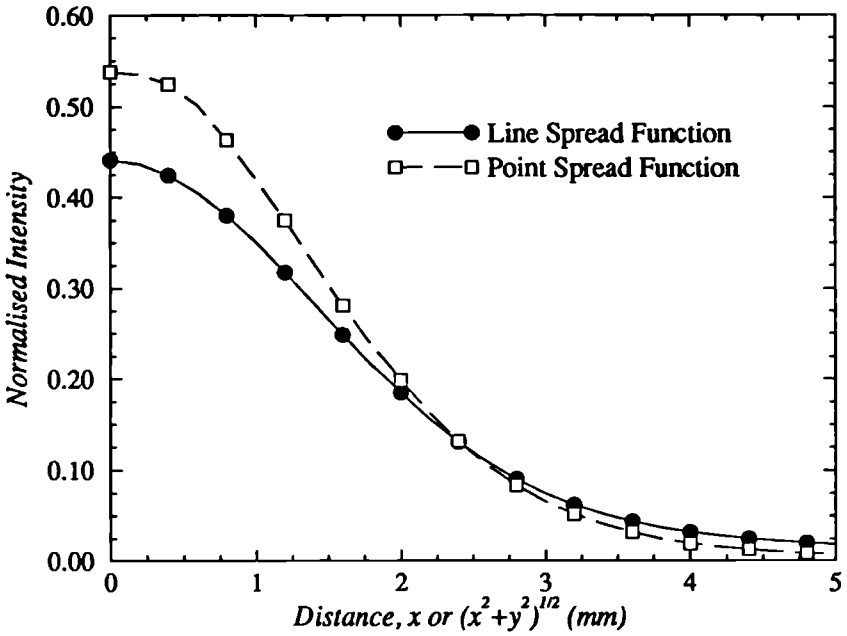

Figure 2.6. Example of the line spread function measured for 140 keV photons (10% energy window) and the point spread function calculated according to Marchand (1964).

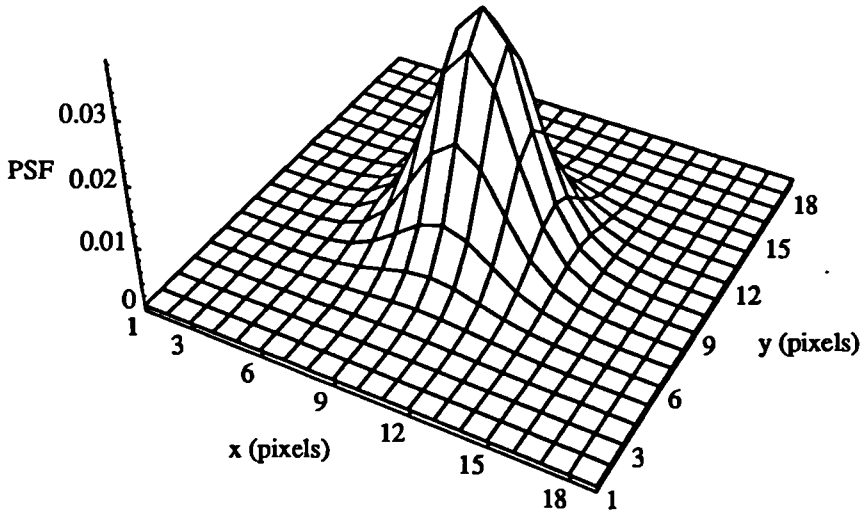

Figure 2.7. Three-dimensional representation of the point spread function.

2.2.2. Measurement of the Intrinsic Spatial Resolution

The measurement of the intrinsic spatial resolution of the IGE XCT gamma camera was carried out using a NEMA transmission phantom with slits of 0.5 mm thickness (NEMA 1980). An uncollimated ^{99m}Tc point source was positioned vertically above the centre of the phantom at a distance of 2 metres to obtain near parallel beam conditions. The phantom was placed centrally on the uncollimated gamma camera and its orientation adjusted so that its slit axis was aligned parallel to the *Y* axis of the gamma camera. Alignment was achieved by performing a set of short test acquisitions until the centroids of the profiles of the central line image in the top, centre and bottom coincided in the same *X*-pixel channel.

The images were acquired in a 1024x16 format until the maximum number of counts was greater than 10^4. Calibration of the pixels was accomplished using the physical separation between the slits and the mean value of the peaks (in channels). Once the system was aligned, the variation of the spatial resolution was studied as function of photon energy and window width.

All the acquired images were transferred to a Sun workstation for further analysis. To obtain the line spread function, 4 horizontal profiles were added. The central slit of the NEMA phantom was chosen as the representative LSF of the gamma camera since this position should suffer minimal distortion (Elliott *et al* 1986).

2.2.2.1. ^{133}Xe and ^{99m}Tc Spatial Response

In order to compare the LSF produced with different photon energies, two measurements were carried out using ^{133}Xe (81 keV) and ^{99m}Tc (140 keV). It was also important to use different energy windows because a larger energy window implies the inclusion of events with more statistical fluctuations in the production of light photons. The increase in statistical fluctuation in the light photons produces a greater uncertainty in the determination of the photon position. A 20% window centred in 81 keV was set for ^{133}Xe. Two energy windows of 10% and 20% were used for ^{99m}Tc, centred at 140 keV. Figure 2.8a shows the experimental LSF and figure 2.8b shows the calculated PSF. The parameters that characterise both the LSF and the PSF are shown in table 2.3.

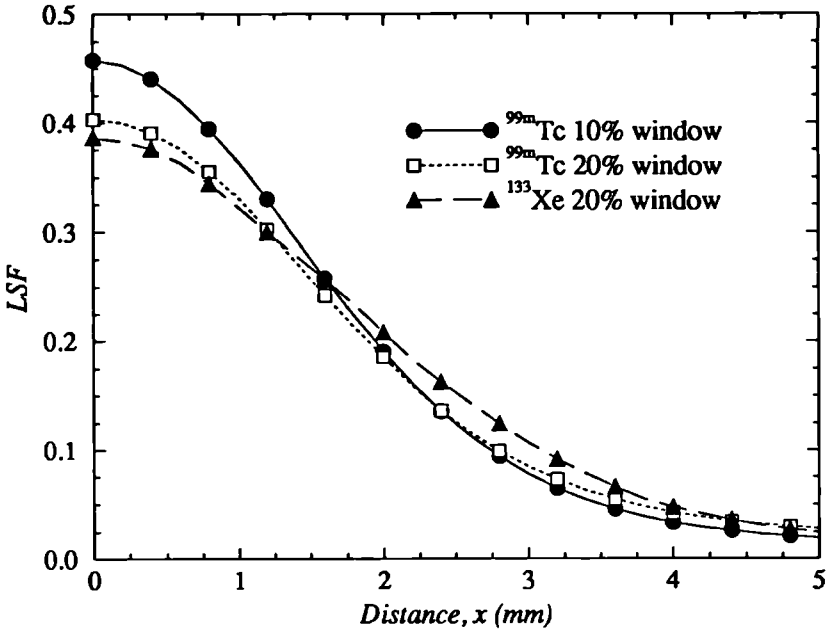

Figure 2.8a. Line spread functions measured for ^{133}Xe and ^{99m}Tc.

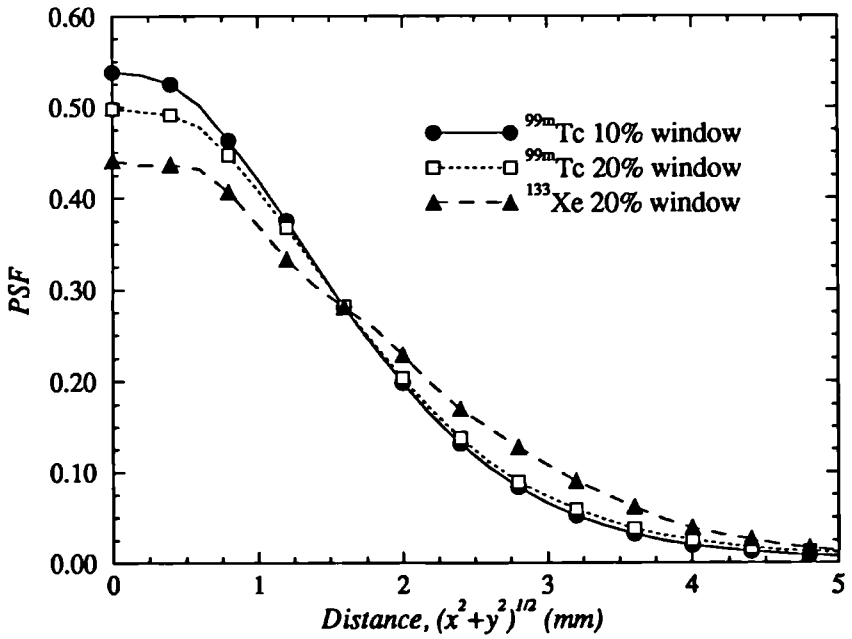

Figure 2.8b. Point spread functions calculated for ^{133}Xe and ^{99m}Tc.

Table 2.3. Experimental results of the intrinsic spatial resolution of the gamma camera for two sources. The estimated error in the measurement of FWHM was ±0.15 mm.

			LSF		*PSF*	
Source	Photopeak (keV)	Energy window (%)	FWHM (mm)	FWTM (mm)	FWHM (mm)	FWTM (mm)
^{133}Xe	81	20	4.2	8.6	4.2	7.6
^{99m}Tc	140	10	3.5	7.2	3.3	6.6
^{99m}Tc	140	20	3.8	8.2	3.5	6.7

It can be observed from figure 2.8 and table 2.3 that the LSF measured for ^{133}Xe presents a wider spread than either of the two energy windows used for ^{99m}Tc. This effect is reflected in the values of the FWHM and FWTM. The major difference between the PSF for the two energies (81 and 140 keV) occurs when comparing ^{99m}Tc (10% window) and ^{133}Xe in which the FWHM differed by 26% and the FWTM by 20%. When comparing the ^{133}Xe PSF with ^{99m}Tc (20% window) the differences reduced to 18% and 13%, respectively.

The difference in spatial response for ^{99m}Tc with 10% and 20% energy windows is barely noticeable. The spatial resolution of the narrow energy window is slightly better than the one for the wider window. The FWHM changes by 6.5% and the FWTM by 5.8%.

However, the differences in spatial resolution shown above do not have an important effect on the overall system resolution. Assuming that the spatial resolution of the collimator has a FWHM of 10 mm for a source-collimator distance of 10 cm, the overall system resolution is 10.8, 10.5 and 10.6 mm for ^{133}Xe, ^{99m}Tc (10% window), ^{99m}Tc (20% window), respectively. Since these values differ by less than 3%, the intrinsic response of the gamma camera can be characterised with a single value independently of the photon energy or the window width. This assumption is valid only for the range of energies considered in this study.

In this work, the energy of the primary photons was chosen between 75 keV and 180 keV and all image acquisitions were simulated using a 20% energy window. Based on the arguments given above, the PSF calculated for ^{99m}Tc (20% window) was chosen as the representative intrinsic spatial response of the gamma camera.

2.3. Conclusions

This chapter presented the measurement of the energy and intrinsic spatial response of the gamma camera and described the algorithms implemented in the Monte Carlo simulations to account for the photon detection process. It was shown that the energy response depends on the energy of the primary photon energy and on the position where the photons are detected across the gamma camera crystal. Differences in photopeak mean values of up to 0.5 keV occur when measuring energy spectra for ^{57}Co (122.1 keV) with a ^{99m}Tc energy correction matrix. However, a shift in the photopeak mean energy of 0.5 keV only reduces the number in detected primary photons in less than 0.5 %. The loss in detection efficiency can therefore be considered negligible and the energy response of the gamma camera can be assumed uniform across the field of view.

The intrinsic spatial resolution of the gamma camera, characterised by the line spread function, was also measured. The calculated PSFs showed small differences between the several cases considered and their contribution to the overall system resolution were essentially equivalent. On this basis, the PSF calculated for ^{99m}Tc (20% energy window) was chosen as representative of the intrinsic response of the gamma camera.

CHAPTER 3

Monte Carlo Simulation of a Parallel Hole Collimator

This chapter presents the properties that characterise the collimator performance and describes the computer simulation of a low-energy, general-purpose collimator (LEGP) with hexagonal holes. Comparison with analytical expressions and an experimental validation of the program are presented. In the former case, the collimator program is used to calculate the point spread function assuming an ideal detector response and the results are compared with both Anger's equation for collimator resolution and the collimator geometric response function, GRF. The GRF is an analytical expression for the geometric component of the collimator point spread function. The experimental verification involved the simulation of photon transport from a source distribution embedded in a scattering medium through the collimator to the camera where the effect of the intrinsic response of the gamma camera was included. Comparisons of these results with experimental data obtained from such a source are shown.

3.1. Gamma Camera Collimators

It has been discussed in Chapter 1 that the use of a gamma camera to obtain a planar projection of a three-dimensional source distribution requires that the photons emitted from the object arrive at the detector in a predictable manner. The formation of an image relies on relatively crude collimation that excludes from the detector most of the gamma rays which are not travelling in a particular direction with respect to the crystal plane. Typical photon energies used in SPECT imaging require the collimator to be constructed using very high atomic number materials to stop most of the unwanted radiation and keeping the photon penetration to a minimum level (normally below 5%). Most collimators are made of a 94%-6% lead-antimony alloy. The lead absorbs unwanted radiation and the small amount of antimony is added to provide mechanical strength.

The parameters that characterise a collimator are: hole size and shape, collimator length and septal thickness. These values are normally chosen by optimising both the spatial resolution and collimator efficiency for a particular photon energy range. Spatial resolution refers to the ability of an imaging system to differentiate two point sources close to each other. Collimator efficiency refers to the fraction of isotropically emitted gamma rays from a point source that are appropriately collimated (Moore *et al* 1992). Four types of collimators are normally used in nuclear medicine: pinhole, parallel hole, diverging and converging. All these collimators but the pinhole are multiple arrays of holes drilled or cast in lead; the orientation of the holes may be parallel, diverging or converging. A pinhole collimator consists of a lead cone with a pinhole aperture in the apex. A revision of collimator types and performances can be found elsewhere (Sorenson and Phelps 1987, Sharp *et al* 1985).

3.2. Parallel Hole Collimators

A parallel hole collimator consists of a multiple array of holes drilled or cast in lead, parallel to each other and perpendicular to the crystal face. The projected image has a one to one correspondence with the object. The most common parallel hole collimator has hexagonal hole shape which offers a stronger structure and higher efficiency as compared to collimators with circular or square holes. The efficiency of the parallel hole collimator does not depend on the source-collimator distance because the loss of photon flux at increasing distance is compensated for with an increase on the viewing area of the collimator. However, the spatial resolution deteriorates with increasing source-collimator distance. The performance of a collimator is measured in terms of the geometric efficiency and collimator spatial response. The parameters that determine the collimator performance are septal thickness (T), collimator length (L) and hole size (D). These parameters are shown in figure 3.1.

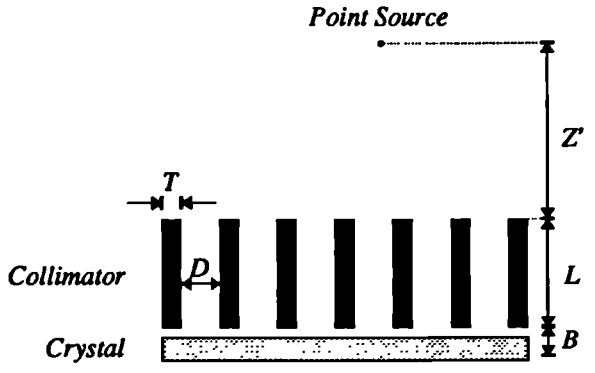

Figure 3.1. Section view of a parallel hole collimator.

3.2.1. Geometric Efficiency

The geometric efficiency (g) of a parallel hole collimator was first derived by Anger (1964). A modification of the original formula to account for septal penetration is given by:

$$g = k\left[D^2 / L_e(D+T)\right]^2 \qquad (3.1)$$

where D and T are as defined in figure 3.1, L_e is the effective collimator length ($L_e = L - 2/\mu$, μ is the linear attenuation coefficient of the collimator material for the particular photon energy) and k is a factor that depends on the shape of the hole and on their distribution pattern. For hexagonal holes closely packed its value is 0.263 (Moore *et al* 1992). It can be seen from equation 3.1 that geometric efficiency can be increased by increasing the size of the holes, decreasing the collimator length or decreasing the septal thickness. However, an improvement of the geometric efficiency leads to a deterioration of the collimator spatial resolution, as will be shown in the next section.

3.2.2. Collimator Response

In the ideal case an imaging system should be linear and shift invariant, that is, the response of the system must be directly proportional to the input signal, and the output must be independent on the location of the input (Barrett and Swindell 1981). The collimator is not a shift invariant system since when imaging a point source, its response depends on the location of the source with respect to the hole array pattern (Anger 1964). A practical way of eliminating this positional dependence is by defining an effective response function given by the image formed by a point source when the collimator is uniformly translated but not rotated (Metz *et al* 1980). According to this definition, the formation of the effective point spread function requires that all the elements of the imaging system be held fixed except for the collimator. An equivalent method to obtain the effective point spread function is by averaging point source images formed at several source positions with respect to the two-dimensional collimator pattern.

The collimator effective point response function contains three components that depend on the trajectories of the detected photons. The geometric component is formed by all those photons that pass geometrically through the collimator holes

without entering any septa. The penetration component is due to photons that penetrate the collimator septa without interacting. Finally, the scatter component is due to photons that scatter at least once in the collimator septa before detection. The geometric component does not depend on the collimator material, detector or radioisotope, it depends only on the geometric characteristics of the collimator. The penetration and scatter components depend on the collimator material, geometry (hole size, septal thickness and collimator length) and photon energy.

The geometric response function for parallel hole collimators can be calculated analytically in terms of source-detector distance, collimator thickness and hole size (Metz *et al* 1980, Barrett and Swindell 1981, Zeng *et al* 1991). The penetration and scatter components can be determined by using ray tracing techniques (Muehllehner and Luig 1973, Beck and Redtung 1985) and Monte Carlo simulations (deVries *et al* 1990, Rosenthal and Henry 1990), respectively.

3.2.2.1. Anger's Equation

Anger's (1964) expression for the collimator resolution expressed as the full width at half-maximum (FWHM) of the point spread function is

$$R_{(FWHM)} = \frac{D(L+B+Z')}{L} \tag{3.2}$$

where D is the hole size, L is the collimator length, B is the detector-collimator distance and Z' is the source-collimator distance (see figure 3.1). Equation 3.2 was derived from simplistic geometric considerations and does not take into account septal penetration or collimator scatter. Although useful to indicate the overall performance of the collimator response, it does not provide the shape of the point spread function. The next section examines the mathematical formulation of the collimator geometric response that predicts the probability that a photon traverses the collimator as a function of the photon direction.

3.2.2.2. Geometric Response Function

The geometric response function is defined as the photon fluence distribution on the detector plane determined by the geometric aperture of the collimator holes. It has been calculated analytically in terms of collimator thickness, hole size and source height for parallel, cone and fan beam collimators (Metz *et al* 1980, Barrett and

Swindell 1981, Zeng *et al* 1991). The total photon fluence as given by Zeng *et al* (1991) for circular holes of radius R is of the form

$$\Phi(r_T)=\left(\frac{R^2}{C}\right)\left(2\cos^{-1}\left|\frac{r_T}{2R}\right|-\left|\frac{r_T}{2R}\right|\sqrt{1-\left|\frac{r_T}{2R}\right|^2}\right) \tag{3.3}$$

where

$$r_T=\frac{L}{Z}|\mathbf{r}-\mathbf{r}_0| \tag{3.4}$$

In this equation it is assumed that a point source is located at a distance Z from the image plane (corresponding to the XY plane) and that the collimator, of thickness L, is parallel to the XY plane. $\mathbf{r}_0$ is the projection of the point source onto the XY plane and $\mathbf{r}$ represents the intersection of a photon trajectory with the image plane (this vector can be calculated from geometric considerations). Figure 3.2 shows schematically all these parameters.

Equation 3.3 also applies for cone and fan beam collimators. However, the variable r_T for these cases has a more complicated form and its value depends, among the variables shown above, on the distance between the collimator focal point and the detector plane (Tsui and Gullberg 1990, Zeng *et al* 1991).

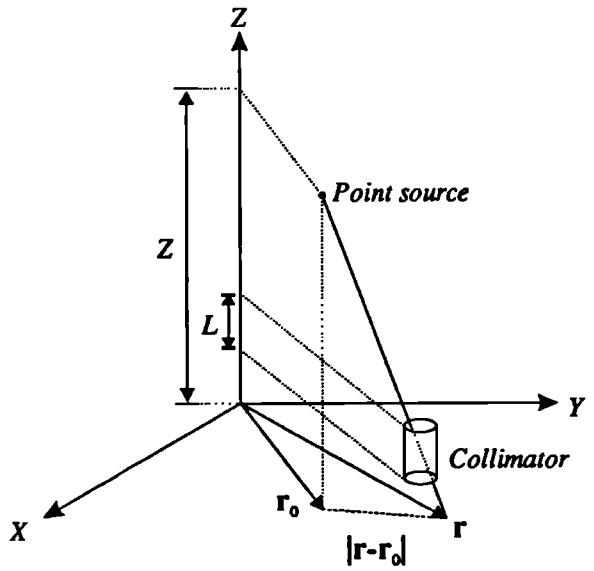

Figure 3.2. System of coordinates and parameters used to calculate the geometric response function. The detector is assumed to lie on the XY plane.

Note that $|\mathbf{r}-\mathbf{r}_0|$ represents the magnitude of the vector $(\mathbf{r}-\mathbf{r}_0)$ that lies in the *XY* plane. This quantity depends on the photon direction with respect to the normal vector of the detector plane and on the source height (measured from the detector plane). The geometric response function shown in equation 3.3 is shift invariant and rotationally symmetric due to the $|\mathbf{r}-\mathbf{r}_0|$dependence.

The derivation of the collimator geometric response function assumed a collimator with circular holes. However, it has been shown (Metz *et al* 1980) that the shape of the effective point spread function for a hexagonal hole is approximately equal to that of a circular hole. Because the mathematical formulation calculates the projected area onto the image plane, it is natural to think that when the formula is applied to a hexagonal hole collimator, the area of the hexagon must match that of a circular hole. To calculate the radius of an equivalent circular hole, *R*, let *DF* represent the hexagonal hole size flat-to-flat (see figure 3.3). The area of the hexagon as a function of the parameter *DF* is given by:

$$A_h = \frac{\sqrt{3}}{2} DF^2 \tag{3.5}$$

Therefore, a circle with the same area will have radius:

$$R = \frac{\sqrt[4]{3}}{\sqrt{2\pi}} DF \tag{3.6}$$

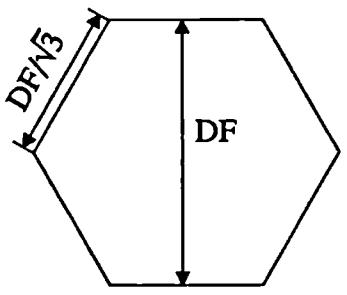

Figure 3.3. Flat-to-flat distance (*DF*) and sidelength of a hexagonal hole.

The parameter *C* in equation 3.3 is a normalisation factor that can be found by calculating $\Phi(0)$, that is, the photon fluence for photons travelling perpendicular to the detector plane. In the case of a hexagonal hole collimator, the average number of detected photons will be proportional to the ratio of the area of the hexagonal hole and

the area of the hexagonal hole surrounded by half the septal thickness of the collimator material. For photons travelling perpendicular to the image plane r_T equals zero and therefore

$$\Phi(0)=\frac{\pi R^2}{C} \tag{3.7}$$

The value of the normalisation factor C for a hexagonal hole collimator is given by:

$$C=\frac{\sqrt{3}}{2}(DF+T)^2 \tag{3.8}$$

where DF is the hole size flat-to-flat and T is the septal thickness.

3.3. Monte Carlo Simulation of a LEGP Collimator

It has been discussed in section 3.2.2 that the collimator response to a point source is the sum of three components: geometric, penetration and scatter. The most accurate investigation of these components is by using Monte Carlo simulation in which photon propagation is carried out using the probability of photon interactions for the appropriate photon energy and medium. Monte Carlo techniques offer the great advantage of performing analogue photon transport, that is, every photon is independently traced and its history can be recorded at every single step. In this way, a photon can be classified in terms of the number of interactions it has undergone in an attenuating medium or whether it has passed through without being disturbed. The technique provides information on the geometry, photon parameters (position, direction, energy) and sites of interactions at all times, allowing all the components of the collimator response to be found. It appears useful to use this technique to investigate the performance of a parallel hole collimator.

3.3.1. Program implementation

A parallel hole collimator has a periodic pattern determined by a unit cell. The unit cell is defined as that portion of the collimator used to tessellate the desired pattern over the entire collimator face (Beck and Redtung 1985). The hexagonal hole structure and the unit cell used in the program are shown in figure 3.4.

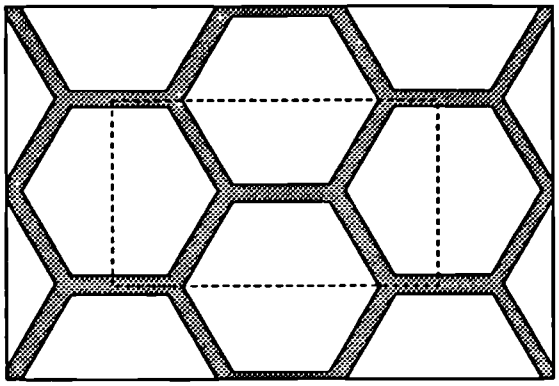

Figure 3.4. Section of the front face of the hexagonal hole collimator. The area delimited with the dashed line represents the unit cell.

The unit cell is a three-dimensional structure which can be represented by the intersection of several planes forming polyhedra. Each of these polyhedra defines a region in the unit cell filled with either lead or air. In the program, every region is defined by a set of planes and it is associated with a given medium. Each plane separates neighbouring regions. To illustrate this, let us divide the unit cell into 13 regions as shown in figure 3.5. Regions 2, 6, 8 and 12 contain air and the rest of the regions contain lead. The figure also shows a magnified view of region 5, which is defined by four planes P_1, P_2, P_3 and P_4. A photon travelling within this region can intersect any of these planes depending on its direction cosines. The program checks which plane the photon will hit and performs the photon transport. Assuming that the photon intersects plane P_1 then the photon is transported to this plane and continues travelling within region 8.

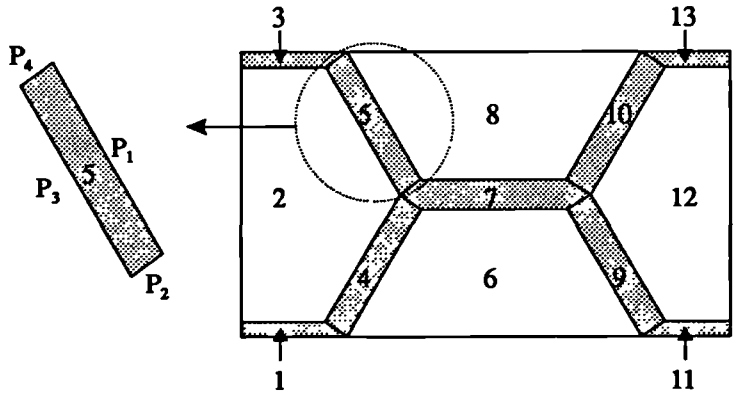

Figure 3.5. The unit cell is divided in 13 regions, each region contains a particular medium (air or lead).

To illustrate the implementation of the program, consider a photon travelling from point *A* towards point *C* in the image plane. The intersection of the photon trajectory

with the collimator face is at point *B* (see figure 3.6). The initial photon position and direction cosines determine the point of intersection of the photon trajectory with the collimator face. This point can be used to find the region of the unit cell where the photon will continue travelling.

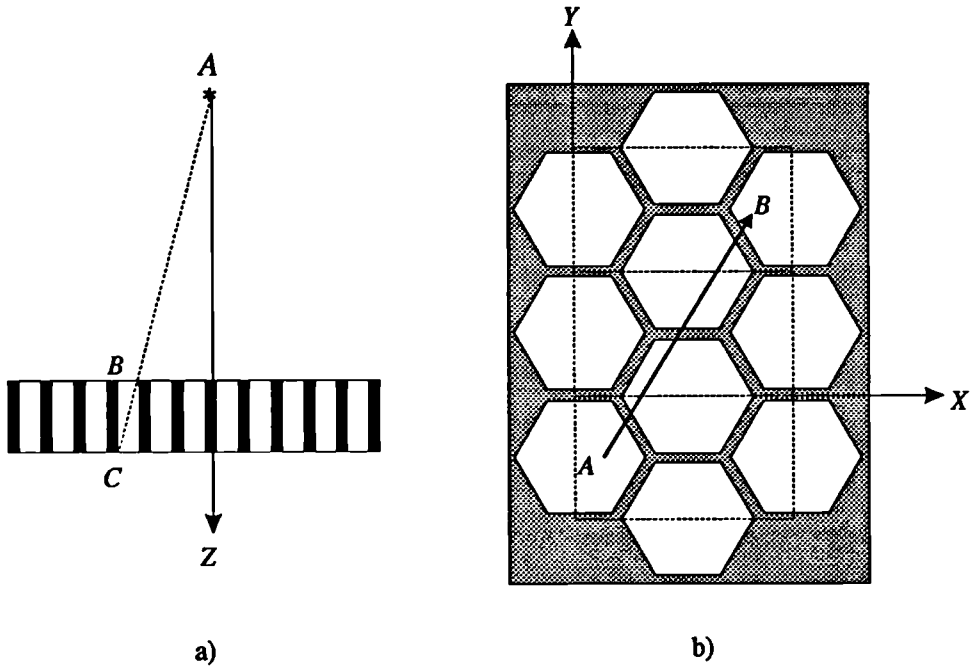

Figure 3.6. Geometry of the system used in the implementation of the collimator program. a) A photon emitted at position *A* intersects the collimator front face at point *B* and the image plane at point *C*. b) Section of the collimator showing the position on the unit cell where the photon intersects the collimator front face.

Once the photon is travelling within a region of the unit cell, the photon direction cosines determine which face of the polyhedron the photon will hit in the absence of attenuating medium. This process is performed in a system of coordinates fixed in the unit cell. The photon position and direction are used to calculate the distance that the photon has to travel to cross to the next region. This distance is compared with the integral photon mean free path calculated for the particular medium where the photon is travelling and the photon energy. If the distance is lower than the integral mean free path then a photon interaction takes place, otherwise the photon is transported to the next region. When the photon reaches the boundary of the unit cell, the photon coordinates are transformed with respect to the fixed Cartesian system defined by the unit cell in order to continue the transport. This procedure is repeated until the photon is absorbed, escapes the collimator geometry or its energy drops below a cut-off energy.

The actual implementation of the program allows the parameters of the hexagonal hole and the collimator material to be altered to simulate a variety of collimators. The default values for the collimator geometry are: 0.03 cm septal thickness, 0.25 cm hole size flat-to-flat and 4.1 cm collimator length. The collimator is assumed to be constructed with a 94%-6% lead-antimony alloy. Three types of photon interactions are included: coherent scattering, incoherent scattering and photoelectric interaction. The cut-off energy is assumed to be 80 keV.

It is feasible to simulate the production and transport of characteristic photons within the collimator. However, some tests indicated that their inclusion resulted in an increase of the CPU time as compared with the same version of the program without this option. It is also important to mention that for many isotopes the presence of characteristic photons does not affect the quality of the images since windowing is applied. For these reasons, the production of characteristic x-rays was not included.

3.3.2. Validation of Monte Carlo Codes

Any Monte Carlo simulation study must include a validation of the program to ensure that the code does not have potential errors and that all the approximations assumed during its development are valid. Several methods have been proposed in nuclear medicine for testing Monte Carlo codes quantitatively. These include comparisons between theoretical prediction of parameters that characterise the system and the simulation results. Experimental validations are also widely used to compare measured and simulated quantities such as energy spectra, scatter fractions, point spread functions or image profiles (Floyd *et al* 1984, Manglos *et al* 1987a, Rosenthal and Henry 1990, Yanch *et al* 1992, Yanch and Dobrzeniecki 1993). In this project both types of validation were used to test the collimator program.

3.4. Validation of the Collimator Program Using Analytical Expressions

This section presents the validation of the Monte Carlo program described in section 3.3.1 by using the collimator spatial resolution according to Anger's formula (equation 3.2) and the geometric response function (equation 3.3). To achieve this, a Monte Carlo simulation was written to calculate the effective point spread function of the LEGP collimator as a function of the source-collimator distance.

The same coordinate system as shown in figure 3.6 was used in the simulation. A ^{99m}Tc (140 keV) point source was assumed to be located above the collimator face. The detector was assumed to have an ideal response, that is, every photon hitting the image plane, located immediately behind the collimator, was recorded. The position of detection was given by the intersection of the photon trajectory with this plane. The collimator was assumed to be fixed in the system of coordinates whereas the point source and the detector were shifted along the X and Y directions to cover a certain area. The X and Y source positions were sampled from uniform distributions within 4 collimator unit cells to include all the possible positions in the collimator hole pattern.

For each source position the photon direction cosines were sampled according to the probabilities that govern an isotropic distribution. The program allowed every individual photon to be traced from its point of origin in the source until it reached the image plane. The detected photons were classified according to their contributions to the components of the point spread function, that is, if a detected photon travelled completely through air, it contributed to the geometric component. Conversely, if a detected photon had passed through a septa without suffering any interaction, its contribution was assigned to the penetration component, otherwise to the scatter component.

3.4.1. Spatial Resolution

Results of calculations using equation 3.2 were compared with those from the Monte Carlo simulation. Spatial resolution according to Anger's formulation considered square collimator holes. Therefore, the collimator hole size in equation 3.2 cannot be substituted directly by the hexagonal hole size flat-to-flat, DF, due to the fact that D represents an average of the possible paths a photon can travel through a collimator hole. It can be shown (Harrison 1993) that the effective hole size for a hexagonal hole is $D \equiv (\sqrt{3}/2)DF$. A plot of the Anger's collimator resolution as a function of source to collimator distance is shown in figure 3.7. Results for the geometric component FWHM obtained with Monte Carlo simulation are also plotted. The chi-square, χ^2, criterion was applied to compare both sets of data obtaining $\chi^2 = 5.28 \times 10^{-3}$. This value indicates that there is a very good agreement between the theoretical prediction and the Monte Carlo simulation.

The Monte Carlo data presented in figure 3.7 were fitted with a straight line of the form $y = mx + b$ where m is the slope and b is the intercept. According to the parameters used in Anger's equation, $m = (D/L) = 0.0528$ and $b = D = 0.217$ considering an effective hole size $D = (\sqrt{3}/2)DF = (\sqrt{3}/2) \times 0.25$ cm, a collimator length $L = 4.1$ cm and a collimator-detector distance $B = 0.0$ cm. The linear regression of the Monte Carlo data produced a slope of $m = 0.0522 \pm 0.0002$ and an intercept of $b = 0.211 \pm 0.006$. These values are in agreement with those predicted with Anger's equation.

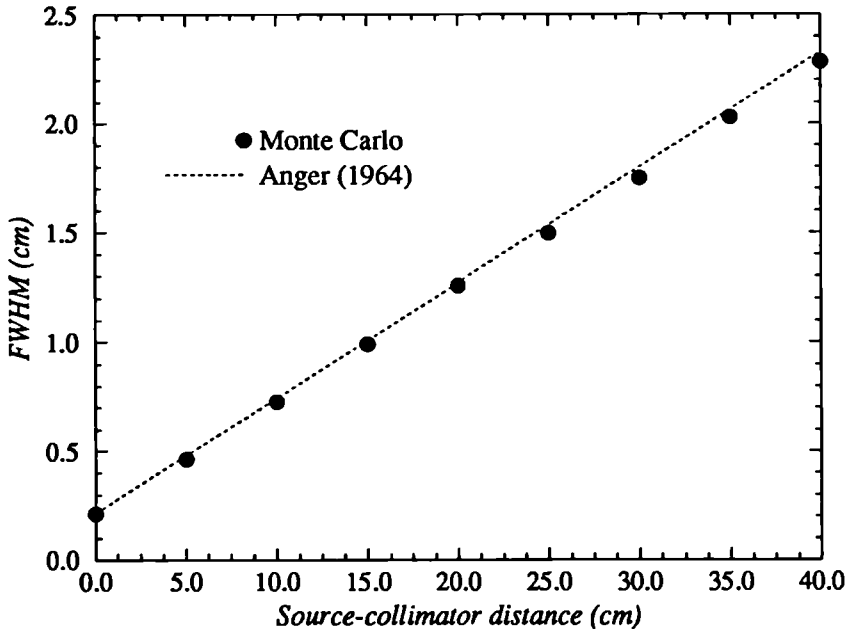

Figure 3.7. Collimator resolution as a function of source height obtained from the Monte Carlo simulation and Anger's equation. Estimated errors are of the order of the symbol size.

3.4.2. Geometric Response Function

The geometric component of the effective point spread function was determined for a set of source heights measured from the front face of the collimator. The normalised geometric components of the effective point spread function are shown in figure 3.8 for both, the results from the Monte Carlo simulation and the geometric response function. The number of photons originating from the source (within the Monte Carlo program) had to be increased with increasing source height to maintain the same number of detected photons per unit area in the image plane. It can be observed from the graph that there is an excellent agreement between the two sets of data.

A quantitative comparison between the sets of data was carried out using the χ^2 criterion. In all cases the χ^2 values were lower than 3×10^{-3}, confirming our observation that there is a very good agreement between the two calculations.

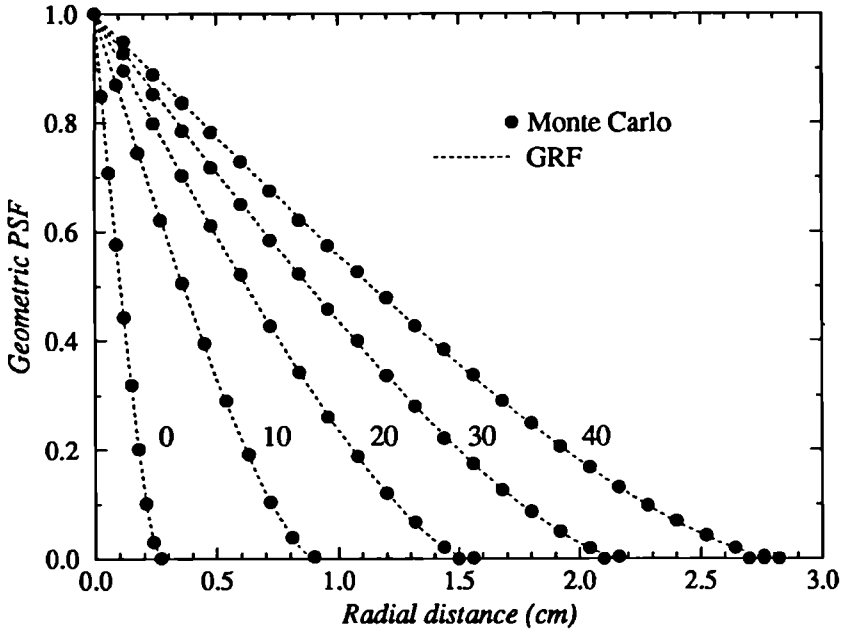

Figure 3.8. Comparison between the geometric response function (equation 3.3) and the geometric component of the collimator PSF calculated with the Monte Carlo program at several source heights. The curves are normalised to one at the origin. Calculated errors are of the order of the symbol size.

3.4.3. Geometric, Penetration and Scatter Components

Figure 3.9 shows the point spread function components obtained with the Monte Carlo simulation for a source-collimator distance of 40 cm. They are plotted in a semi-logarithmic graph in order to better visualise the small contributions of the scatter and penetration components. It can be observed that the geometric component determines almost entirely the shape of the point spread function. However, the tail of the PSF is modulated by the penetration and scatter components. The geometric, penetration and scatter components comprised approximately 97.5%, 1.9% and 0.6% of the total number of photons, respectively. These values were typical for all source-collimator distances used in the simulation. These results show that the dominant contribution to the PSF for 140 keV photons originates mainly from the geometric component and that the penetration and scatter components are negligible.

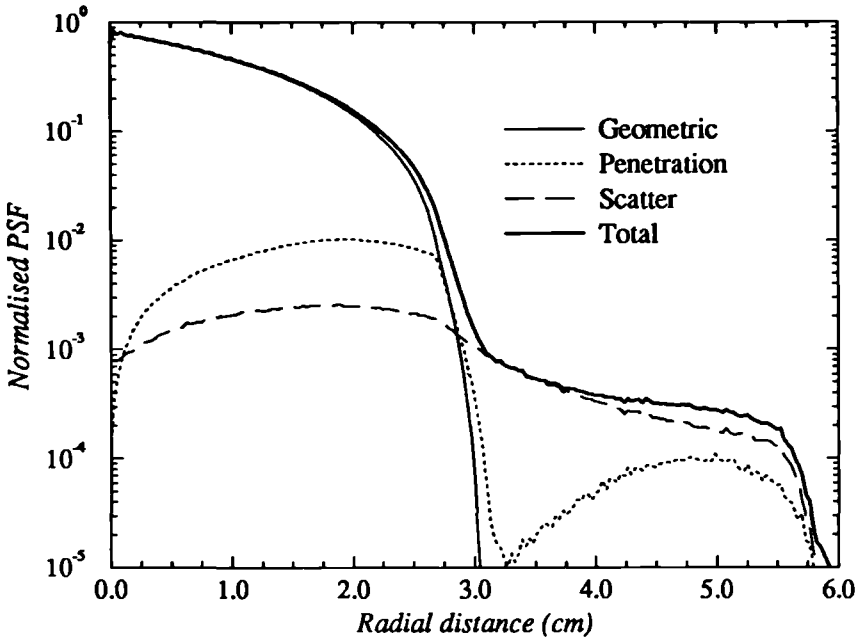

Figure 3.9. Calculated point spread function components for a ^{99m}Tc source placed at 40 cm from the collimator front plane.

3.5. Experimental Validation of the Monte Carlo Program

The theoretical validations of the collimator simulation presented in the preceding sections only considered the geometric characteristics of the imaging system composed of source and collimator without the inclusion of the detector response or the presence of a scattering medium. It has been pointed out in Chapter 2 that the formation of an image with the gamma camera is affected by the detector intrinsic response. Furthermore, the presence of scattering material between the source and the detector degrades the image producing a reduction in contrast, resolution and quantification. It was therefore important to develop a program which included not only a source distribution within a scattering material but also the intrinsic resolution of the gamma camera. The comparison of the Monte Carlo simulation and experimental data provided an accurate evaluation of the program to simulate a more realistic environment.

3.5.1. The Phantom

The structure and dimensions of the phantom were based on a CT image of a human thorax. The phantom was composed of three blocks of solid perspex of dimensions

40.96x26.88 cm^2. Two plates, each one of 0.5 cm thickness, formed the upper and lower part of the phantom, with a third plate of 1.0 cm thickness located in the centre. Six parallel cylinders were drilled in the central plate, resembling a transverse cross section of a human thorax. These cylinders were filled with a solution of water and ^{99m}Tc. Figure 3.10 shows a schematic diagram of the phantom and table 3.1 shows the dimensions and positions of the cylinders.

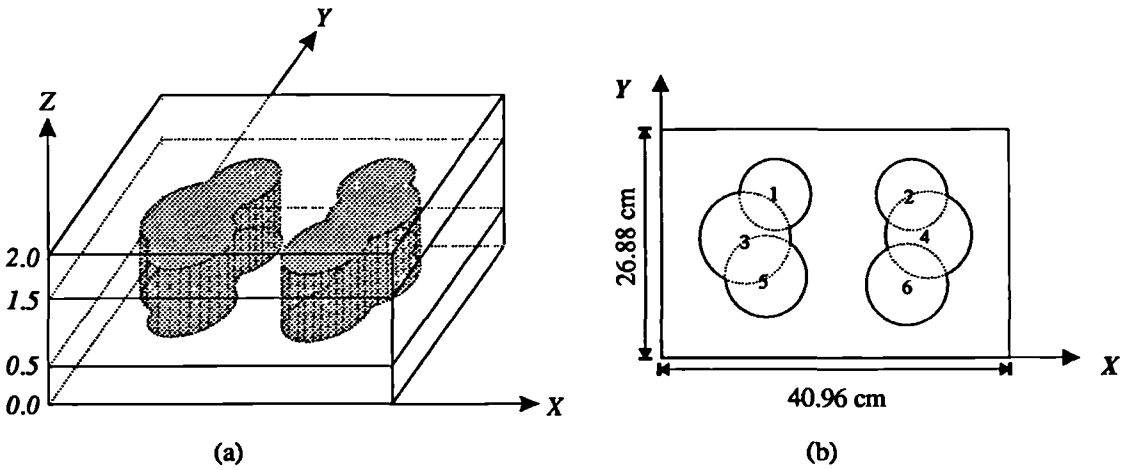

Figure 3.10. Diagram of the phantom used in the experimental validation of the Monte Carlo simulation: a) three-dimensional view of the phantom, b) transverse cross section of the central block.

Table 3.1. Parameters of the cylinders drilled in the phantom.

Cylinder number	*Centre*		Radius (cm)
	X (cm)	*Y* (cm)	
1	13.4	19.2	4.2
2	29.4	19.2	4.2
3	9.9	14.1	5.4
4	31.4	14.5	5.1
5	12.2	9.6	4.8
6	28.8	8.6	4.8

3.5.2. Experimental Arrangement

Figure 3.11 shows the experimental apparatus used during all the measurements. The phantom was aligned with respect to the *X* electronic axis of the gamma camera in the following manner. Two point sources were placed at the centres of the phantom cylinders 1 and 2 (see figure 3.10). The phantom was positioned such that the two sources lay parallel to the *X* axis of the gamma camera. Alignment was accomplished

by performing short image acquisitions, repositioning the phantom every time, until the centroids of the point source images were in the same horizontal profile. After this, a solution of 500 ml of water and ^{99m}Tc (302 MBq) was prepared and the cylinders of the phantom were filled with this solution. A 10 cm thick water bath was placed between the phantom and the collimator to act as a scattering medium.

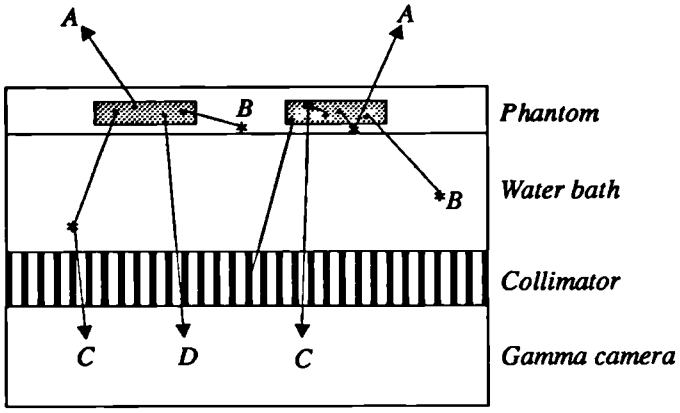

Figure 3.11. Geometry of the system used in both the experiment and Monte Carlo simulation. Photon histories are shown in the diagram representing: *A* escape from the system, *B* absorption, *C* detection of scattered events, *D* detection of primary events.

Two types of measurements were performed with this experimental arrangement. Initially, the gamma camera was set to work in a pulse height analysis mode to measure the energy distribution of the photons hitting the detector. An energy correction matrix measured for ^{99m}Tc was used during this acquisition. The second measurement consisted of the acquisition of several images with different energy windows. Five symmetric windows (10%, 20%, 30%, 50% and 80%) were used, one for each image acquisition. All the images were stored in a 256x256 format. The acquisition time was varied so as to obtain 50×10^6 counts in all the images except the one with 50% energy window where 29×10^6 counts were recorded.

3.5.3. Description of the Program

A uniform activity distribution of ^{99m}Tc mixed with water was assumed to fill the cylinders of the phantom. The *XY* positions of photon emission were sampled from uniform distributions using the rejection sampling method. In this technique, a point is chosen within a rectangle in the *XY* plane that contains the area under interest, in this case the 6 cylinders located in the central block of the phantom. If the point lies within any of the cylinders the point is accepted, otherwise it is rejected. On the other hand,

the Z photon coordinate was sampled from a uniform distribution using the direct sampling method. The photon direction cosines were sampled from the probability distributions that govern an isotropic decay.

The program performed the photon transport within the phantom, water bath and collimator. Once a photon reached the image plane (assumed to be immediately below the collimator) the procedure to account for the intrinsic response of the gamma camera was used. The detected signal was sampled from a Gaussian function with a mean value hv, the energy of the photon just prior to detection, and a standard deviation as a function of hv. The intrinsic spatial resolution of the camera was applied using a digital convolver with a PSF of 3.5 mm.

All the photon histories were traced and classified depending on the number and type of interactions the photons had undergone during their transport. A photon history was discarded when the photons escaped the geometry of the system, the photon energy fell below a cut off energy (set as 80 keV) or when the photon was absorbed in any of the components of the system (phantom, water bath or collimator). A photon energy distribution was obtained for all the detected photons as a function of number of interactions. Following this process, images were produced by binning the detected photon position along the X and Y axes into 256 pixels. The physical pixel size corresponded to 0.16 cm. Five images were thus formed representing 10%, 20%, 30%, 50% and 80% spectral windows centred at 140 keV. The Monte Carlo program ran mainly on IPX Sun workstations. A total of 3.48×10^{10} photon histories were traced in approximately 27 weeks of computing time.

3.5.4. Results

3.5.4.1. Scatter Fractions

The total energy distribution obtained from the Monte Carlo simulation is shown in figure 3.12a. The spectrum is separated in terms of the primary and scattered components. A semi-logarithmic plot of the several contributions to the distribution is also shown in figure 3.12b where the spectrum is separated in different components according to the number of Compton interactions that the photons underwent within the phantom and water bath.

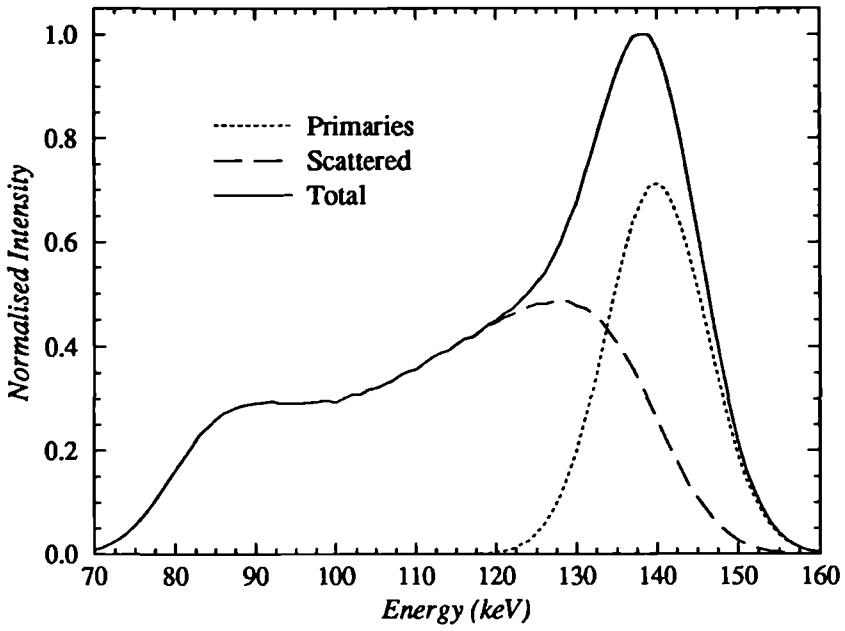

Figure 3.12a. Calculated energy spectra showing the contribution of the primary and scattered photons to the total spectrum.

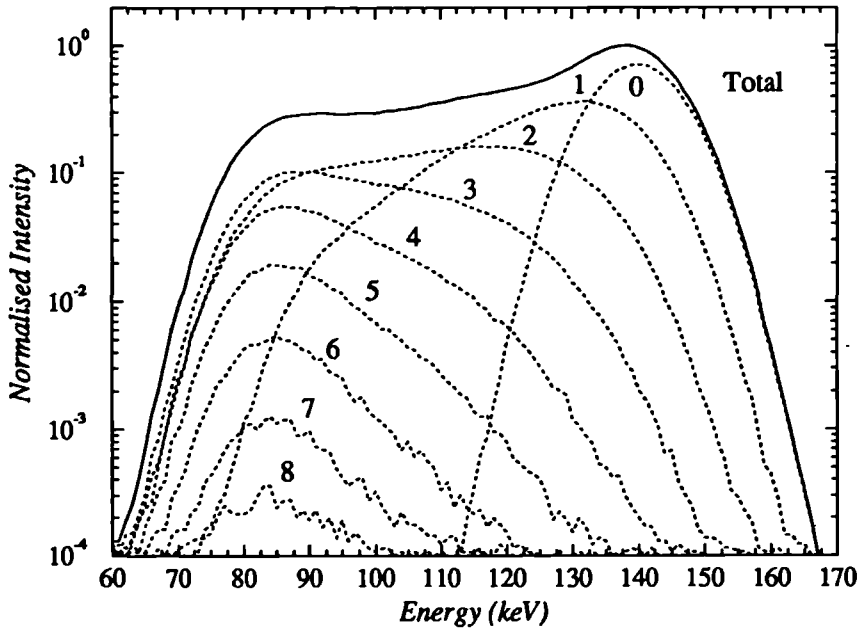

Figure 3.12b. Semi-logarithmic plot of the calculated energy spectra showing the contribution of the different orders of Compton scattered photons.

It can be observed from these plots that the maxima of the spectra are shifted towards lower energies as the number of Compton interactions increases. The results also indicate that a large fraction of scattered photons is detected irrespectively of the energy window used. For 10% or 20% spectral windows (normally used in nuclear medicine departments) the main scatter contribution arises from first and second order Compton scattered photons. The scatter fractions, defined as the ratio of scattered counts to non scattered counts, are shown in table 3.2. The first three orders of Compton scatter are listed separately to show their individual contribution to the scatter fraction.

Table 3.2. Calculated scatter fractions as a function of order of Compton interaction for different energy windows.

Order of Compton interaction	*Scatter fraction*				
	10%	20%	30%	50%	80%
1	0.3787	0.5295	0.6915	0.8792	0.9469
2	0.0566	0.1137	0.2049	0.3956	0.6028
3	0.0051	0.0142	0.0352	0.1107	0.2822
Rest	0.0004	0.0015	0.0044	0.0251	0.1301
Total	0.4408	0.6559	0.9360	1.4106	1.9620

As expected, the scatter fraction increases as the spectral window increases and the contribution of high order Compton scattered photons is more evident. The contribution of first order Compton scattered photons dominates the scatter fraction for any spectral window used. For a 10% energy window, 85.9% of the scattered photons suffered one Compton interaction whereas for a 80% energy window this value dropped to 48.3%.

3.5.4.2. Energy Distribution

The plots of experimental and calculated energy spectra are shown in figure 3.13. Several features can be observed in the graph. The peaks appearing in the experimental data at 74.2 keV and 85.4 keV arise from the characteristic photons produced in the collimator septa. These peaks are not present in the calculated data because no production of the characteristic photons was considered into the collimator program. Besides, the photon cut-off energy was chosen in the program as 80 keV. Therefore, for energies below 90 keV the spectra cannot really be compared. Above this energy, the sets of data show very good agreement.

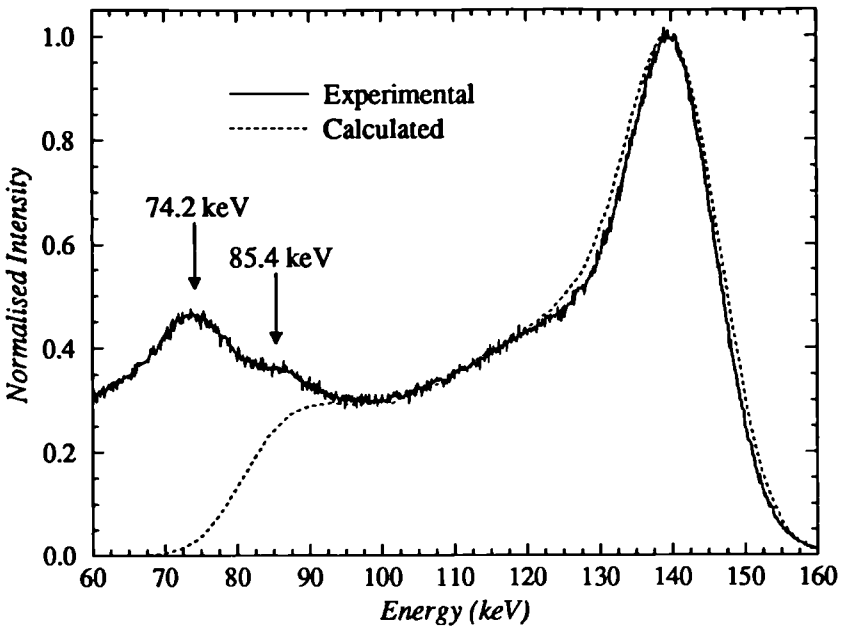

Figure 3.13. Comparison between calculated and experimental energy spectra.

3.5.4.3. Image Comparison

Some examples of the images obtained with the Monte Carlo simulation and experiment are presented in figures 3.14 and 3.15. Table 3.3 lists the statistical properties of the experimental and calculated images. It can be observed that the Monte Carlo code presented lower number of counts than the experimental images. These values were limited by the long CPU times required to obtain these results.

Table 3.3. Statistical parameters for the experimental and calculated images.

	Maximum number of counts per pixel		Total number of counts ($x10^6$)	
Energy window (%)	Experiment	Monte Carlo	Experiment	Monte Carlo
10	4067	127	50	1.6
20	3945	178	50	2.3
30	3789	200	50	2.8
50	2104	234	29	3.4
80	3421	275	50	4.2

As discussed in Chapter 1, section 1.7, the comparison between two images requires a registration step to correct for differences in data collection. In this work, image registration was performed through a geometric and a grey map transformation. The geometric registration only considered translation as it was ensured during the

experiment that the orientation of the phantom coincided with orientation of the *X* and *Y* axes of the gamma camera. The normalisation (*NF*) and background (*BG*) parameters were determined for each step in the geometric registration by obtaining the scatter diagram. The scatter diagram is a plot of the pixel intensities of the experimental image *versus* the corresponding values in the calculated image. If a straight line is fitted to this set of data, the normalisation factor is given by the slope of the line and the background by the intercept. The maximum value of the correlation coefficient, *r*, establishes when the images are registered and gives a measure of their similarity.

The procedure to compare the experimental and calculated images can be summarised as follows:

i) Because the extent of the experimental image is limited by its size, a region of interest was selected in both images. A rectangular region of 176x148 pixels was used.

ii) The region of interest on the experimental image was shifted *Dx*, *Dy* pixels ($-m \leq Dx \leq m$, $-m \leq Dy \leq m$, $m \geq 0$).

iii) The scatter diagram was obtained for each shifted position and the parameters *NF*, *BG* and *r* were calculated.

The iterative repetition of steps *i)* through *iii)* allowed the determination of the parameters *Dx*, *Dy*, *NF* and *BG* that maximised *r*. Table 3.4 lists the parameters found during the maximisation of the correlation coefficient for all the energy windows used during the image acquisitions. Results are shown in figures 3.14 and 3.15 for spectral windows of 10% and 80%, respectively. These figures present the experimental images after the registration procedure.

Table 3.4. Parameters that maximise the correlation coefficient *r* during the comparison of experimental and Monte Carlo calculated images.

Energy window (%)	*Dx* (pixels)	*Dy* (pixels)	*NF*	*BG*	*r*
10	-5	-1	0.032	0.990	0.996
20	-5	-1	0.047	-1.689	0.996
30	-5	-1	0.056	-1.817	0.996
50	8	7	0.118	-2.728	0.995
80	8	7	0.084	-3.997	0.995

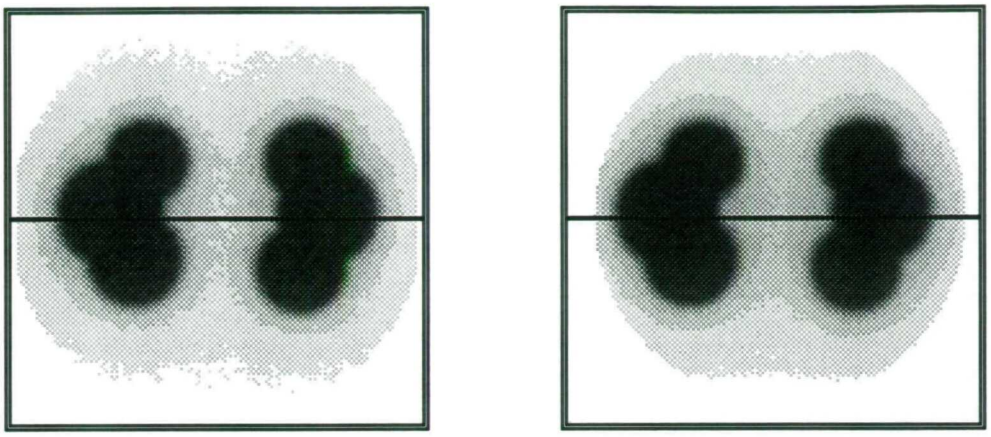

a) b)

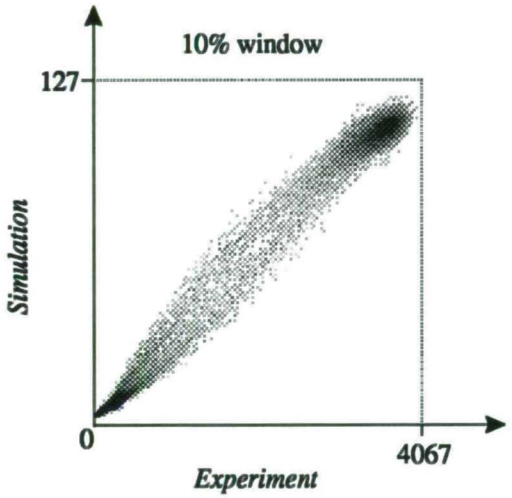

c)

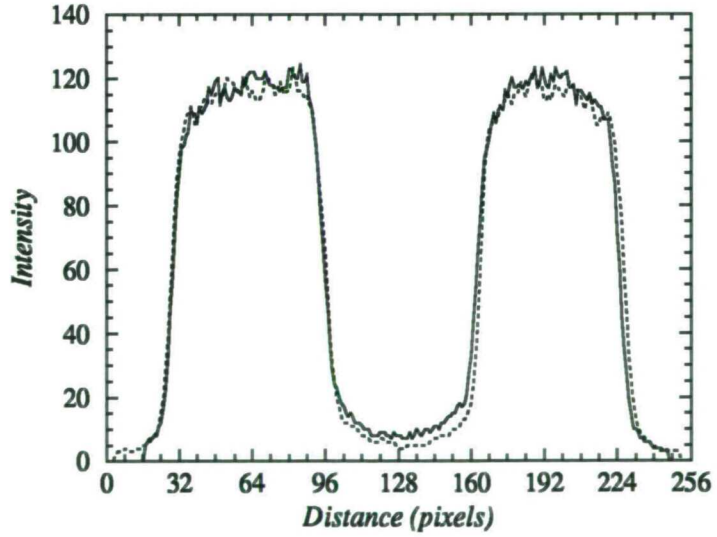

d)

Figure 3.14. Results for a 10% spectral window. a) Monte Carlo simulation, b) experiment after registration, c) scatter diagram. d) horizontal profiles at y=128 pixels as shown in a) and b). ——— experiment, ····· simulation.

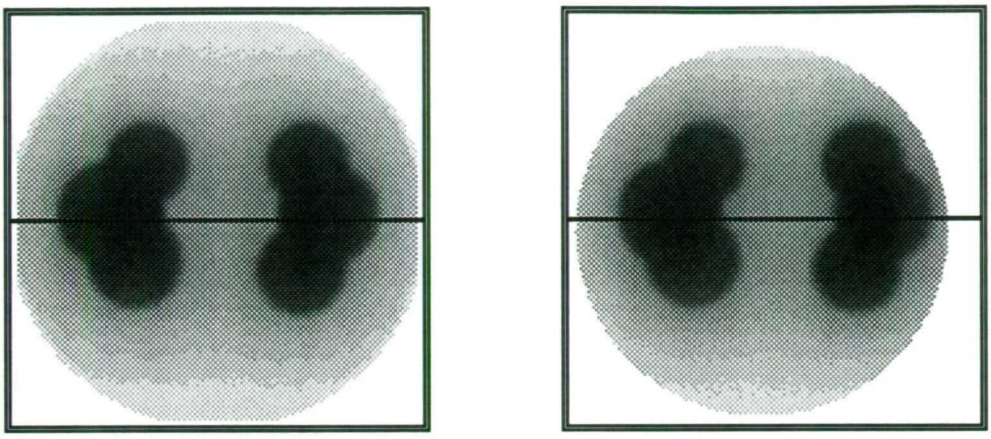

a) b)

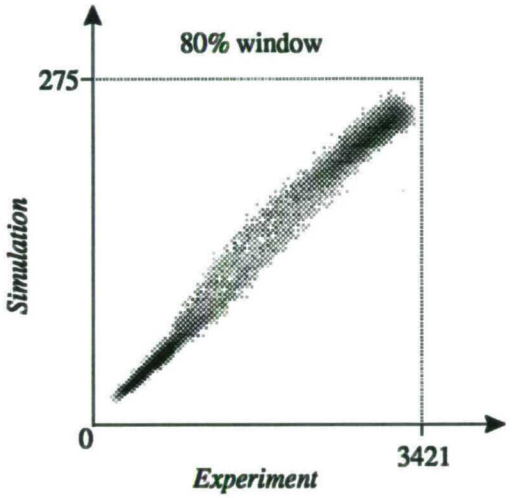

c)

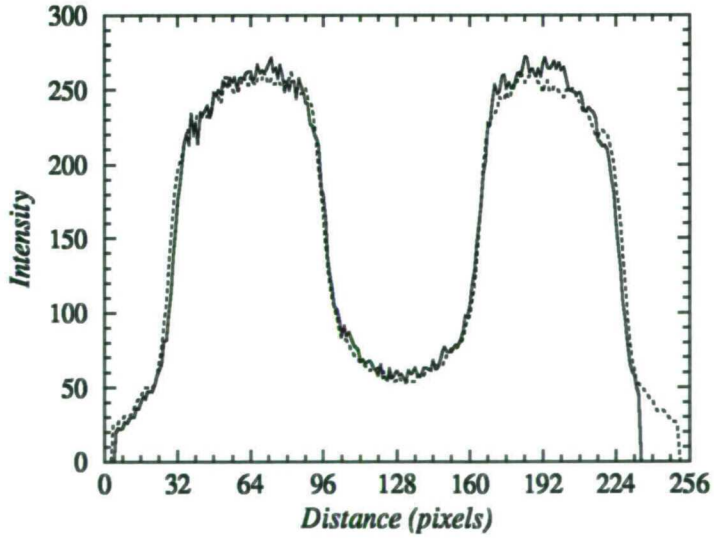

d)

Figure 3.15. Results for a 80% spectral window. a) Monte Carlo simulation, b) experiment after registration, c) scatter diagram and d) horizontal profiles at y=128 pixels as shown in a) and b). ——— experiment, ····· simulation.

It can be observed that in all the cases the values of the correlation coefficients are very close to unity. This fact indicates that the images are very similar to each other. A test was carried out to determine if the correlation coefficient was reliable as a similarity criterion. To this end, the experimental and calculated images were translated from the values Dx and Dy that optimised r given in table 3.4 and the corresponding correlation coefficient calculated. For a displacement of the region of interest of 7 pixels the change in the correlation coefficient was approximately 17% whereas for a displacement of 3 pixels the change was of the order of 5%. According to these values, the correlation coefficient seems to be very sensitive to small image misregistrations.

One of the disadvantages of using the correlation coefficient as a similarity measure is that it ignores the spatial differences between the images. There exist, however, robust methods that account for spatial differences between the images. Among these, the stochastic and deterministic sign change algorithms have proved to be very successful. However, they require the images to have the same statistics: either with statistical fluctuations or with a very good signal to noise ratio. In our comparison, the experimental and calculated images did not present the same statistics: the Monte Carlo images were relatively noisy and the experimental ones had a very high signal to noise ratio. This fact precluded the use of these criteria as measures of image similarity.

To show that spatial correlation existed between the experiment and Monte Carlo results, horizontal profiles were drawn through the images and plotted in the same graph (see figures 3.14d and 3.15d). For an 80% window, a very good agreement can be seen between the profiles. The small differences in the profiles for a 10% window can be explained in terms of experimental errors.

3.6. The GRF as an Alternative Procedure to the Collimator Simulation

The experimental validation of the collimator program indicated an excellent agreement between the experimental data and the simulation. However, the computing time required to obtain these results was extremely long (27 weeks of CPU time). This represents a practical limitation when Monte Carlo techniques are used for more complicated studies. To alleviate this problem, the GRF can be used instead of the collimator simulation to reduce the computing time.

The use of the GRF to account for the presence of the collimator can be justified on the following bases. Firstly, it has been shown in section 3.4.2 that the geometric component of the collimator PSF calculated with the Monte Carlo program is equivalent to the GRF, as can be seen in figure 3.8. Secondly, it was indicated in section 3.4.3 that the geometric component is the dominant contribution to the collimator PSF, and that the scatter and penetration components can be considered negligible. Finally, the photon transport within the patient cannot be replaced by any other technique to characterise the system. These arguments indicate that one approach to reduce computational speed is by using the GRF instead of performing the photon transport through the collimator.

On the basis of these arguments, the GRF was used in place of the collimator simulation to produce all the results presented in the following chapters.

3.7. Conclusions

This chapter described the Monte Carlo simulation of a parallel hole collimator of hexagonal holes. The verification of the program was performed using two approaches. In the first case, the collimator effective point spread function was simulated assuming an ideal detector response. The geometric component of the PSF was compared with both Anger's equation for the collimator resolution and the geometric response function. It was found an excellent agreement between these two comparisons.

The collimator program was modified to include the intrinsic response of the gamma camera and an extended source distribution within a scattering medium. Experimental verification using an equivalent system as in the simulation was performed by comparing energy distributions and images acquired with different energy windows. Both comparisons showed very good agreement. Image comparisons using the correlation coefficient method produced correlation coefficients greater than 0.99 in all the cases. These results indicated that the Monte Carlo program and the approach to include the intrinsic response of the gamma camera produced adequate images. It is then expected that they could be used for more complicated studies.

CHAPTER 4

Transmission Tomography with a Gamma Camera

As discussed in Chapter 1, attenuation compensation algorithms have been developed to correct SPECT images for non-uniform photon attenuation. These algorithms require to determine first the spatial distribution and composition of the attenuating media where the emission source is embedded. Attenuation maps can be measured with a rotating gamma camera fitted with an external source, using standard CT techniques. Several geometries for the external source have been proposed which provide attenuation coefficients for narrow or broad beam geometry. This chapter presents results of a Monte Carlo simulation of a transmission tomographic SPECT system. In order to evaluate the most satisfactory approach to the production of attenuation maps two systems were modelled considering both types of geometry.

4.1. Attenuation Coefficients in SPECT

It has been pointed out in Chapter 1 that SPECT images are contaminated with scattered photons due to the finite energy response of the gamma camera. It was also mentioned that spectral windowing is the most common scatter rejection technique used in nuclear medicine departments. This method allows the rejection of a large fraction of scattered photons, the majority of rejected photons having undergone multiple scattering (Floyd *et al* 1984). A good example of the last statement is presented in Chapter 3, section 3.5.4.1, where the photon energy distribution of a simulated phantom was calculated as a function of number of Compton interactions. In this example, the use of a 20% energy window produced a scatter fraction of 0.66, with 80% of the scattered photons arising from single Compton interactions. Similarly, some primary events were discarded because their energies were not within the spectral window causing a loss of detection efficiency. This indicates that the selection of an energy window is a compromise between the rejection of a large fraction of scattered photons while maximising the detection of primary photons. Unless a scatter

correction is applied to the emission data, the image acquisition is considered to be under broad beam geometry. An increase in the number of detected photons produces an apparent increase in the penetration of the primary photons. Under these circumstances, the linear attenuation coefficients associated with scattering media are regarded as effective attenuation coefficients, which characterise by having a lower value than narrow beam attenuation coefficients.

If attenuation correction is to be applied to the emission data it is important to determine what sort of attenuation coefficients should be used. Several attenuation correction methods have been proposed, amongst which we can find those that assume a uniform object with constant linear attenuation coefficient (Budinger and Gullberg 1974, Kay and Keyes 1975, Budinger *et al* 1979, Chang 1978). These investigations raised the question of whether to use narrow or broad beam attenuation coefficients. Harris *et al* (1984) have measured the attenuation coefficient for 140 keV photons in water-filled phantoms using gamma cameras. Their data showed that an effective attenuation coefficient of $\mu_{eff} = 0.12\ cm^{-1}$ improved results when compared with the use of the narrow beam value $\mu = 0.15\ cm^{-1}$. This work suggests that a value of $\mu = 0.11 - 0.12\ cm^{-1}$ is appropriate for use in attenuation compensation when an average is required. Other researchers (King *et al* 1991) have used the latter value with remarkable success.

On the basis of these studies it could be supposed that the linear attenuation map required for attenuation correction should be measured using a broad beam geometry. This assumption seems to be valid if the emission data contains both primary and scattered photons. However, if the scattered photons can be discarded from the data set by using a scatter correction technique, it could be assumed that the attenuation coefficient map should be measured on a narrow beam geometry basis. Therefore, it is important to study carefully the effects of attenuation correction when using the two types of geometry in the determination of attenuation coefficients. Scatter correction techniques are not within the scope of this project and they will not be used explicitly. However, because of the flexibility of the computer simulations, it is straightforward to classify separately primary and scattered events and label every detected photon according to its history. In this way, it is possible to consider only primary photons during the image reconstruction (this case would correspond to an ideal scatter correction) or primary plus scattered events (no scatter correction applied).

4.2. Monte Carlo Simulation

Thirty-two projections were simulated over a 180° rotational arc following the procedure described in Chapter 1, section 1.6.2. A circular orbit with a radius of rotation of 15 cm was employed. The projections were obtained in a 128x128 format with a corresponding pixel size of 0.32 cm. A range of photon energies for the external source was selected based on the typical energies used in a nuclear medicine department. For both sources the energies selected were 180, 140, 98 and 75 keV. In addition, the collimated line source also included a study with 122 keV photons.

4.2.1. The Transmission Phantom

A mathematical phantom was designed with similar external dimensions to the thorax of a human adult. The phantom consisted of a cylinder of perspex, elliptical in cross section, containing 6 rods filled with different tissue equivalent materials. The selection of the materials was based on the tissues normally found in the thorax and were selected because of their range of densities and compositions. A schematic diagram of the phantom is presented in figure 4.1. The height of the phantom was equal to 41 cm, the FFOV of the IGE XCT gamma camera.

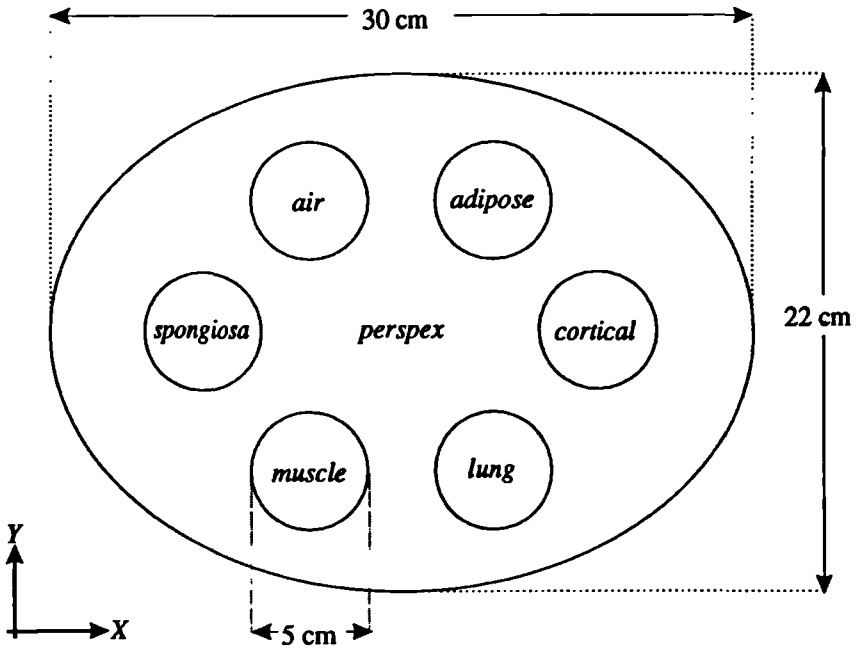

Figure 4.1. Transverse section of the transmission phantom. The selection of the rod materials was based on the range of tissues found in the thorax.

4.2.2. Monte Carlo Procedure

As described in Chapter 1, section 1.6.2, the photon histories were traced and, if the photons reached the collimator face, their parameters were stored on magnetic tape. In this study, at the end of each successful history each photon was associated with a vector given by:

$$\mathbf{r} = (y_i, z_i, \varphi_i, y_f, z_f, E, \varphi, \theta, N_R, N_C) \tag{4.1}$$

where: (y_i, z_i) is the initial photon position in the source plane (at $\alpha = 0°$),

φ_i is the initial photon azimuthal angle,

(y_f, z_f) is the final photon position in the collimator face (at $\alpha = 0°$),

E is the photon energy on arrival at the collimator,

φ is the photon azimuthal direction (angle measured on the collimator face),

θ is the angle between the photon direction and the normal to the collimator face,

N_R and N_C are the number of Rayleigh and Compton interactions inside the phantom, respectively.

A problem was encountered while storing the photon parameters due to the large file size required to store a statistically significant number of counts. A typical run output for a photon energy of 180 keV, projection angle α=0°, with the two geometries used in this study is shown in table 4.1. The last column in the table, referred to as efficiency, is the number of detected photons expressed as a percentage of the number of photons hitting the collimator face. The number of detected photons was obtained from the output of the collimator program.

Table 4.1. Typical output for the two geometries used in the transmission study.

Source	Number of emitted photons ($x10^6$)	Number of photons reaching the collimator face ($x10^6$)	Efficiency (%)
Collimated line	20	2.2	1.19
Flood	90	4.9	0.28

The parameters associated with each photon occupied approximately 16 bytes when stored in a coded format. This value multiplied by the number of photons reaching the collimator face produced file sizes of approximately 34 megabytes for the collimated

line source and of 75 megabytes for the flood source, for each projection and energy. These large files imposed a physical limitation on the number of stored photons. On the other hand, the number of photons reaching the collimator had to be high in order to get reasonable statistics for the detected events. To alleviate this problem, an algorithm was developed to allow a set of probability density functions to be formed that characterised the photons reaching the collimator face. These density functions were then used to generate as many photons as required. This algorithm is described in the next section.

4.2.3. Sampling of Photon Parameters

The photons reaching the collimator face could be completely characterised by the probability density functions that governed their position (y_f, z_f) direction (θ, φ) and energy (E). These probabilities were obtained by using the respective photon intensity, $I(y_f, z_f)$, energy spectrum, $I(e, y_f, z_f)$, and angular distributions, $I(\theta, y_f, z_f)$ and $I(\varphi, y_f, z_f)$, as a function of the photon position (y_f, z_f).

For the ideal case of an infinitely long source and phantom, both symmetrical along the Z direction, the above distributions can be reduced to expressions that depend only on the Y coordinate. In practice, however, it is not possible to use an infinite phantom and source, but the statement can be considered a good approximation if the phantom and source are long. This study was carried out with a long phantom and a long source both symmetrical along the Z axis. Thus, it can be considered a good approximation to characterise the photon distributions only as a function of the Y coordinate. To illustrate this, an example of the phantom images obtained with a collimated line source, a 180 keV photon energy and a projection angle $\alpha = 0°$, is shown in figure 4.2. The 4 images were formed separately with primary and scattered events, before and after the transport through the collimator. Profiles across three different rows in the images are also shown.

It can be observed from figures 4.2a and 4.2b that the images are symmetric along the Z axis and similar spatial photon distributions along the Y direction are obtained for a wide range of horizontal profiles. Taking advantage of this fact, the average photon intensity distribution in the Y direction (which will exhibit less statistical variation) can be constructed by simply adding the photon intensities in the Z direction (that is, along each column).

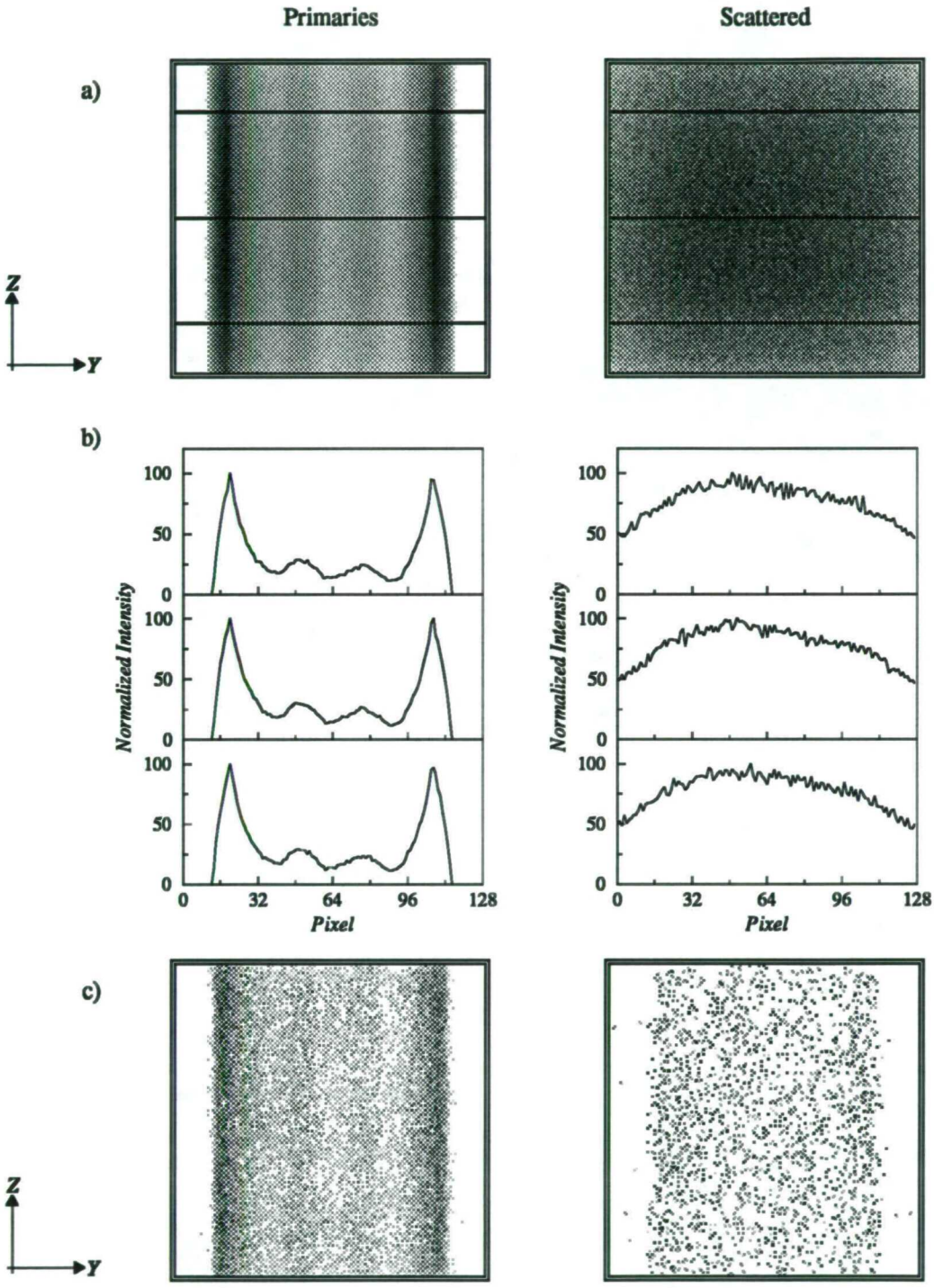

Figure 4.2. Phantom images obtained with a collimated line source, 180 keV photons and projection angle α=0°; a) image of the photons reaching the collimator face, b) profiles across different rows in the images shown in a), c) images of the photon distribution after the transport through the collimator.

Similarly, the photons lying on a particular column are characterised by sharing the same distributions in terms of energy and direction (angles θ and φ), and their respective probability density functions are simply obtained by their classification (with a further normalisation) in terms of these parameters. This is illustrated in figure 4.3.

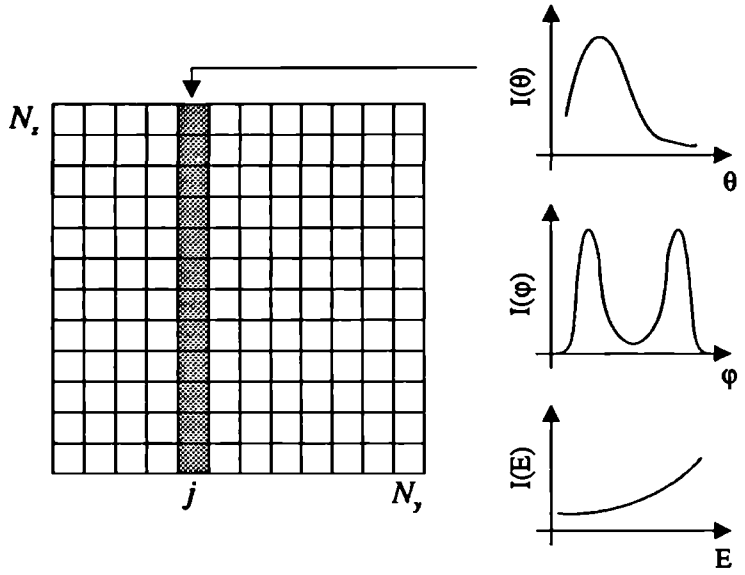

Figure 4.3. The image is represented by a two-dimensional array of intensities $I(j,k)$, $j=1,..,N_y$, $k=1,..,N_z$. For each column, the photon distributions are obtained by summing the photon intensities as a function of any of these parameters: energy, angle θ or angle φ.

The photon distributions obtained were then used to sample photon parameters, as many times as required, to obtain sufficient photon statistics in the detector plane. It was expected that the probabilities that characterised the primary photons would be different from the probabilities for the scattered photons and care was taken in their calculation. The characteristics of the primary photons were still related to the characteristics of the source whereas the scattered photons lost any information about the way they were initially generated. Because of this, the probability density functions for the primary and scattered photons were produced independently of each other.

Once the probability density functions were obtained, the next step was to sample new photon parameters based on these distributions by using the direct method. This method required calculation of the cumulative probability functions, CPF's, associated with the probability density functions and sample from these functions the required parameters. The photon transport through the collimator can be summarised as follows (see also flow diagram in figure 4.4):

1.- CPF's for a particular geometry and incident photon energy were obtained using the raw data stored on magnetic tape (output of the phantom simulation). Primary events were treated independently from scattered events as their distributions depended on their photon histories. The scatter to primary ratio was stored in order to keep the same ratio when the photon parameters were generated.
2.- The CPF's were then used as input data for the collimator simulation. The photon position along the *Z* axis was sampled from a uniform distribution and the rest of the parameters (position along the *Y* direction, energy, azimuthal and polar angles) were sampled from the corresponding CPF's.
3.- Having generated the photon parameters, the transport through the collimator was carried out. This step also included the detection process with the gamma camera.
4.- Tomographic images were finally reconstructed using the ML-EM algorithm.

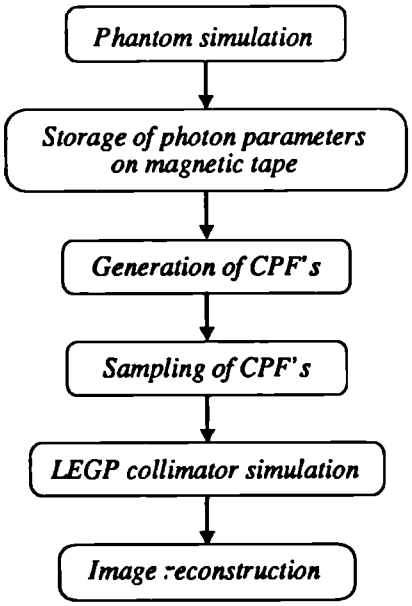

Figure 4.4. Flow diagram showing the steps followed to obtain the phantom attenuation maps.

4.3. Results and Analysis

The two geometries for the external source were simulated according to the procedure described in Chapter 1, section 1.6.2.1. Table 4.2 shows the selection of source geometries, photon energies and activities considered in the study together with the corresponding CPU times used from the production of the raw data (within the phantom program) up to photon detection in the gamma camera. The total number of counts collected over the 32 projections and the percentages of primary and scattered

photons with respect to the total number of counts are also shown. The total number of emitted photons in the source was calculated considering the isotropic photon emission in a 4π geometry. The activity was calculated on the basis of a 30 second acquisition time for each projection.

The collimated line source was run with an aperture of $\Delta\varphi=5°$ for all the studies and all the outputs shown in the table correspond to this value. This aperture was chosen because it allowed investigation of the effect of a high degree of source collimation on the transmission maps. It was only possible to complete the study for one aperture due to time limitations. The CPU times shown in table 4.2 are not directly comparable because the programs were running on different Sun workstations at different stages (including SPARCstation SLC, SPARCstation IPX and SPARCstation 10) but do give an indication on the required computing time.

Table 4.2. Geometries, energies and activities used in the transmission study. The total CPU time for each combination of geometry and photon energy is shown, together with the total number of detected counts added over the 32 projections.

Source	Photon energy (keV)	Activity (MBq)	CPU time (hr)	Detected photons ($x10^6$)	Primary (%)	Scatter (%)
Flood	180	708	650	4.93	69.5	30.5
	140	708	590	3.78	66.8	33.2
	98	786	795	3.29	63.4	36.6
	75	889	617	3.12	61.3	38.7
Line	180	1893	268	9.34	92.7	7.3
	140	1893	272	7.28	92.2	7.8
	122	1893	241	6.56	91.9	8.1
	98	2177	320	6.32	91.2	8.8
	75	2366	362	5.60	90.3	9.7

It can be observed that the flood source study took more than twice the CPU time taken to run the line source study, even though the detected events were considerably smaller. This meant that when the flood source data were generated, the source activity had to be limited. For the flood source, the percentage of scattered photons in the detected image is comparable to the values normally reported for a normal emission study (Floyd *et al* 1984) although the geometries and path lengths do differ. For the collimated line source the scatter fraction is considerably reduced and less than 10% of the detected photons have undergone scattering. This value could be further reduced by decreasing the aperture of the collimated line source. It can also be observed that the fraction of detected scattered photons increases as the photon energy decreases. This effect was also reported by Floyd *et al* (1988). This result may seem

unexpected since the relative probability of incoherent scatter decreases as the photon energy decreases. However, as the photon energy decreases, the probability of photoelectric interaction increases, raising the number of absorbed photons. This loss of primary photons via absorption increases the scatter to primary ratio.

4.3.1. Determination of the Attenuation Coefficients

The phantom attenuation maps obtained with a photon energy of 140 keV are shown in figure 4.5, separated in terms of source geometry and whether only primary or primary plus scattered photons were considered.

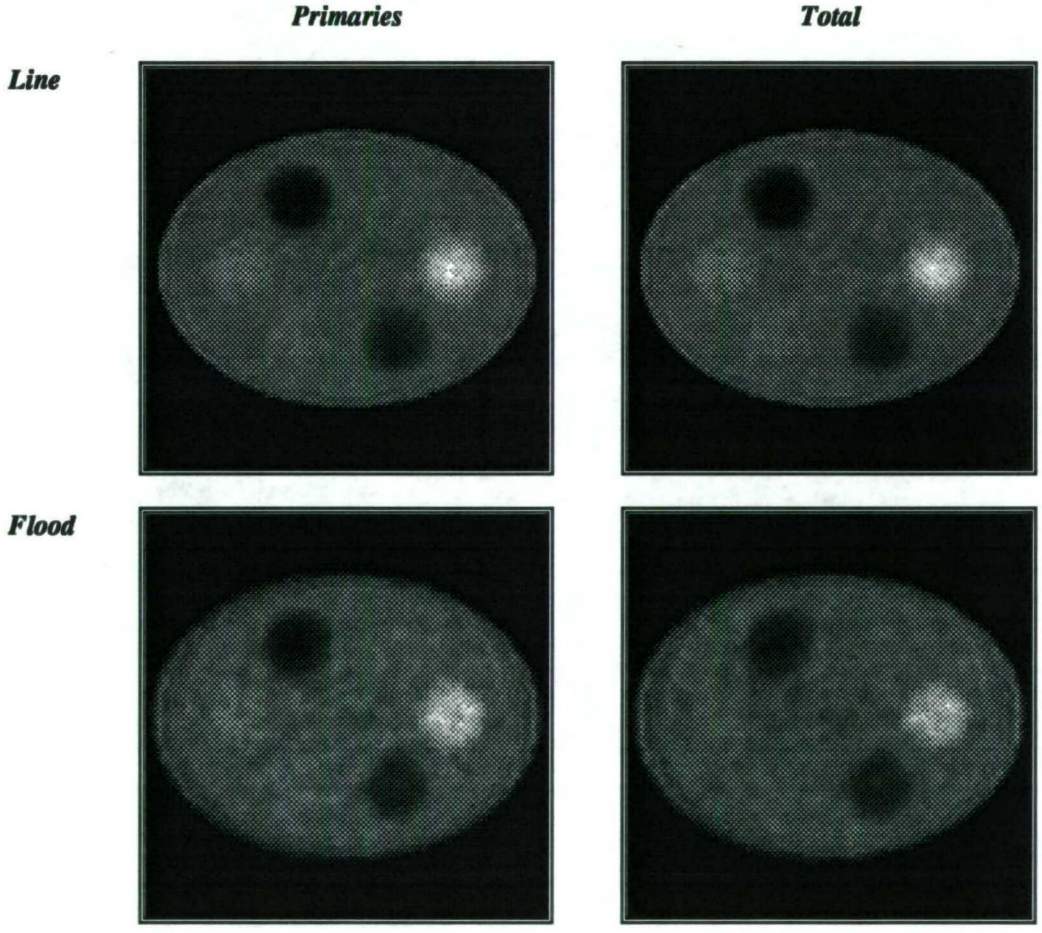

Figure 4.5. Tomographic images of the phantom simulation. Images are presented for 140 keV photons for the two geometries used in the program. The orientation of the images corresponds to the diagram of the phantom shown in figure 4.1.

It can be observed that the collimated line source produced improved image quality with lower statistical fluctuations than the flood source.

The determination of the attenuation coefficients for each material was carried out using an image processing software called *DispImage* (Plummer 1992). The images were displayed and squared regions of interest (ROI) were defined at the centre of each rod. The location of each ROI was selected using the mathematical phantom shown in figure 4.1. Partial volume effects were avoided by selecting the regions of interest enclosed by the rods. The mean value of the attenuation coefficient and the associated standard deviation were calculated for each region. The results are shown in table 4.3 together with the narrow beam attenuation coefficients (NB) calculated from Storm and Israel (1970).

A better way of looking at these results is by plotting the linear attenuation coefficients as a function of energy for each material and geometry. These graphs are shown in figure 4.6. Their main features can be listed as follows:

- The predicted attenuation coefficients are very close to the narrow beam values when calculated for both types of source and considering only primary events (except for the regions containing lung and air).
- The linear attenuation coefficients calculated with the flood source have associated larger uncertainties than the collimated line source images.
- The effective attenuation coefficients show reduced values than narrow beam attenuation coefficients. This reduction varies with photon energy and material type. This result is not unexpected since the intensity and spatial distribution of scattered photons vary with the photon energy, composition and structure of the attenuating media.
- The predicted attenuation coefficients for air are never zero, independently of the source geometry or energy.

Table 4.3. Linear attenuation coefficients obtained from the Monte Carlo simulation.

Material	Energy (keV)	μ_{NB}[a] (cm^{-1})	*Collimated Line Source*				*Flood Source*			
			Primaries $\mu \pm \Delta\mu$ (cm^{-1})		Total $\mu \pm \Delta\mu$ (cm^{-1})		Primaries $\mu \pm \Delta\mu$ (cm^{-1})		Total $\mu \pm \Delta\mu$ (cm^{-1})	
Cortical	180	0.264	0.267	0.010	0.252	0.010	0.264	0.016	0.207	0.008
	140	0.297	0.300	0.016	0.279	0.014	0.298	0.015	0.228	0.012
	122	0.319	0.329	0.013	0.307	0.012	—	—	—	—
	98	0.367	0.375	0.018	0.349	0.013	0.378	0.025	0.280	0.012
	75	0.465	0.474	0.019	0.444	0.021	0.479	0.042	0.363	0.022
Spongiosa	180	0.166	0.167	0.006	0.159	0.005	0.161	0.009	0.112	0.007
	140	0.182	0.189	0.010	0.180	0.009	0.179	0.011	0.123	0.006
	122	0.192	0.195	0.012	0.183	0.010	—	—	—	—
	98	0.210	0.210	0.014	0.197	0.011	0.205	0.015	0.136	0.005
	75	0.243	0.249	0.010	0.229	0.009	0.247	0.015	0.151	0.008
Muscle	180	0.148	0.151	0.005	0.145	0.005	0.146	0.010	0.107	0.004
	140	0.161	0.163	0.009	0.155	0.008	0.158	0.010	0.113	0.007
	122	0.168	0.170	0.007	0.161	0.006	—	—	—	—
	98	0.181	0.179	0.008	0.170	0.007	0.173	0.013	0.121	0.006
	75	0.200	0.205	0.010	0.191	0.007	0.190	0.016	0.123	0.009
Adipose	180	0.135	0.137	0.006	0.131	0.005	0.140	0.010	0.105	0.005
	140	0.146	0.147	0.007	0.141	0.006	0.152	0.010	0.114	0.008
	122	0.152	0.150	0.005	0.143	0.004	—	—	—	—
	98	0.163	0.162	0.007	0.155	0.006	0.160	0.013	0.118	0.008
	75	0.177	0.175	0.009	0.167	0.008	0.173	0.010	0.126	0.008
Perspex	180	0.129	0.138	0.010	0.131	0.009	0.128	0.015	0.091	0.010
	140	0.140	0.145	0.010	0.138	0.008	0.136	0.018	0.095	0.011
	122	0.146	0.152	0.010	0.144	0.010	—	—	—	—
	98	0.156	0.165	0.011	0.154	0.010	0.157	0.013	0.103	0.009
	75	0.170	0.177	0.015	0.166	0.012	0.181	0.017	0.117	0.009
Lung	180	0.037	0.046	0.004	0.045	0.004	0.044	0.007	0.035	0.004
	140	0.040	0.051	0.004	0.049	0.004	0.049	0.006	0.040	0.004
	122	0.042	0.051	0.006	0.050	0.006	—	—	—	—
	98	0.045	0.053	0.005	0.053	0.005	0.057	0.004	0.048	0.003
	75	0.049	0.060	0.006	0.060	0.006	0.057	0.008	0.052	0.006
Air	180	0.000	0.021	0.003	0.021	0.003	0.020	0.004	0.024	0.004
	140	0.000	0.020	0.005	0.020	0.004	0.023	0.006	0.028	0.005
	122	0.000	0.022	0.005	0.022	0.004	—	—	—	—
	98	0.000	0.023	0.005	0.024	0.004	0.025	0.006	0.031	0.005
	75	0.000	0.026	0.005	0.027	0.005	0.028	0.008	0.036	0.007

[a] NB refers to narrow beam geometry.

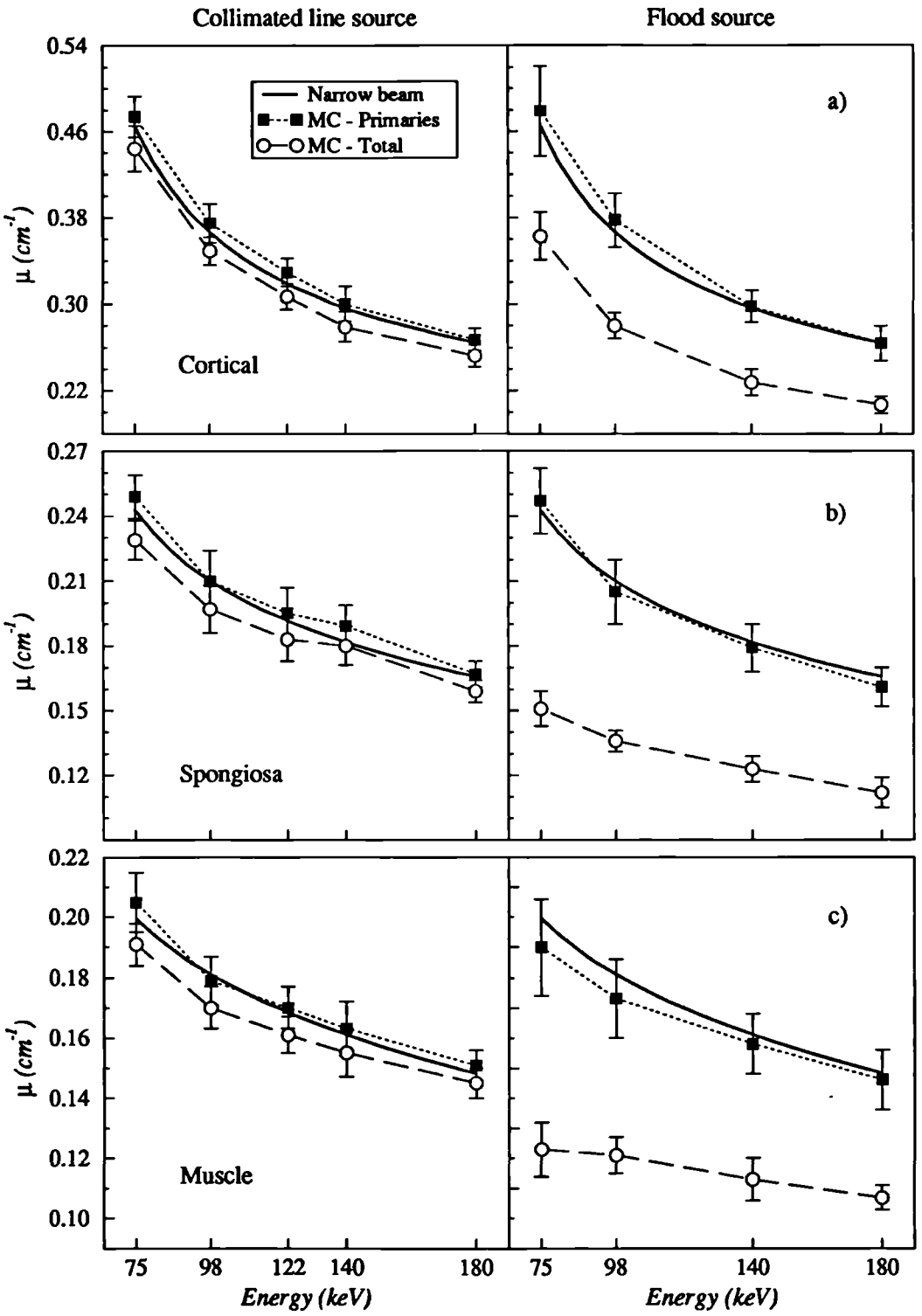

Figure 4.6a-c. Linear attenuation coefficients as a function of energy calculated with the Monte Carlo simulation for the collimated line and flood sources. The data are separated according to the contribution of only primaries or primary plus scattered photons using a 20% window. a) cortical bone, b) spongiosa, c) muscle.

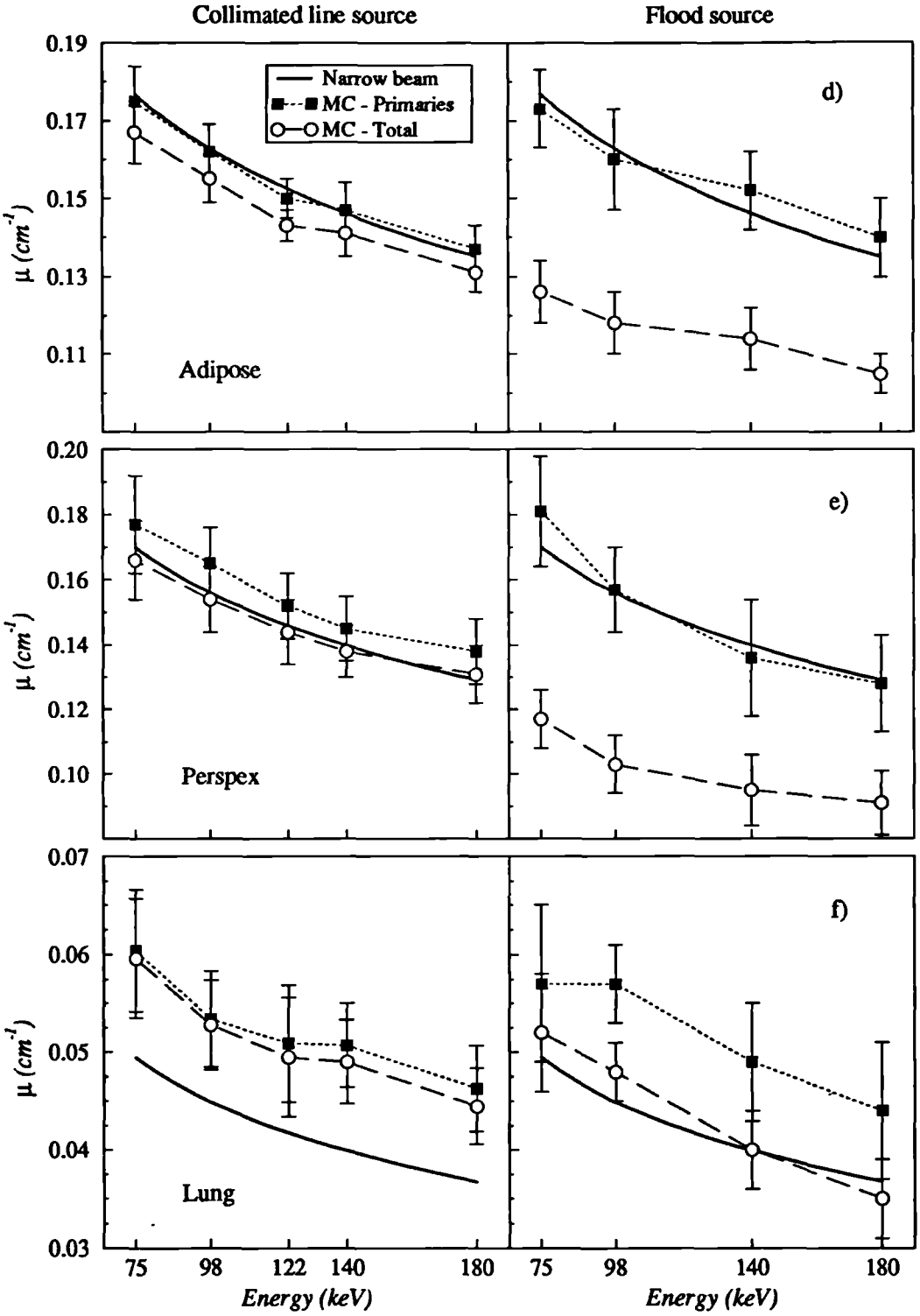

Figure 4.6d-f. Linear attenuation coefficients as a function of energy calculated with the Monte Carlo simulation for the collimated line and flood sources. The data are separated according to the contribution of only primaries or primary plus scattered photons using a 20% window. d) adipose, e) perspex, f) lung.

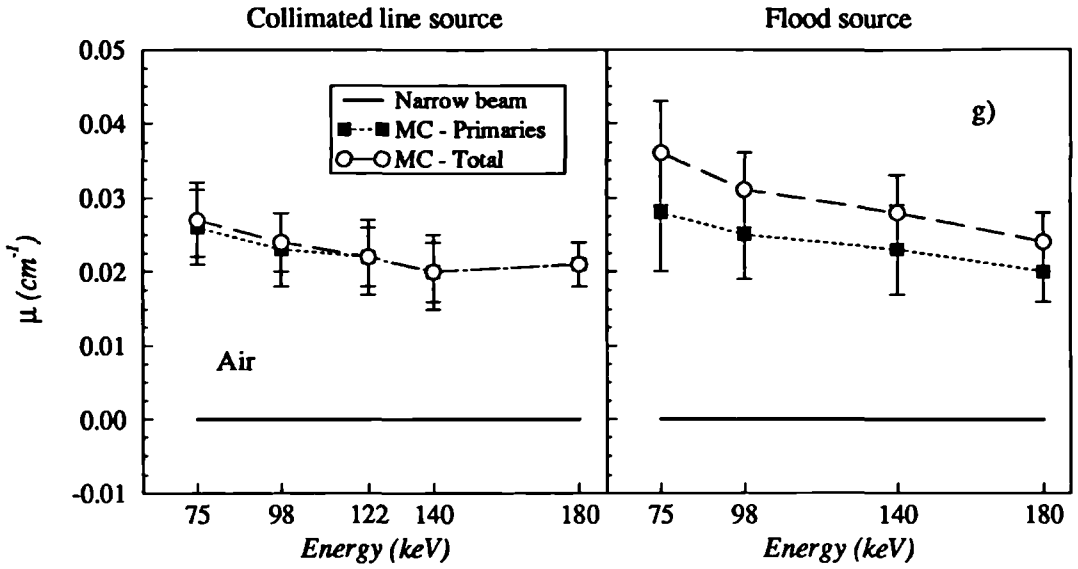

Figure 4.6g. Linear attenuation coefficients as a function of energy calculated with the Monte Carlo simulation for the collimated line and flood sources. The data are separated according to the contribution of only primaries or primary plus scattered photons using a 20% window. g) air.

4.3.2. Energy Dependence of the Linear Attenuation Coefficients

As detailed in Chapter 1, attenuation maps can be measured using the dual radionuclide technique in which the photon energy of the transmission source (E_T) is different from the energy used for the emission study (E_E). The use of this technique requires to scale the attenuation maps in order to be used in the attenuation correction of the emission data. Most researchers simply assume a linear relationship between the attenuation coefficients for both energies E_T and E_E. Bailey and Hutton (1987) have validated this assumption using experimental data. However, the reported attenuation coefficients for tissues were measured with a patient study where partial volume effects could affect the measurements.

The data presented in table 4.3 were used to investigate the relationship between the attenuation coefficients obtained at different energies as a function of several parameters such as geometry of the source and whether the photons originated from primary or primary plus scattered events. To this end, the linear attenuation coefficients obtained from the Monte Carlo simulation for each energy were plotted against the attenuation coefficients obtained with the Monte Carlo simulation for a 140 keV photon energy. These plots are shown in figures 4.7a and 4.7b. Primary events are plotted separately from the primary plus scattered events.

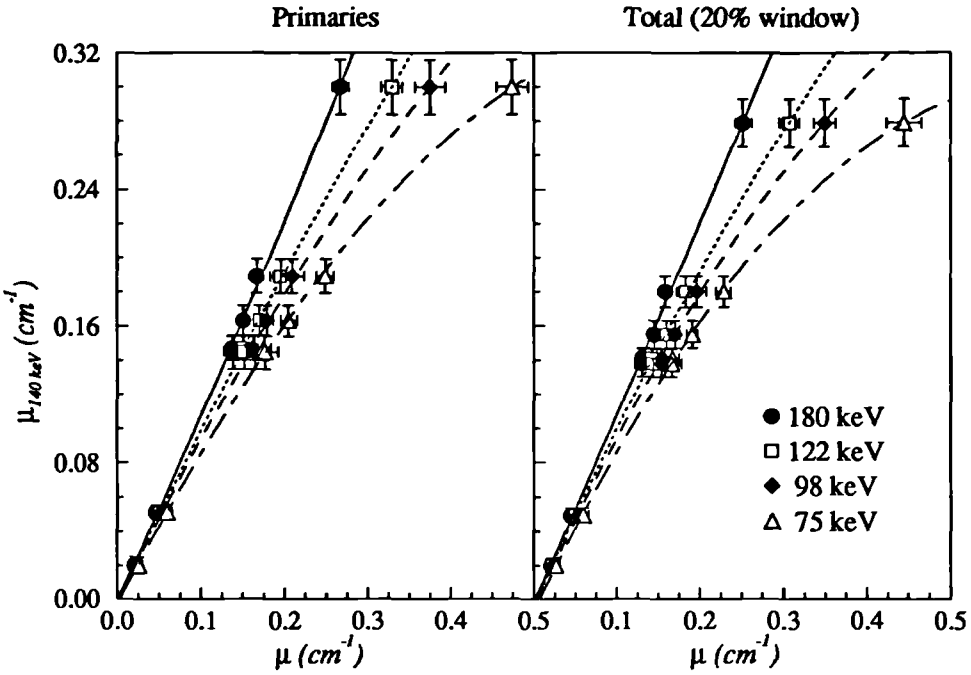

Figure 4.7a. Plot of the linear attenuation coefficients at 140 keV *versus* the linear attenuation coefficients at several energies for the collimated line source study. The symbols represent the Monte Carlo simulation results and the lines the quadratic fits.

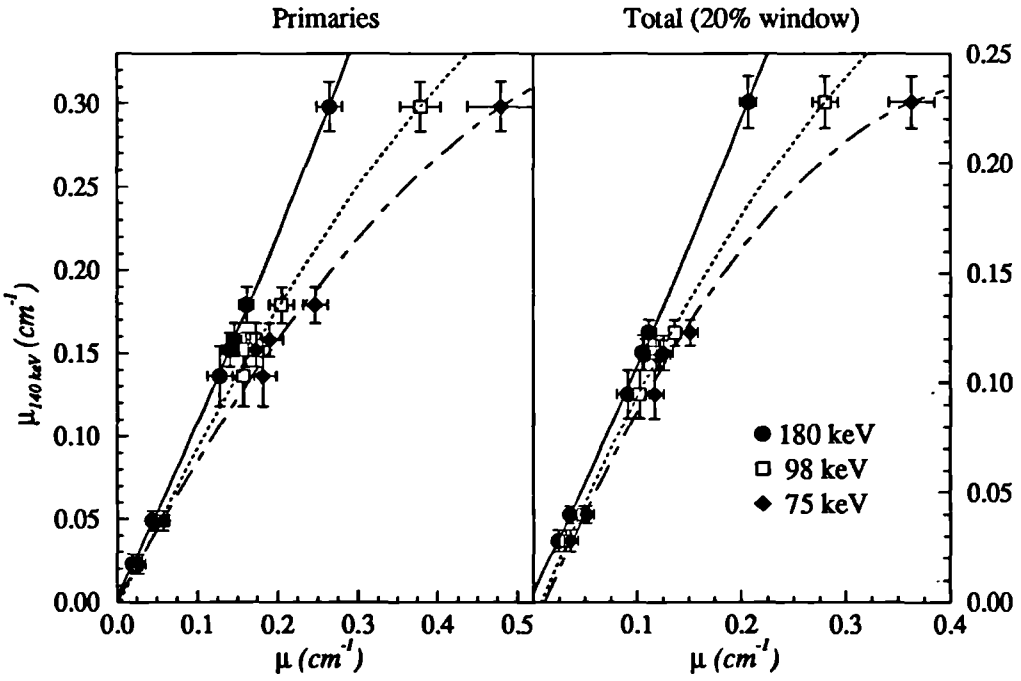

Figure 4.7b. Plot of the linear attenuation coefficients at 140 keV *versus* linear attenuation coefficients at several energies for the flood source study. The symbols represent the Monte Carlo simulation results and the lines the quadratic fits.

It can be observed that there is a non-linear relationship between the attenuation coefficients for the photon energies and external source geometries presented in the graphs. The trend of the curves indicate a quadratic relationship of the form:

$$\mu_{140\ keV} = A_{0,i} + A_{1,i}\mu_i + A_{2,i}\mu_i^2,\ i = 180,\ 122^*,\ 98,\ 75\ keV \qquad (4.2)$$

A quadratic regression algorithm was used to obtain the parameters A_0, A_1 and A_2 for all the data sets of figure 4.7. These parameters are shown in table 4.4. Columns 6 and 10 in the table present the correlation coefficient which indicates the goodness of the fit.

Table 4.4. Parameters obtained from the quadratic fits of the transmission data shown in figures 4.7a and 4.7b.

		Primaries				*Total*			
Study	Energy (keV)	A_0	A_1	A_2	r	A_0	A_1	A_2	r
Line	180	-0.001	1.046	0.309	0.9985	-0.002	1.074	0.170	0.9984
	122	-0.002	1.043	-0.376	0.9997	-0.004	1.077	-0.505	0.9994
	98	-0.003	1.015	-0.551	0.9993	-0.006	1.061	-0.700	0.9994
	75	-0.004	0.951	-0.657	0.9994	-0.007	1.013	-0.829	0.9998
Flood	180	0.003	1.002	0.439	0.9996	0.004	0.980	0.491	0.9992
	98	-0.005	1.031	-0.610	0.9976	-0.008	1.109	-0.954	0.9984
	75	-0.001	0.914	-0.613	0.9924	-0.012	1.115	-1.250	0.9943

In all the cases, the intercept is approximately zero, the first order coefficient is approximately one and the magnitude of the second order coefficient increases but becomes more negative as the energy of the independent variable decreases. The absolute value of the second order coefficient increases as the energy of the independent variable decreases. Therefore, the quadratic term in equation 4.2 becomes more important.

The non-linear relationship between the attenuation coefficients at different energies arises as a consequence of the dependence of the probability of photon interactions with both photon energy and tissue composition. Two main features are observed from the graphs. First, the quadratic trend is more prominent for low photon energies. Second, cortical bone and, to a much lesser extent, spongiosa are the tissues that deviate the curves from straight lines.

* Only for the collimated line source study.

These two characteristics might be explained in terms of the photoelectric effect. At low photon energies, this type of interaction depends on the atomic number of the scattering medium as Z^4 and on the photon energy as E^{-3}. It is then expected that the cortical bone and spongiosa would contribute more markedly to a non-linear relationship because they contain a significant amount of calcium, which is one of the highest atomic number elements in all the tissue compositions. Furthermore, this effect would also be more prominent at lower energies since the E^{-3} dependence is more important.

On the basis of these arguments, it can be concluded that the non-linear relationship found is largely due to the presence of a significant amount of calcium in the tissue composition of cortical bone and spongiosa. To corroborate this, the cortical bone and spongiosa attenuation coefficients were removed from the data sets shown in figure 4.7 and a linear regression algorithm was used to fit the curves. In all the cases, the linear regression produced intercepts between 0.001 ± 0.002 for primary events and between 0.008 ± 0.008 for primary plus scattered events. The slopes of the straight lines and the correlation coefficients obtained are presented in the following table.

Table 4.5. Parameters obtained from the linear regression of the data shown in figure 4.7, excluding the data for cortical bone and spongiosa.

	Collimated Line Source				*Flood Source*			
	Primaries		Total		Primaries		Total	
Energy (keV)	Slope	*r*	Slope	*r*	Slope	*r*	Slope	*r*
180	1.08 ± 0.02	0.9995	1.08 ± 0.02	0.9997	1.07 ± 0.01	0.9998	1.03 ± 0.02	0.9991
122	0.96 ± 0.02	0.9996	0.97 ± 0.02	0.9996	—	—	—	—
98	0.89 ± 0.02	0.9992	0.91 ± 0.01	0.9998	0.92 ± 0.04	0.9970	0.98 ± 0.03	0.9983
75	0.81 ± 0.02	0.9987	0.84 ± 0.02	0.9993	0.81 ± 0.06	0.9916	0.94 ± 0.06	0.9931

It can be observed that all the sets of data can be fitted with straight lines passing through the origin. It is interesting to note that the slopes of the straight lines which contain only primary events can be represented by:

$$\mu_{140\ keV} = \frac{\mu_{140\ keV}(H_2O)}{\mu_i(H_2O)}\mu_i,\ i = 180,\ 122,\ 98,\ 75\ keV \qquad (4.3)$$

where $\mu_{140\ keV}(H_2O)$ and $\mu_i(H_2O)$ are the linear attenuation coefficient for water at 140 keV and the corresponding energy *i*. This linear relationship has been used in the

past to transform the linear attenuation coefficients at different energies (Tsui *et al* 1989).

Equation 4.3 can be used to transform attenuation maps at different energies only if the object under study contains equivalent soft tissue materials. However, this relationship does not hold for objects containing bone tissue and the second order polynomial transformation (presented in equation 4.2) must be used instead.

It is expected that the second order polynomial coefficients presented in table 4.4 (for primary events only) could be used to scale narrow beam attenuation maps. The presence of scattered photons in the attenuation maps precludes the use of a general transformation and the polynomial coefficients must be found for every particular study.

4.4. Conclusions

In order to perform non-uniform attenuation compensation in SPECT imaging it is necessary to obtain the attenuation maps where the source distribution is embedded. This can be accomplished using a rotating gamma camera fitted with an external source and following standard CT techniques. The geometry of the external source can be chosen as to produce narrow or broad beam attenuation coefficients. The use of any of these two types of attenuation coefficient depends on whether the emission data contain scattered photons or not.

This chapter described the Monte Carlo simulation of a transmission study with a rotating gamma camera fitted with a LEGP collimator and an external source. Two geometries and several photon energies for the external source were simulated. A phantom containing different tissues arranged in a simple structure was mathematically designed and included in the transmission study. A mathematical approach was used to obtain reasonable statistics for the detected events. This method allowed a set of probability density functions to be formed characterising the photons reaching the collimator face. The sampling of these probabilities generated as many photons as required. With this respect it is important to note that the calculated activities for the Monte Carlo simulation (4.2) agree with the source activities used in experimental studies for both collimated line and flood sources (Malko *et at* 1986, Bailey *et al* 1988, Tsui *et al* 1989, Gilland *et al* 1993).

The results showed that the collimated line source performed better than the flood source, mainly because the direction of emission was limited. As expected, the flood source produced reduced attenuation coefficients than the reported values for narrow beam geometry and, because the number of detected photons was smaller than the collimated line source study, the reconstructed attenuation maps presented higher statistical fluctuations.

The collimated line source generated attenuation coefficients very close to the calculated narrow beam values. It also produced images with better quality than the flood source. It is expected that the amount of scattered photons reaching the detector can be decreased using a higher degree of collimation.

It was found that the attenuation coefficients at different energies can be related through a second order polynomial transformation, irrespective of the geometry of the source.

CHAPTER 5

Attenuation Compensation Effects

In an ideal case, the intensity values of a SPECT image should be directly proportional to the activity per unit volume (activity concentration) in the object. The use of a conversion factor should then transform the image values to activity concentration. In practice, SPECT images are degraded by several factors that hinder the quantification of physical quantities in the image. This chapter presents the analysis of Monte Carlo simulated data of a tomographic emission study with a rotating gamma camera.

5.1. Quantification in SPECT

The goal of SPECT imaging is to produce the location and intensity of emitting sources within an attenuating medium. Quantification in SPECT refers to the measure of physical quantities related with the source distribution. This measurement can be performed in relative or absolute terms. Relative quantification involves the comparison of different regions in the same image or comparison of one region in two different images acquired under the same conditions. Absolute quantification implies the measurement of areas, volumes and activities in absolute units. Relative or absolute quantification can be achieved by producing images whose pixel values represent the activity concentration in the corresponding region in the patient.

Quantification in SPECT is not an easy task since several degrading factors are involved during the image acquisition process. Among the most important factors are photon attenuation, imaging of scattered photons, detector blurring and poor statistics. The production of a quantitative image requires the use of techniques which can compensate for these factors without creating image distortions or artefacts.

An interesting effect on the quantification of activity concentration occurs when SPECT images are compensated for attenuation and scatter but not for detector blurring. Although the gamma camera resolution is mainly dominated by the collimator resolution, other factors must also be taken into account. Among these factors are

intrinsic resolution of the gamma camera, sampling interval (linear and angular) reconstruction filter and slice thickness. The resolution of the gamma camera has two components: *in-plane* (measured across the reconstructed image) and axial resolution (measured perpendicular to the image plane). The combination of these two components leads to the definition of a volume (the resolution volume) within which measurements of activity or volume cannot be accurately made. The overall effect of the gamma camera resolution is that of producing blurred images of sharp objects.

The measure of activity concentration in a region of interest (ROI) in the reconstructed image requires the knowledge of activity and volume simultaneously, quantities that should be directly proportional to the number of counts in the ROI. Unfortunately, the number of counts within an ROI is dependent on the size of the object relative to the spatial resolution of the imaging system. It has been recognised that the activity concentration of an object can be estimated from the number of counts in the image only if the dimensions of the object are larger than approximately twice the resolution of the imaging system (Hoffman *et al* 1979).

This statement can be illustrated with the use of the superposition principle which states that the image produced by a linear-shift invariant system is given by the convolution of the object intensity distribution with the point spread function of the imaging system (Rossmann 1969). Let us assume, for example, two one-dimensional objects of unit intensity and dimensions of 15 and 2 pixels. Let us also assume that the gamma camera point spread function can be represented with a Gaussian function of FWHM=3 pixels. The convolution of the Gaussian function with the object distributions produce the intensities shown in figure 5.1.

It can be observed that the image of the large object has a large proportion of pixels with the same intensity as the original object intensity and a FWHM equal to the width of the object. Therefore, it is then possible to estimate activity concentration by measuring both the number of counts in the plateau region and the FWHM. A calibration factor must be determined to relate the number of counts per unit volume in the ROI with the sensitivity of the gamma camera (Eichling *et al* 1977).

The image of the small object (whose dimension is smaller than twice the imaging system resolution) has a decreased intensity and its FWHM does not represent the dimension of the object. In this case the total number of counts is preserved but they are distributed over an area larger than the dimensions of the object. Therefore, if the maximum number of counts and the FWHM of the image intensity are taken as a

measure of activity and volume, respectively, there will be an under-estimation of the activity and an over-estimation of the volume. This effect prohibits the measurement of activity and volume simultaneously. Correction factors can be applied to correct for the under-estimation of activity if the volume is known (e.g. by using ultrasound or x-ray CT) (Hoffman *et al* 1979). Conversely, if the activity is known, the volume can be estimated using, for instance, adaptive thresholding techniques (Rowe *et al* 1988). In practice, however, neither the activity nor the dimensions of small objects are known and a true estimation of the activity concentration is impossible to accomplish.

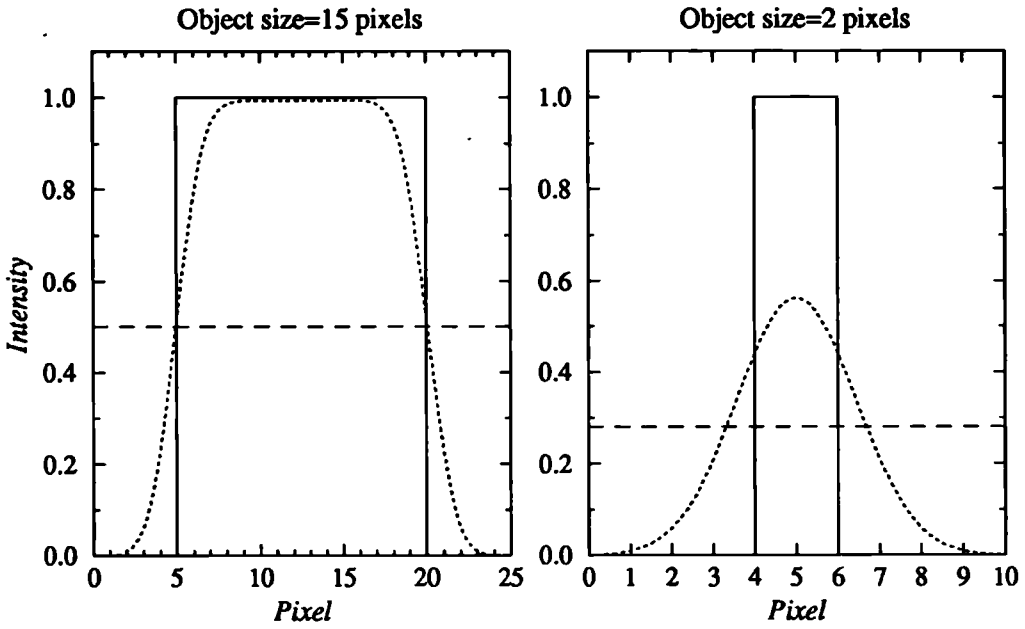

Figure 5.1. Predicted image distributions of one-dimensional objects. The object dimensions were assumed to be larger than or smaller than twice the spatial resolution of an hypothetical imaging system. The point spread function of the imaging system was assumed to be a Gaussian function of FWHM=3 pixels.

In this project relative and absolute quantification of a source distribution was performed using Monte Carlo simulated data and the ML-EM reconstruction algorithm. The structure of the phantom contained non-uniform attenuating media and a cylindrical annular source with activity concentrations varying with angle (see figure 5.2a). The dimensions of the source in the image plane were selected to be smaller than twice the resolution of the imaging system. Such a case is found in myocardial imaging where the maximum myocardial wall thickness can be of the order of the FWHM of the gamma camera resolution (under standard imaging conditions). Non-uniform attenuation compensation was performed using the ML-EM program. The analysis was performed with either only primary or primary plus scattered events. In this way, it was

possible to obtain scatter-free images unaffected by photon attenuation. These images were affected only by the detector blurring.

5.2. Monte Carlo Simulation

Sixty-four projections were simulated over 360°. A circular orbit with a radius of rotation of 15 cm was employed. The projections were obtained in a 128x128 format with a corresponding pixel size of 0.32 cm. Two studies with the same phantom were performed using 75 keV and 140 keV photon energies representing ^{201}Tl and ^{99m}Tc, respectively. A 20% spectral window centred on the photopeak was used in all the simulations.

5.2.1. The Emission Phantom

Cross sectional and lateral views of the phantom with the corresponding dimensions are shown in figure 5.2. This study was based on the same mathematical phantom as the one previously described in Chapter 4 and used in the transmission study. The emitting source consisted of an annular cylinder centred on the phantom with varying angular activity concentrations. Seven relative concentrations (16, 10, 8, 6, 4, 2, 1) were chosen within the annular source at regular angular intervals of 51.4°. The annulus which was parallel to the image plane (*XZ*) had inner and outer radii of 1.5 cm and 3.5 cm, respectively. These values were chosen in such a way that they approximated the maximum myocardial wall thickness (Mettler and Guiberteau 1991). In order to avoid partial volume effects in the direction perpendicular to the image plane, the annular cylinder had a height of 20 cm.

The Monte Carlo program generated the photon positions within the phantom in polar coordinates by calculating a radial distance r_i measured from the centre of the phantom, a polar angle β_i measured anticlockwise with respect to the *Y*-axis and a source height z_i along the *Z* direction. The first two parameters determined completely the position of a photon in the *XY* plane. The selection of the radius required the assumption of a uniform annular source distribution. To illustrate the procedure, let R_1 and R_2 represent the inner and outer radii of the annular source. The area of the annulus is

$$A = \pi\left(R_2^2 - R_1^2\right) \tag{5.1}$$

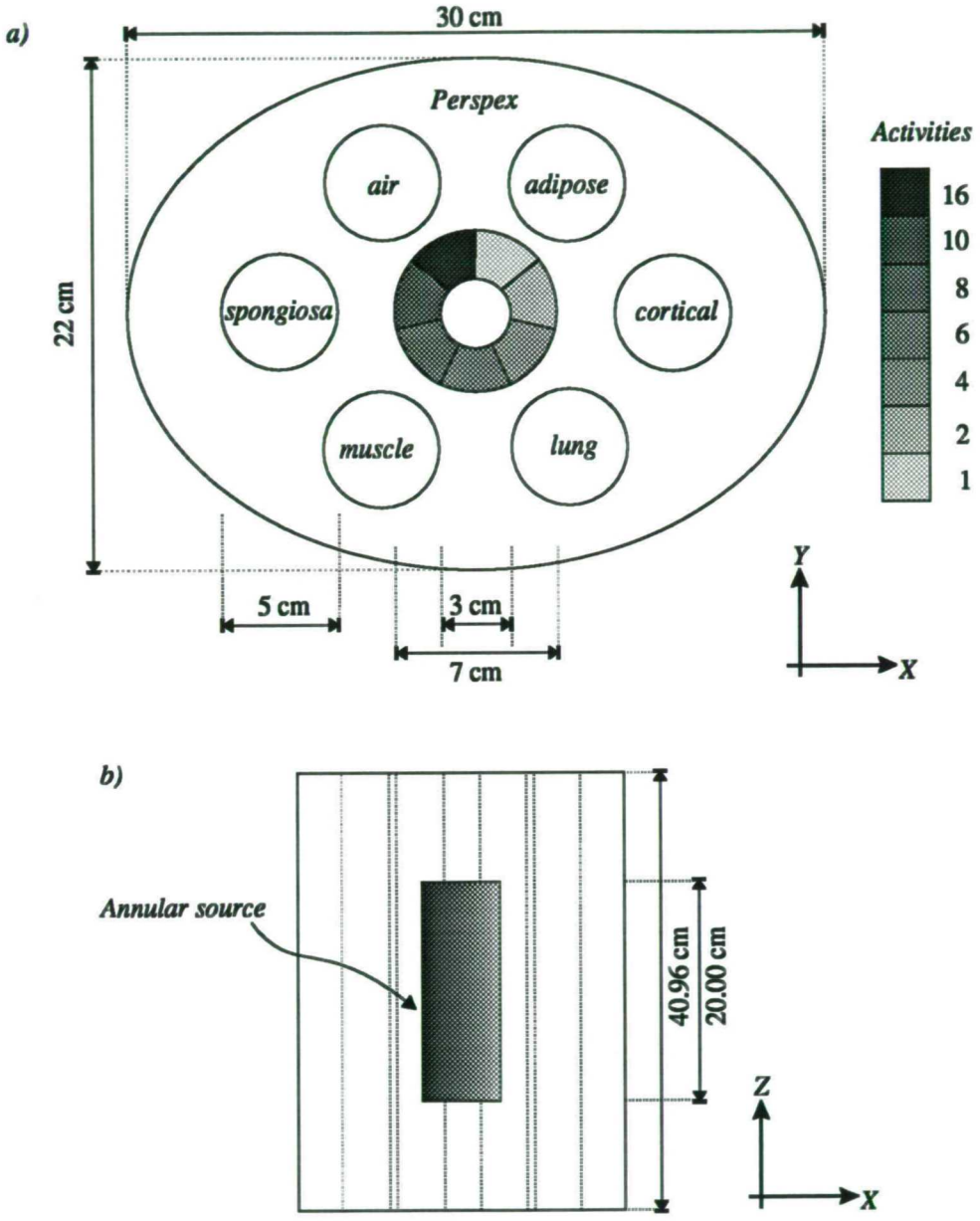

Figure 5.2. Schematic diagram of the emission phantom. a) Phantom cross-section showing seven relative activity concentrations distributed in an annular source. b) Lateral view of the phantom.

In order to generate a uniform distribution within the annulus it is necessary to produce the same number of photons per unit arc length. Since all the positions at radius r_i have the same probability of being generated, the probability density function can be written as follows:

$$p(r_i) = \frac{2\pi r_i}{\pi\left(R_2^2 - R_1^2\right)} = \frac{2r_i}{R_2^2 - R_1^2} \tag{5.2}$$

From this expression, the cumulative probability function is given by:

$$P(r_i \le r') = \int_{R_1}^{r_i} p(r')dr' = \frac{r_i^2 - R_1^2}{R_2^2 - R_1^2}, \quad R_1 \le r_i \le R_2 \tag{5.3}$$

The radius was generated from the last equation by using the inversion method which consists in generating a random number (r^*) between 0 and 1 and inverting equation 5.3. This reduces to calculate:

$$r_i = \sqrt{\left(R_2^2 - R_1^2\right)r^* + R_1^2} \tag{5.4}$$

The polar angle β_i and the source height z_i were sampled from uniform distributions considering $0 \le \beta_i \le 51.4°$ and $0 \le z_i \le 20$ cm.

The sampling of the initial photon parameters r_i, β_i and z_i using the algorithm described above would produce a uniform source distribution in a segment of the annulus. In order to generate segments with different activities in the annulus, a cumulative probability function was produced with the activity concentrations and stored in an array. Then, the inversion method was used to sample the region of the annulus where the photon was going to be generated. The photon direction cosines were sampled according to an isotropic distribution.

Following the procedure described in Chapter 1, section 1.6.3 the photon histories were traced and, if the photons reached the system boundary 1 (figure 1.14), their parameters were stored. At the end of each successful history each photon was associated with a vector given by:

$$\mathbf{r} = \left(IA, r_i, \beta_i, z_i, \beta_f, z_f, \theta, \varphi, E, N_R, N_C\right) \tag{5.5}$$

where: IA is the section of the annulus where the photon was initially generated,

(r_i, β_i, z_i) is the initial photon position in polar coordinates,

(β_f, z_f) is the final photon position in polar coordinates,

(θ, φ) is the final photon direction in spherical coordinates,

E is the final photon energy at the system boundary 1,
N_R and N_C are the number of Rayleigh and Compton interactions the photon underwent inside the phantom, respectively.

5.3. Quantification Methods

5.3.1. Relative Quantification

Relative quantification was performed by comparing the circular profiles of the reconstructed images with a theoretically derived source distribution. The circular profiles were assumed to be centred on the images and were extracted at the maximum radial intensity. The theoretical image was obtained by convolving the source distribution with a calculated point spread function (PSF) of the tomographic system. This PSF was computed from the reconstruction of a point source in air using Monte Carlo simulated data and the ML-EM program. The point source was located in the image plane 2.5 cm from the centre of rotation which corresponds to the average radial distance of the annular source. The geometric parameters of the tomographic acquisition system were kept the same as for the phantom study.

The PSF was calculated for two photon energies (75 keV and 140 keV) and a 20% symmetric energy window. For both energies it was possible to fit the PSFs with a single Gaussian function of 1.2 cm FWHM. Based on this value, the theoretical image was determined by convolving the original source distribution, shown in figure 5.3a, with a spatially invariant Gaussian function with a FWHM of 1.2 cm. The theoretical image, shown in figure 5.3b, represented the noise-free source distribution which only comprised the effect of detector blurring (no scatter or attenuation).

The reconstructed and theoretical circular profiles were compared in terms of the fractional difference (*FD*), expressed as a percentage, of the reconstructed data with respect to the theoretical prediction, which can be expressed as:

$$FD\ (\%) = \frac{(I_R - I_T) \times 100}{I_T} \tag{5.6}$$

where I_R and I_T are the normalised circular profiles at maximum radial intensity obtained from the reconstructed and theoretical source distributions, respectively. An

FD equal to zero indicates no differences between the reconstructed and theoretical profiles, a negative *FD* indicates that the reconstructed data under-estimates the theoretical prediction and a positive *FD* indicates an over-estimation.

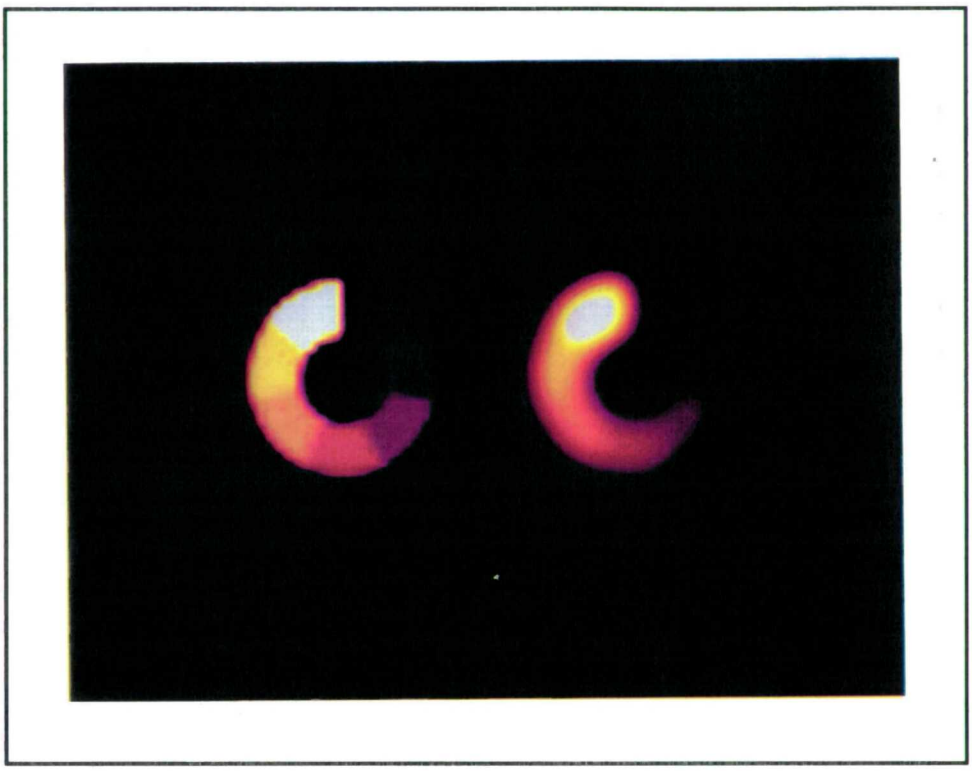

a) b)

Figure 5.3. a) Original source distribution used as input for the Monte Carlo simulation, b) Theoretical source distribution obtained by convolving the original distribution with a spatially invariant Gaussian function (FWHM=1.2 cm).

5.3.2. Absolute Quantification

Absolute quantification was performed with the emission phantom data by measuring the percentage air sensitivity. Sensitivity is defined as the count rate observed per unit source activity. It may be measured with a source within an attenuating medium (a test object) or in air. When measured in air, it represents an ideal quantity which can be used as a basis for comparison with tomographic reconstruction of source distributions. This is particularly important when assessing the performance of attenuation and scatter correction techniques. Percentage air sensitivity is defined as the ratio of the number of counts per unit activity in a region of interest in the phantom to the number or counts per unit activity for a source in air at the same phantom location (expressed as a percentage) (King *et al* 1991).

$$\text{Air sensitivity}(\%) = \frac{(\text{Number of counts in ROI} / \text{Activity in ROI}) \times 100}{\text{Detected counts for a point source in air} / \text{Activity of the point source}} \quad (5.7)$$

Clearly, an ROI with a percentage air sensitivity of 100% means a perfect match between the estimated activity in the ROI and the expected number of counts for a point source in air in which photon attenuation and scatter are not present. Seven regions of interest were selected in the source distribution, one for each segment of the annulus, to measure percentage air sensitivity.

Each region of interest was composed of $2 \times 2 \times 1$ pixels and drawn from the original source distribution used as input for the Monte Carlo simulation. The averaged number of counts in an ROI was measured in the reconstructed images. The theoretical source distribution which contained the effect of the detector blurring (figure 5.3b) was employed to calculate the activity.

In order to obtain the point air sensitivity, a tomographic acquisition of a point source in air was Monte Carlo simulated for the two photon energies (75 keV and 140 keV) using a symmetric energy window of 20%. The point source was assumed to be located within the annulus at the maximum intensity circular profile (described in section 5.3.1). The point source sensitivity in air was found to be 11.11 kilo counts and 11.83 kilo counts per million emitted photons for 75 keV and 140 keV photons, respectively.

5.4. Results and Analysis

The program traced 427×10^6 photon histories for two photon energies, 75 keV and 140 keV. The total number of detected photons summed over all the projections, the scatter fraction and the required computing time are presented in table 5.1. The CPU time quoted in this table corresponds to an average when using different Sun workstations.

Table 5.1. Monte Carlo simulation output of the emission phantom.

Energy (keV)	CPU (days)	Primaries ($\times 10^5$)	Scattered ($\times 10^5$)	Total[a] ($\times 10^5$)	Scatter fraction
75	6.5	7.06	7.64	14.70	1.083
140	9.9	10.31	6.01	16.32	0.584

[a] *Primary plus scattered events*

These data show that the effects of attenuation and scatter are more significant for low energy photons. The attenuation of 75 keV photons produced 31.5% less primary photons than the corresponding value quoted for 140 keV photons. It also noticeable that the scatter fraction, defined as the ratio of scattered to primary events, is higher for the lower energy case.

Fifty-six horizontal profiles were averaged in the projections in order to improve image statistics. Image reconstruction was performed with the ML-EM Program with and without attenuation compensation. The attenuation maps reported in Chapter 4 for the flood and collimated line sources were used for the attenuation compensation analysis.

Since the emission data were separated as primary and primary plus scattered events, the attenuation maps used for the attenuation compensation were selected according to the type of external source geometry with which they were generated. It was expected that the reconstruction of primary events would require the use of narrow beam attenuation coefficients whereas the reconstruction of primary plus scattered events would require the use of effective attenuation coefficients to partially compensate for the imaging of scattered photons. It was also expected that the image quality would be affected when effective attenuation coefficients were used in the reconstruction of primary events and, similarly, when narrow beam attenuation coefficients were used in the reconstruction of scatter contaminated data.

On the basis of the previous arguments, four combinations of emission-transmission data were considered during image reconstruction with attenuation compensation. These combinations are shown in table 5.2. The second column of table 5.2 (denoted as *AC*) indicates whether attenuation compensation was used during image reconstruction or not. These combinations are referred to as cases A, B, C, D, E and F (last column in table).

Several examples of the reconstructed images are shown in figure 5.4. The images are separated in terms of: photon energy (75 keV and 140 keV), type of reconstruction (with or without attenuation compensation) and type of emission data (primary or primary plus scattered events). The reconstruction of primary and total events with attenuation compensation utilised the emission-transmission cases B and F as shown in table 5.2.

Table 5.2. Emission-transmission data combinations used during image reconstruction with the ML-EM program (with and without attenuation compensation).

Emission		*Transmission*			
Type of events	AC[a]	Source	Type of events	Comments	Case
Primaries	No	----	----	No attenuation compensation applied.	A
	Yes	Line	Primaries	Ideal case where scattered photons are not present in any of the tomographic acquisitions. Narrow beam attenuation coefficients apply.	B
	Yes	Flood	Total	This combination investigates the effect of using effective attenuation coefficients in the reconstruction of scatter free emission data.	C
Total[b]	No	---	---	No attenuation compensation applied.	D
	Yes	Line	Primaries	This combination investigates the effect of using narrow beam geometry attenuation coefficients when reconstructing scatter contaminated emission data.	E
	Yes	Flood	Total	The effective attenuation coefficient was used to partially compensate for the presence of scattered photons in the emission data.	F

[a] Attenuation compensation.
[b] 20% energy window centred on the photopeak.

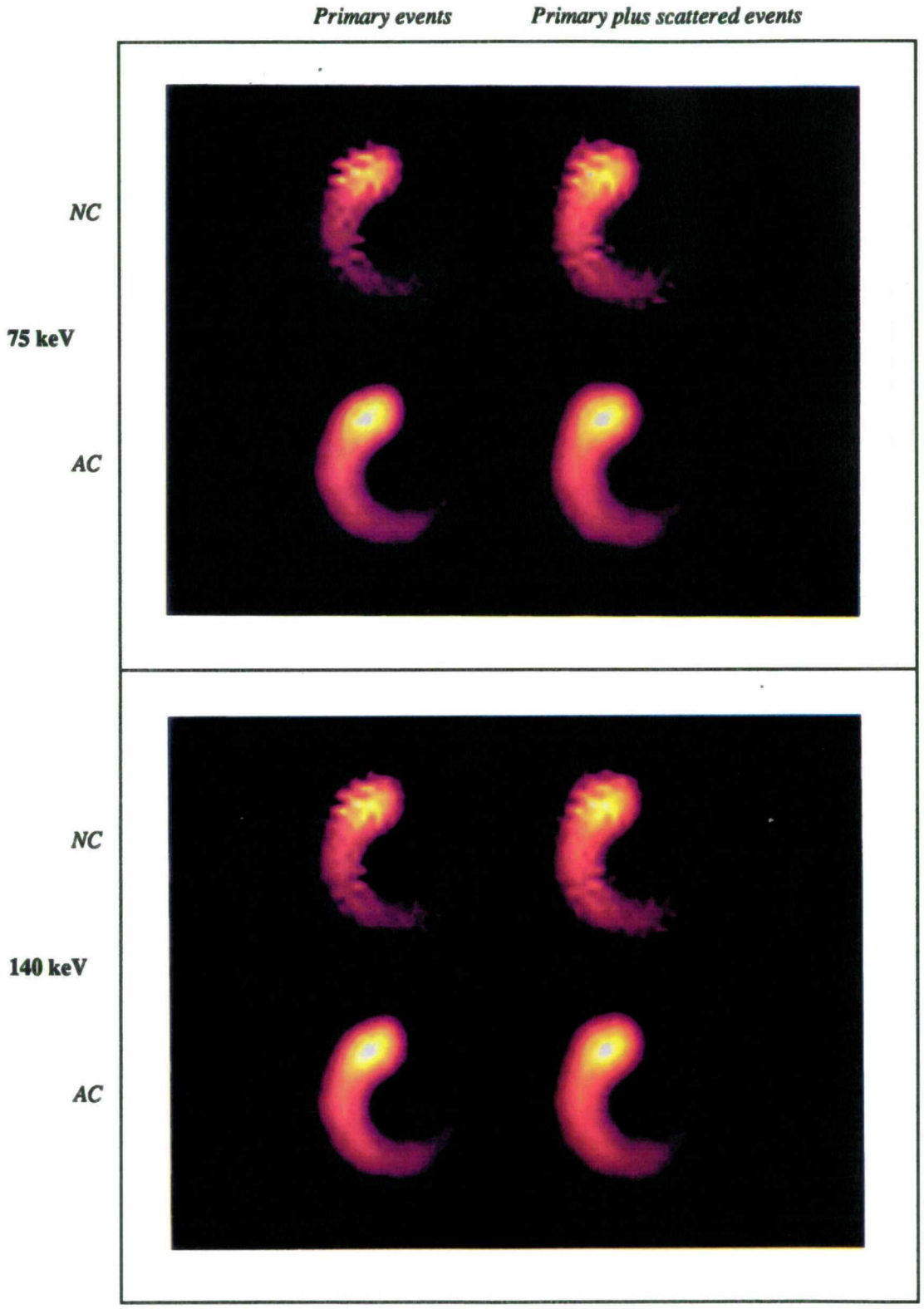

Figure 5.4. Tomographic reconstructions of the emission phantom. The following notation was used: *NC* no attenuation compensation, *AC* with non-uniform attenuation compensation.

5.4.1. Relative Quantification

For each case listed in table 5.2, the circular profiles were extracted and normalised with respect to the maximum intensity. The maximum intensity was chosen as the normalisation factor because it represented the best estimation of the activity for the segment of the annulus with the largest activity concentration (including the partial volume effect). Plots of these profiles as a function of angle are shown in figure 5.5a and 5.5b for the two energies used in this study.

The *FD*s are plotted in figures 5.6a and 5.6b for the two energies employed in this study. The mean value and the standard deviation of the fractional differences were calculated for each profile. The relative activities 1 and 2 were excluded from the calculation of the *FD's* mean values for the cases *D*, *E* and *F* since, at it will be discussed later, these regions presented the largest over-estimation in the number of counts. These results are presented in table 5.3.

Several observations can be drawn from the plots and table:

Primary events (cases A, B and C):

- Reconstruction of the emission data without attenuation compensation under-estimated the number of counts in all parts of the image. This effect was more prominent for 75 keV photons. Statistical fluctuations in the intensity distribution were also more important for 75 keV photons.

- The use of narrow beam attenuation coefficients during image reconstruction with attenuation compensation generated the best estimation of the number of counts in the whole range of activity concentrations. The largest deviation from zero were approximately -13% and -11% for 75 keV and 140 keV, respectively. The corresponding mean values for these two cases were -4% and -1%. This indicated that for 75 keV photons there was a slight under-estimation in the number of counts.

- There was a under-estimation in the number of counts for all parts of the image at both energies when effective attenuation coefficients were used in the attenuation compensation algorithm during image reconstruction.

Total events (cases D, E and F):

- The imaging of scattered events produced an over-estimation on the number of counts in most parts of the reconstructed images which was greater for low activity concentrations. The large number of scattered photons in the 75 keV study (scatter fraction approximated 1.1) produced a more significant effect. The reconstruction of the images without attenuation compensation predicted number of counts with large deviations from the theoretical image in the whole range of activity concentrations.

- Image reconstruction of total events with non-uniform attenuation compensation and narrow beam attenuation coefficients produced an over-estimation in the number of counts throughout the whole range of activities.

- The use of effective attenuation coefficients during image reconstruction produced an over-estimation of the number of counts in regions with low activity concentrations. This can be observed from the plots presented in figures 5.5 and 5.6. In spite of this, this case provided the best prediction of the number of counts when reconstructing emission data containing scattered photons. The best prediction of the number of counts within the relative concentration range of 4-16 was lower than 2% for both energies.

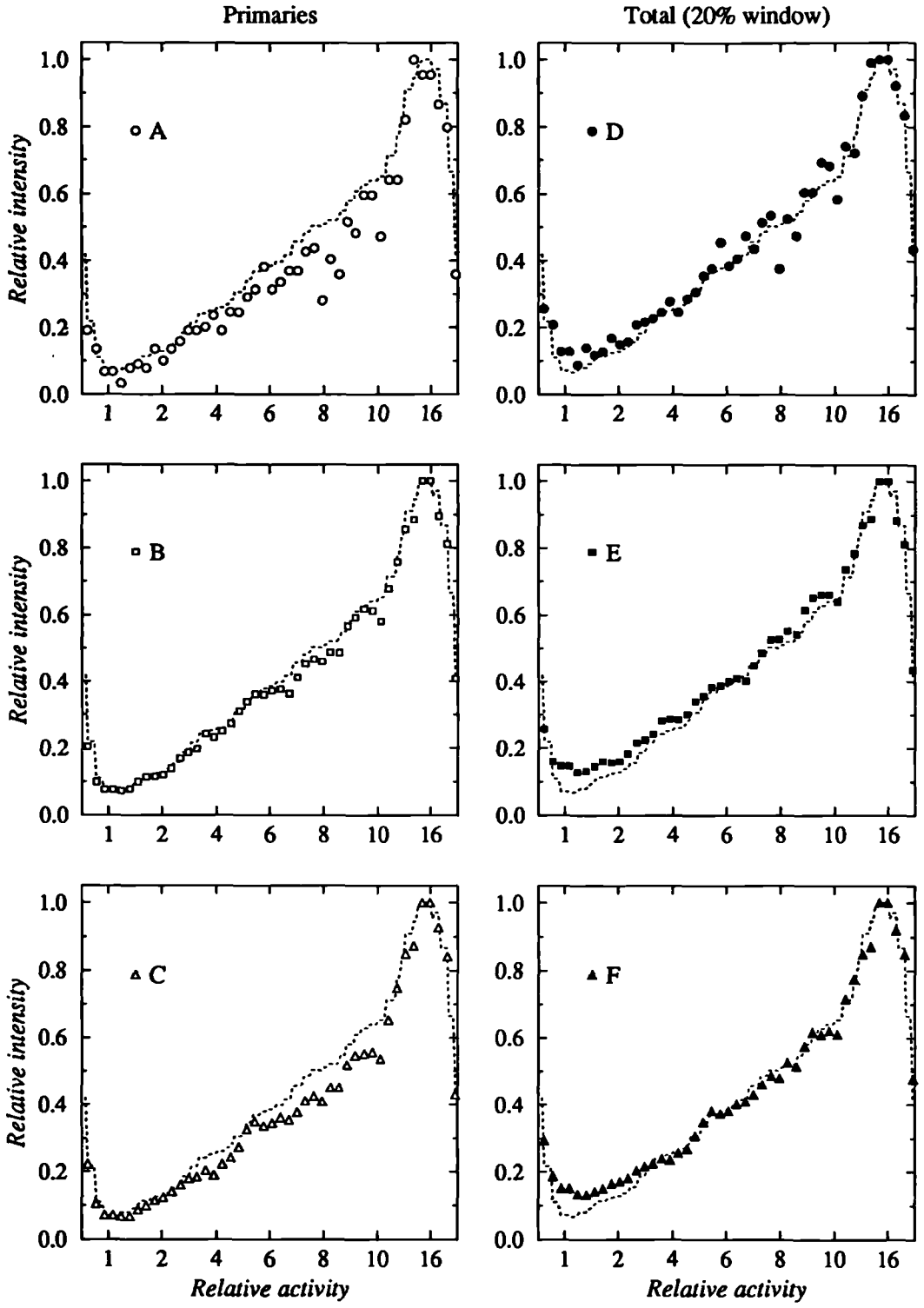

Figure 5.5a. Circular profiles of the reconstructed images at the maximum radial intensity for 75 keV photons. The data are normalised with respect to the maximum number of counts and represent the transmission-emission data combinations presented in table 5.2. The dotted line represents the theoretical prediction.

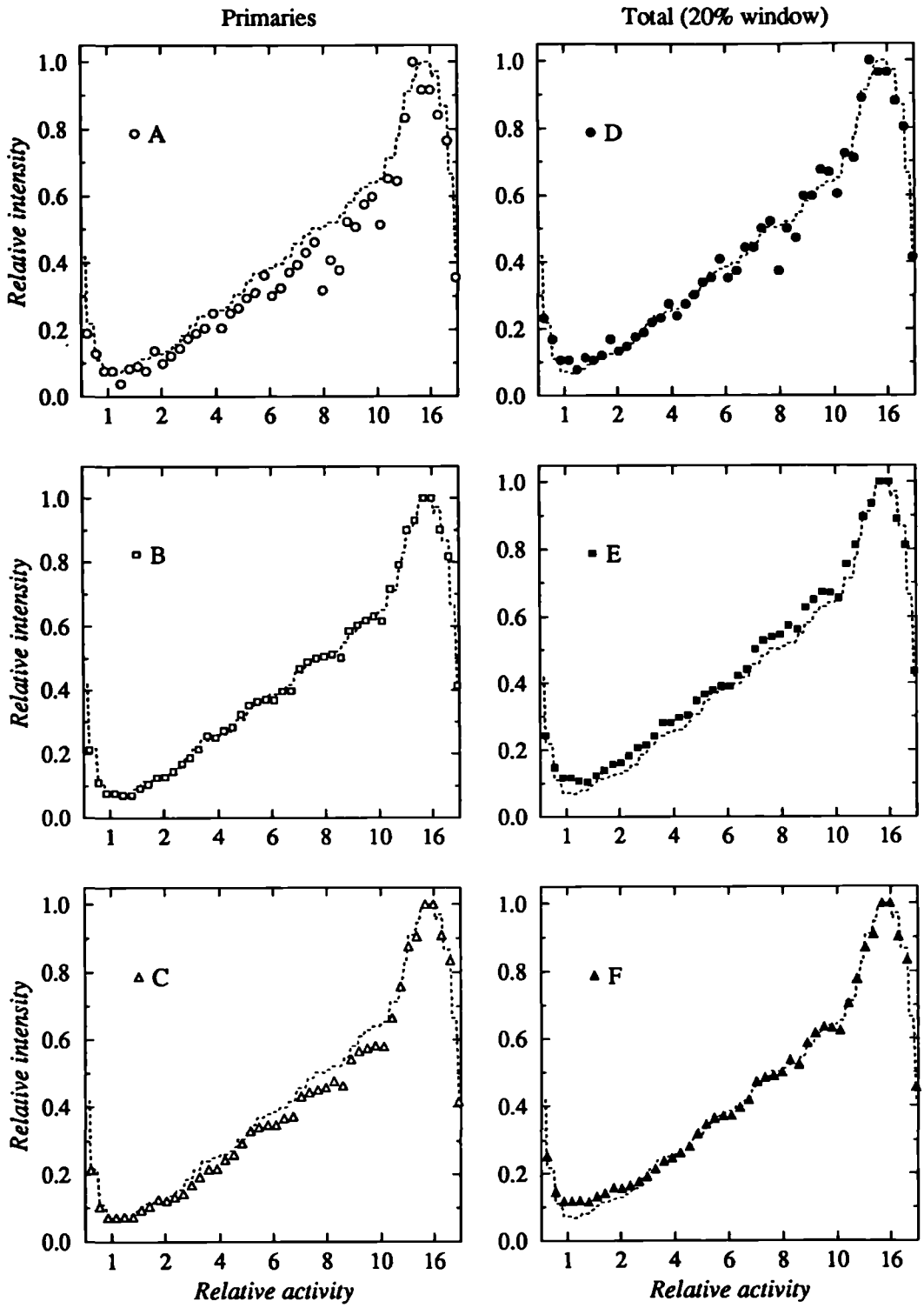

Figure 5.5b. Circular profiles of the reconstructed images at the maximum radial intensity for 140 keV photons. The data are normalised with respect to the maximum number of counts and represent the transmission-emission data combinations presented in table 5.2. The dotted line represents the theoretical prediction.

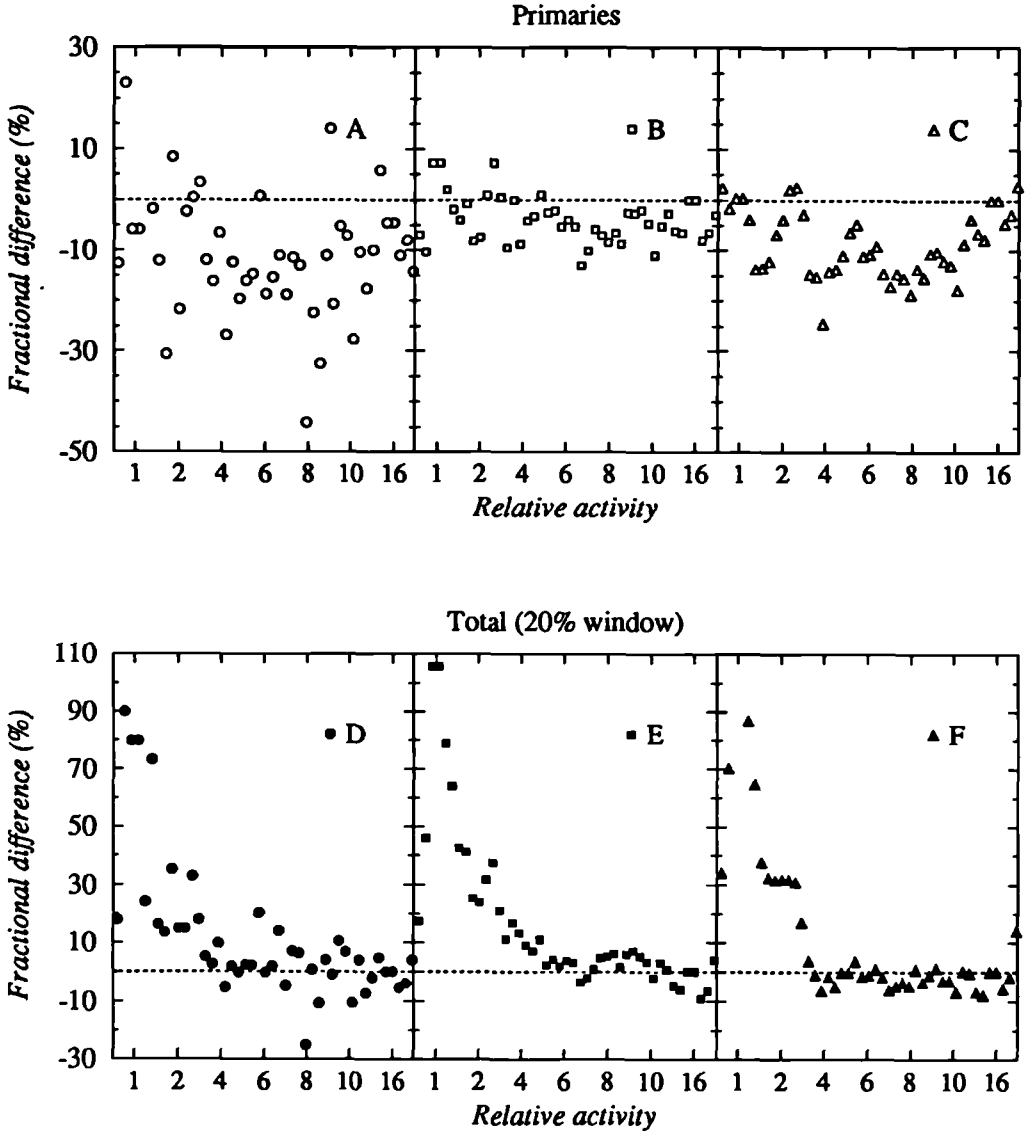

Figure 5.6a. Plot of the fractional difference (expressed as a percentage) between the estimated circular profiles (cases A, B, C, D, E and F) and the theoretical source distribution for 75 keV primary photons. The dotted line corresponds to the ideal case (zero difference).

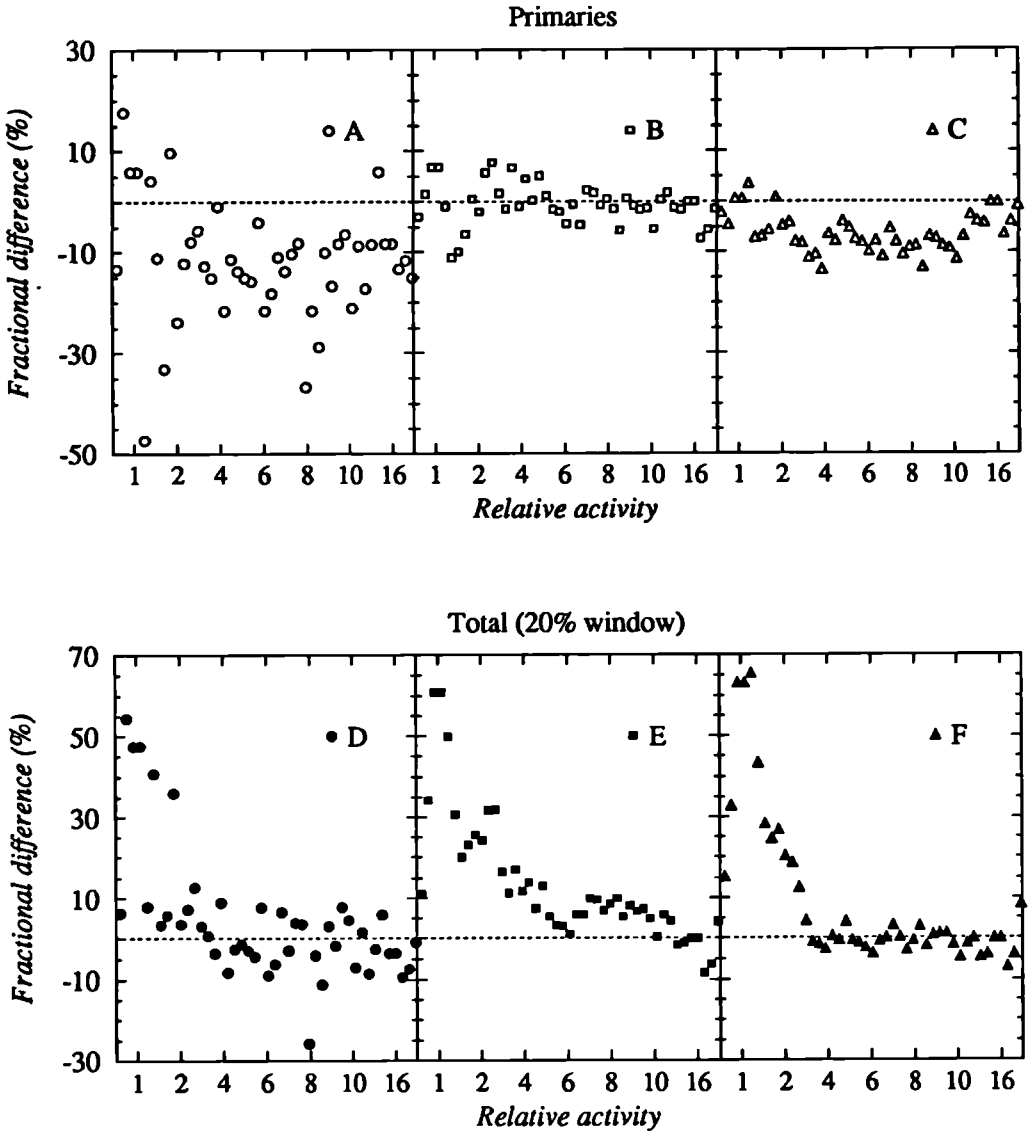

Figure 5.6b. Plot of the fractional difference (expressed as a percentage) between the estimated circular profiles (cases A, B, C, D, E and F) and the theoretical source distribution for 140 keV primary photons. The dotted line corresponds to the ideal case (zero difference).

Table 5.3. Mean value of the fractional differences of the circular profiles at maximum radial intensity obtained with the image reconstruction.

	75 keV		*140 keV*	
Case	*FD (%)*	*ΔFD*	*FD (%)*	*ΔFD*
A	-12.54	12.94	-12.26	11.72
B	-4.09	4.39	-0.75	4.14
C	-8.97	6.38	-6.21	3.71
D[a]	1.13	8.77	-2.20	7.23
E[a]	3.19	5.90	5.63	5.74
F[a]	-1.82	3.22	-0.85	2.68

[a] Excluding relative activities 1 and 2.

5.4.2. Absolute Quantification

The percentage air sensitivities for the two photon energies (75 keV and 140 keV), the seven activity concentrations and the different combinations of emission-transmission data are listed in table 5.4 and plotted in figure 5.7. The different cases listed in the first column correspond to the transmission-emission data combinations listed in table 5.2. Several conclusions can be drawn from the table and from the plots:

- Image reconstruction of source distributions without attenuation compensation produced images with a significantly decreased percentage air sensitivity.
- Image reconstruction of source distributions with non-uniform attenuation compensation increased the number of counts in approximately 500% when compared to data reconstructed without attenuation compensation.
- The use of narrow beam attenuation coefficients predicted the best sensitivities when scatter-free data were reconstructed with attenuation compensation. The estimated percentage air sensitivity differed by approximately 8% from the ideal value for both energies (75 keV and 140 keV). When primary plus scattered events were reconstructed with the same type of attenuation coefficients, the sensitivities were over-estimated, particularly in regions of low activity concentrations.
- The use of effective attenuation coefficients in the reconstruction of primary photons with attenuation compensation produced an under-estimation of sensitivities in the whole range of activity concentrations. When primary plus scattered events were reconstructed with the same type of attenuation coefficients there was an under-estimation of sensitivities in regions of medium or high activity concentrations and an over-estimation in regions of low activity concentrations. However, this case represented the best estimation when all the events (primary plus scattered) were used in the reconstruction.

Table 5.4. Percentage air sensitivity computed for 75 keV and 140 keV photons. *RA*: relative activity in annulus, *AS*: percentage air sensitivity, ΔAS: percentage air sensitivity uncertainty.

		75 keV		*140 keV*	
Case	*RA*	*AS (%)*	ΔAS	*AS (%)*	ΔAS
A	1	17.72	7.69	23.64	10.04
	2	14.47	2.08	20.12	3.47
	4	12.70	2.19	18.63	3.25
	6	13.31	0.66	18.43	1.02
	8	13.67	1.47	19.06	1.39
	10	13.64	1.83	19.60	2.01
	16	16.11	1.07	21.53	1.25
B	1	98.65	28.87	99.67	31.37
	2	93.93	4.49	95.45	5.52
	4	94.87	9.14	98.09	9.35
	6	93.37	7.15	93.55	5.95
	8	93.84	6.02	92.86	7.27
	10	91.73	6.27	93.23	5.56
	16	96.84	4.51	94.57	4.00
C	1	65.23	20.27	69.98	21.59
	2	61.22	4.42	70.02	3.81
	4	51.84	5.86	63.26	7.32
	6	55.35	5.89	64.59	4.52
	8	54.25	4.27	64.63	4.26
	10	55.32	2.92	64.55	3.96
	16	63.97	2.44	70.84	2.91
D	1	34.22	12.78	36.50	13.83
	2	21.86	2.57	27.60	4.05
	4	17.70	2.24	22.70	2.96
	6	18.54	0.86	23.04	1.29
	8	18.74	1.56	23.60	1.40
	10	18.66	1.84	24.24	1.99
	16	18.35	0.77	23.64	1.14
E	1	215.01	56.44	162.65	47.12
	2	160.66	6.58	140.59	6.07
	4	140.77	10.41	124.93	9.76
	6	127.24	9.03	115.80	6.94
	8	131.04	8.29	116.95	9.54
	10	124.24	7.71	113.75	6.60
	16	118.86	6.42	107.87	5.05
F	1	150.59	39.88	119.15	33.29
	2	105.22	4.86	103.20	3.89
	4	75.71	6.11	79.68	7.55
	6	75.48	7.36	79.91	5.03
	8	76.20	6.16	81.34	5.85
	10	75.28	4.08	79.12	4.93
	16	76.49	3.67	80.00	3.75

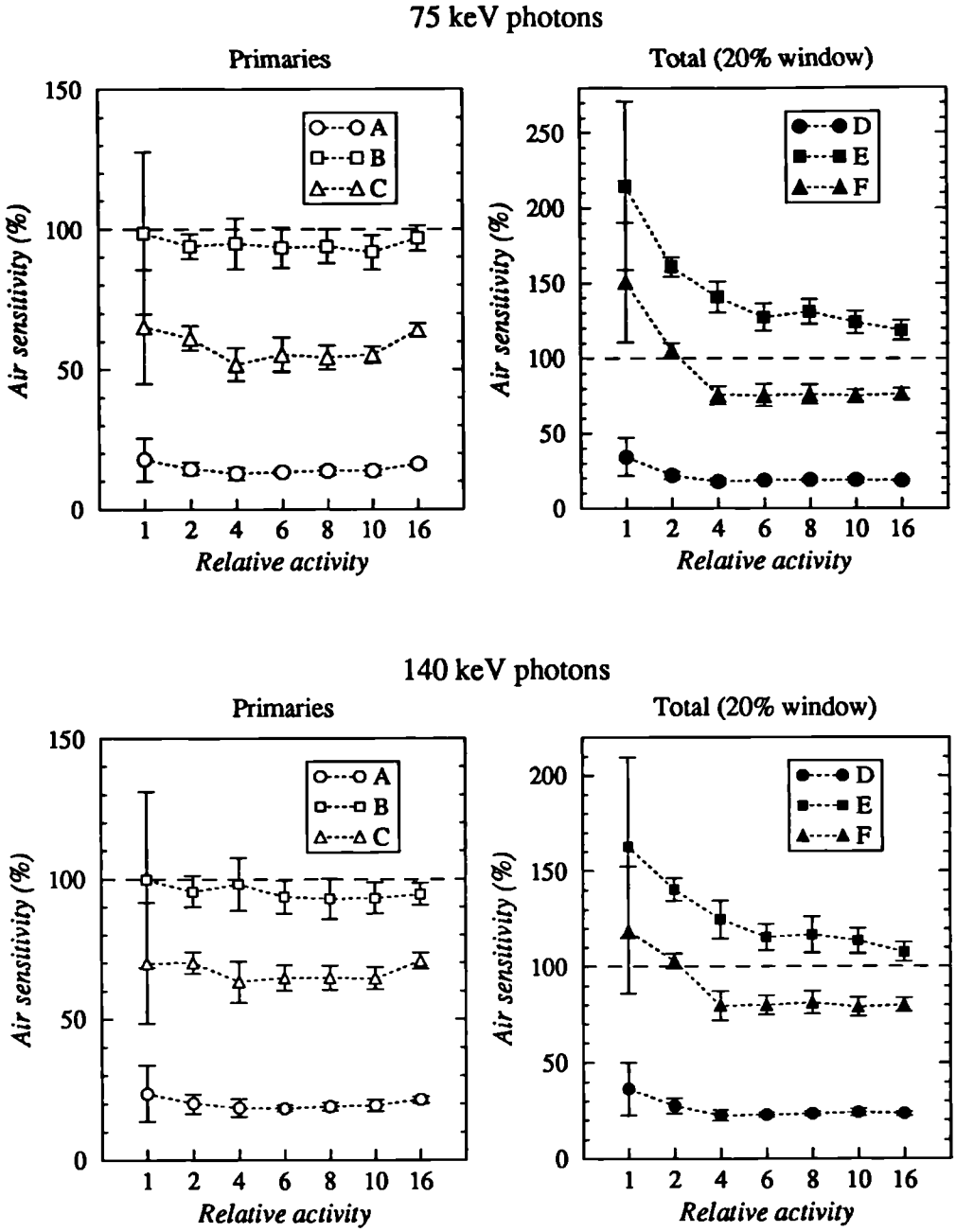

Figure 5.7. Percentage air sensitivities for 75 keV and 140 keV photons measured relative to the predicted source distribution including the effect of detector blurring (figure 5.3b). The dotted line indicates the ideal case.

5.4 Conclusions

The analysis presented in this chapter indicates that quantification in SPECT imaging can only be achieved if the reconstructed images are corrected for the most important degrading factors involved during image acquisition.

It was found that 140 keV photons produced improved image quality with smaller statistical fluctuations than the corresponding images produced with 75 keV photons.

Image reconstruction without attenuation compensation produced images with a substantial decrease in the predicted activity over the whole range of activity concentrations. This effect was clearly shown when absolute quantification was performed irrespective of whether the emission data contained primary or primary plus scattered events. Another interesting feature of the reconstructed images without attenuation compensation was the presence of large statistical fluctuations on the predicted number of counts.

The ML-EM program with attenuation compensation produced the best estimations of number of counts and sensitivities in the whole range of activity concentrations present in the phantom. This finding was particularly important when the reconstructed data contained only primary events and the map used in the attenuation compensation algorithm represented narrow beam attenuation coefficients.

The presence of scattered photons in the emission data hindered both relative and absolute quantification, particularly in regions of low activity concentrations. In both cases it was observed an over-estimation of the number of counts in all the regions of the reconstructed images when narrow beam attenuation coefficients were used. The utilisation of effective attenuation coefficients during attenuation compensation produced both under-estimation and over-estimation in the number of counts in different regions of the images. However, this case represented the best estimation when all the events were used in the reconstruction.

The best percentage sensitivity was found for scatter-free data reconstructed with narrow beam attenuation coefficients. In this case, the estimated percentage air sensitivity differed by approximately 8% from the ideal value for both energies, 75 and 140 keV.

CHAPTER 6

Emission-Transmission Tomography in Myocardial Imaging

As discussed in Chapter 1, thallium 201 SPECT myocardial perfusion imaging is a non-invasive nuclear medicine technique to diagnose the existence of lesions in the myocardium and to specify their location. Despite the quantitative potentials of SPECT imaging, this technique has been normally used qualitatively since the problem of photon attenuation within the thorax (amongst other factors) limits the accurate determination of activity concentrations. This chapter presents a test of the Monte Carlo simulated system presented in the previous chapters using an anthropomorphic phantom. Tomographic images of myocardial and lung radionuclide uptake were simulated. A transmission study with the same tomographic system and a collimated line source was also simulated to obtain the attenuation maps. These attenuation maps were used to compensate the emission data for non-uniform photon attenuation.

6.1. Simulation of a Realistic Thorax Phantom

A thorax phantom was generated for the simulation using x-ray computed tomography (CT) scans as input data. The CT images are two-dimensional matrices of volume elements (voxels) whose values represent an average of the attenuation coefficients of the tissues contained in each voxel.

The simplest approach to include this mathematical phantom into the Monte Carlo simulation was to consider each individual voxel as an independent region with the medium contained in that voxel completely determined by its grey level value on the CT scan. This approach required the definition of an extremely large number of regions in the computer program producing a very accurate but inefficient code, even if using CT images of medium or low resolution. For example, a set of 19 images of 128x128 pixels needed the use of 311296 regions.

A more practical and efficient method consisted in grouping all those pixels that represented the same tissue and were next to each other to form cuboids. In order to apply an algorithm of this nature it was necessary first to define grey level intervals that represented homogeneous tissue materials. For this, the attenuation coefficients of the most abundant tissues forming the thorax were determined within a range of photon energies. The tissues selected were: lung, heart (with and without blood), muscle, adipose, skin and two types of bone, cortical and spongiosa.

The linear attenuation coefficient associated with each tissue depends on its composition and density. The elemental composition of these tissues depends upon the relative amounts and composition of water, lipid, protein, carbohydrate and minerals. The linear attenuation coefficients of the selected tissues were calculated from Storm and Israel (1970) and plotted as a function of energy (figure 6.1). Compositions of body tissues as reported by Woodard and White (1986) were used.

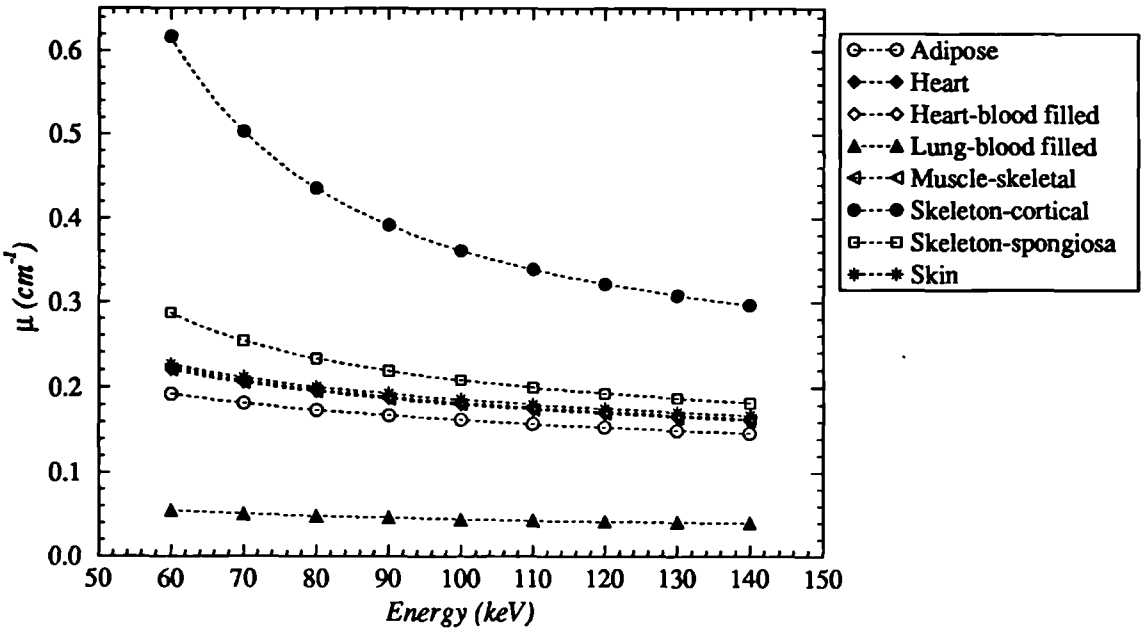

Figure 6.1. Linear attenuation coefficient for several tissues found in the thorax.

It can be observed from the graph that the heart (with and without blood) and skin can be enclosed in a single group represented by muscle tissue. Their attenuation coefficients are within 3.5% of the attenuation coefficients of muscle for the range of energies considered in this study. Taking this fact into account, it was concluded that

the most important differences in linear attenuation coefficients were due to cortical bone, spongiosa, muscle, adipose and lung.

The selection of grey level intervals associated with each tissue type was carried out in the following manner. The CT images were displayed on the computer and compared to an atlas of cross sectional anatomy with correlated imaging (Bo *et al* 1990). This atlas contains photographs of cross sections of the human body with correlated CT, MRI and ultrasound images. Grey level windows were selected and associated with a tissue material by direct comparison with the images shown in the atlas. Afterwards, an algorithm (described below) was used to reduce the number of regions within the Monte Carlo program.

The grouping of the regions was performed using an algorithm (UNION) developed initially in a Monte Carlo calculation of dose distributions in electron beam radiotherapy treatment planning (Manfredotti *et al* 1990). This algorithm produces a mathematical description of the CT images in terms of boxes of varying dimensions, each box containing a homogeneous tissue defined by a grey level interval. The most important characteristic of this method is that the media contour is not modified after the application of this procedure. To illustrate the algorithm, let us consider for simplicity a single image of 9x9 pixels containing three types of media represented by a, b, c (see figure 6.2).

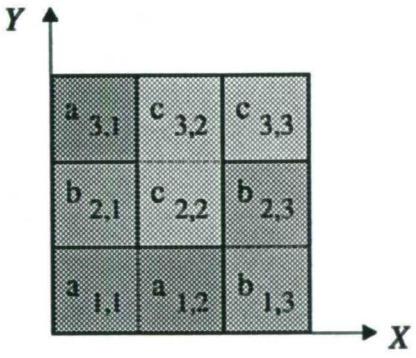

Figure 6.2. Application of the UNION algorithm to an image of 9x9 pixels.

In a two-dimensional image UNION starts by scanning the *X* direction followed by the *Y* direction. Scanning of the image is performed by starting at element (1,1) and proceeding row by row. In this example, pixels (1,1) and (1,2) contain the same material and are joined together to form a single region. The order of the scan causes pixels (1,3) and (2,3) to be joined into a single box as well as pixels (2,2) and (3,2). The number of regions has been reduced from 9 (the total number of pixels in the

image) to only 6. Clearly, the total number of regions will depend on the complexity of the image and on the number of materials represented by the grey level intervals.

When the algorithm is applied to a set of CT images in three-dimensional space the scan is performed in the *X*-, then in the *Y*- and finally in the *Z*- direction. The choice of scanning the Z dimension last is due to the different spatial resolution in this direction (the distance between *Z*-planes is normally greater than the distance between *X*- and *Y*-planes). Swapping the precedence of *X*- and *Y*- does not cause appreciable variation on the resulting box number.

Orthogonal geometry was desirable to produce an efficient program. This was accomplished by aligning the images parallel to the *X*, *Y* and *Z* axes of coordinates. The geometry of every box was completely defined by two opposite vertices joining a diagonal through the box. They were selected according to the largest and smallest *X*, *Y* and *Z* values. The orientation of a box and the selection of the vertices, represented by the vectors (x_a, y_a, z_a) and (x_b, y_b, z_b), are shown in figure 6.3.

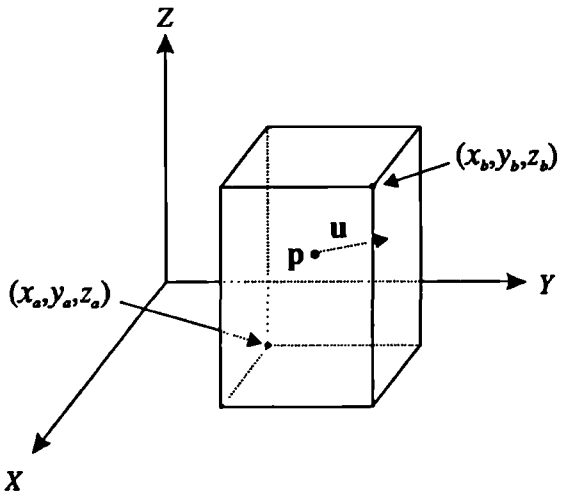

Figure 6.3. The geometry of a box can be completely defined in terms of two opposite vertices joining a diagonal through the box.

The use of "boxes of media" means that the photon transport within a box is a simple process. Consider, for example, a photon inside a box with a position defined by the vector $\mathbf{p} = (x, y, z)$ and direction cosines $\mathbf{u} = (u, v, w)$. Let us assume that the direction of the photons is in the positive direction, that is $(u, v, w) > (0, 0, 0)$. The intersection of the photon trajectory with any of the sides of the box is given by:

$$t = \min\left(\frac{x_b - x}{u}, \frac{y_b - y}{v}, \frac{z_b - z}{w}\right) \tag{6.1}$$

As can be observed, only three operations are required to calculate the distance to the next boundary. Similar expressions can be derived for any photon direction within the box. This technique produces a very efficient code in terms of computational speed.

The UNION algorithm was used in the thorax simulation to reduce the number of regions in the phantom. Nineteen contiguous CT images were used as input data for the Monte Carlo simulation. The images had an original format of 128x128 pixels that were reduced to 128x92 pixels by removing regions containing only air. The total number of regions used in the simulation of the thorax phantom was of the order of 25000. The system of coordinates and the orientation of the images are shown in figure 6.4.

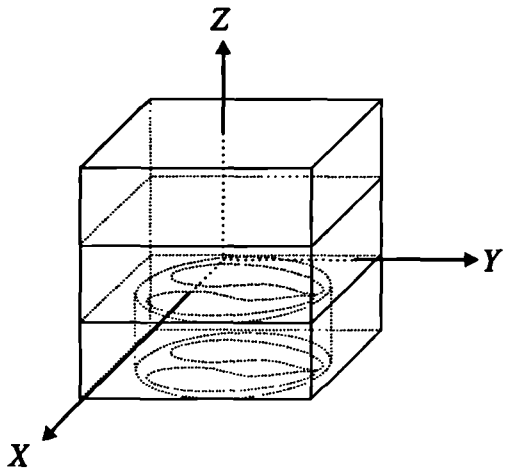

Figure 6.4. Alignment of the CT images in the Cartesian system of coordinates.

The CT images were aligned parallel to the *XY* plane separated by a distance ΔZ according to the slice thickness of the original CT scan. The physical dimensions of the CT images corresponded to a pixel size of 0.25x0.25 cm^2 in the *X-Y* directions and of 1.0 cm in the *Z* direction. Figure 6.5 shows an example of an original CT image, its transformation into five grey scale levels and the geometric simplification into boxes after the application of the UNION algorithm. The original image in figure 6.5a contained 11776 regions (pixels) which were subsequently reduced to only 1358 after using UNION.

a)

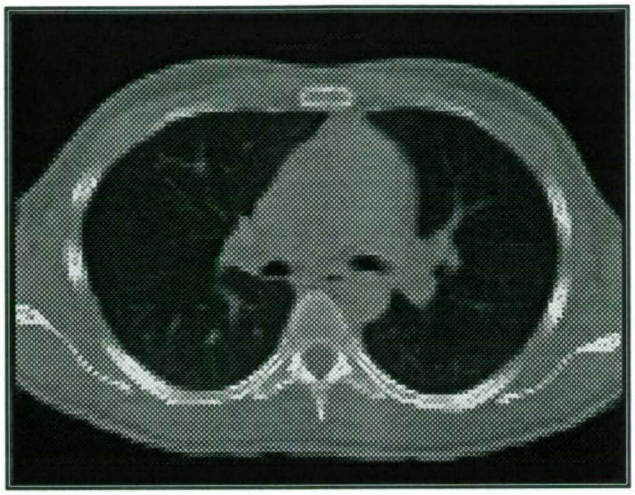

b)

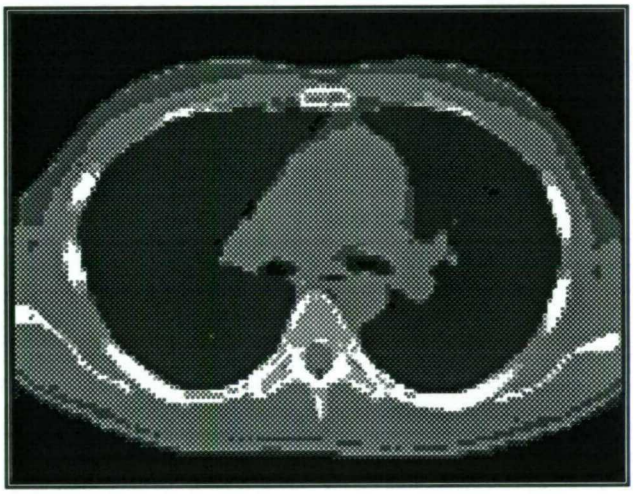

c)

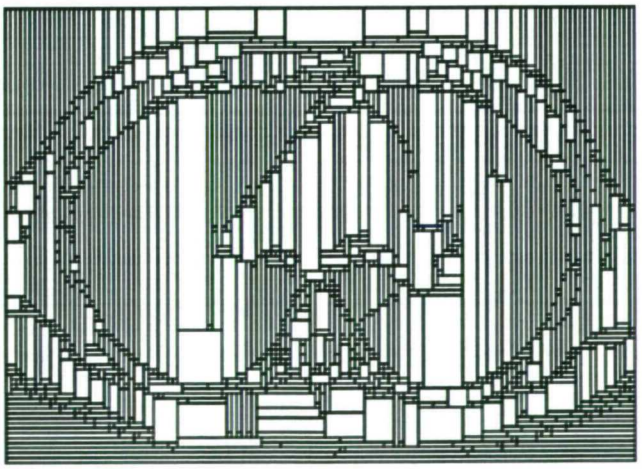

Figure 6.5. Geometric simplification of the CT images: a) Original image with 256 grey scales. b) Reduction to five grey level intensities corresponding to lung, adipose, muscle, spongiosa and cortical bone. c) Box representation after the UNION algorithm was applied to image b).

6.2. Description of the Simulations

6.2.1. General Features

The emission and transmission studies were carried out according to the procedures described in Chapter 1, sections 1.6.2 and 1.6.3. The simulations assumed a circular orbit with a radius of rotation of 22.5 cm, a 20% energy window centred on the photopeak and a 64x64 image format (0.64 cm pixel size). This radius of rotation allowed the external source and collimator to rotate without touching any of the boxes defined in the thorax phantom. Several sets of images were produced for each study considering only primary or primary plus scattered events.

Image acquisitions of uniform source distributions in the lung and myocardium were simulated assuming 64 projections over 360°. A 360° rotational arc was used instead of a 180° arc since the former case presents greater photon attenuation. In order to compare results produced with the two radionuclides clinically important in myocardial perfusion imaging, two photon energies were used: 75 keV and 140 keV, corresponding to the main photon energies of ^{201}Tl and ^{99m}Tc. Image reconstruction was performed with the ML-EM (with and without attenuation compensation) and the results compared with images produced with a filtered back-projection (FBP) program (Ramp-Hanning filter, cut-off frequency 0.8 cycles/cm), a commonly used reconstruction algorithm in cardiovascular nuclear imaging.

A transmission study with the same tomographic system as the emission study and a ^{99m}Tc collimated line source was also simulated to obtain the attenuation maps. Thirty-two projections over a 180° arc were assumed. The attenuation correction for ^{201}Tl emission data required the transformation of the 140 keV attenuation maps to the appropriate energy (75 keV). To this end, a second order polynomial transformation was used as suggested in Chapter 4 (section 4.3.2).

6.2.2. Transmission Study

Figure 6.6 shows the dimensions of the tomographic system used in the program. The system consisted of the thorax phantom, a scanning line source and the gamma camera fitted with a LEGP collimator. A scanning line source was used due to its high efficiency performance as compared to the efficiency of a flood source. The source

scanned an area of $19.0 \times 39.4\ cm^2$ parallel to the *YZ* plane and centred at the mathematical centre of the phantom. The maximum azimuthal angle of photon emission ($\Delta\varphi$) that defined the slit aperture was chosen as 2°. This aperture produced a scatter fraction of less than 3.6% in all the planar acquisitions.

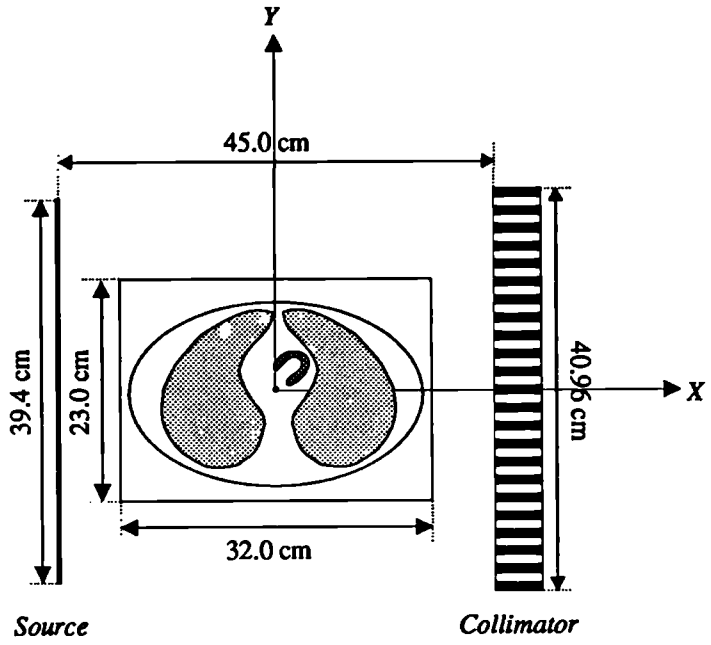

Figure 6.6. Dimensions of the tomographic transmission system.

As described in Chapter 1, each photon reaching the collimator face was associated with a vector **r** whose components contained information on the photon history. In this study, the photon vector was given by:

$$\mathbf{r} = (y_f, z_f, \theta, \varphi, E, NI) \tag{6.2}$$

where (y_f, z_f) is final photon position, (θ, φ) are the polar and azimuthal angles which define the final photon direction, E is the final photon energy and NI is the number of interactions that the photon underwent inside the phantom. The photon position and direction were defined with respect to a fixed system of coordinates at projection $\alpha = 0°$. Each photon history was stored on a file for further processing with the collimator program.

6.2.3. Emission Study

For the emission study the original CT images had to be modified to simulate radionuclide uptake in the myocardium and background in the lungs. For this, the

original images were displayed on a graphics workstation and compared to an atlas of sectional anatomy with correlated imaging (Bo *et al* 1990). The myocardium was drawn by selecting regions of interest on the displayed images according to the anatomy of the myocardium shown in the atlas. The dimensions of the myocardium with respect to the size of the patient were carefully maintained. The boundaries of the lung were extracted from the CT images using a threshold grey level value. A uniform activity was assumed to be distributed in the myocardium and in the lungs, with a lung to heart ratio of 0.2. Nine of the nineteen CT images used in the simulation are shown in figure 6.7, displaying the activity distribution in both the myocardium and lung.

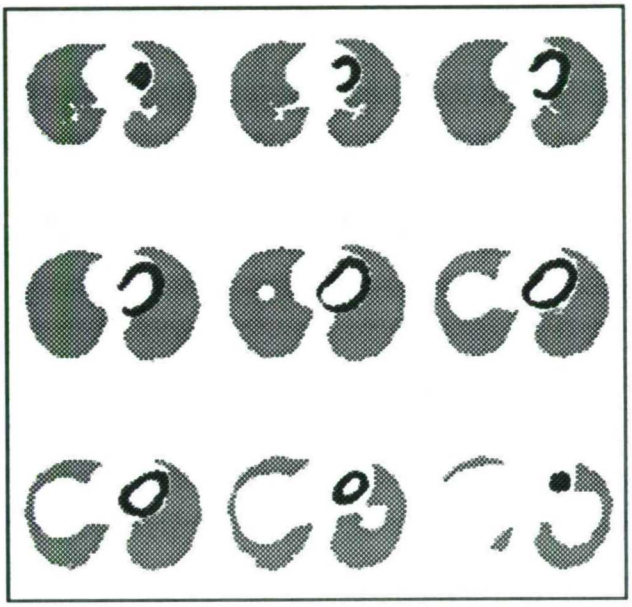

Figure 6.7. Uniform activity distributions in lung and myocardium used as input in the Monte Carlo simulation.

The geometry and dimensions of the tomographic system were kept the same as in the transmission study depicted in figure 6.6. The output of the thorax program consisted of a set of vectors (one for each photon) whose components were associated with photon parameters. Each vector was given by:

$$\mathbf{r} = (\beta, z_f, \theta, \varphi, E, NI) \tag{6.3}$$

where (β, z_f) is the final photon position in polar coordinates, (θ, φ) are the polar and azimuthal angles which define the final photon direction, E is the final photon energy and NI is the number of interactions that the photon underwent inside the phantom.

The collimator program read the set of vectors $\{\mathbf{r}\}$ as input data and proceeded with the photon transport through the collimator.

6.3. Relative Quantification

Relative quantification was carried out by comparing horizontal profiles drawn across the reconstructed images and the theoretical source distributions. The theoretical images were obtained by convolving the original source distribution (figure 6.7) with the calculated point spread function of the tomographic imaging system. The point spread function was assumed to be Gaussian in shape (FWHM=1.4 cm), spatially invariant and its spread was calculated for a radius of rotation of 22.5 cm considering the collimator resolution and the intrinsic spatial resolution of the gamma camera. A single slice of the theoretical prediction of the source distribution after convolution is shown in figure 6.8 (corresponding to slice 4 in figure 6.7).

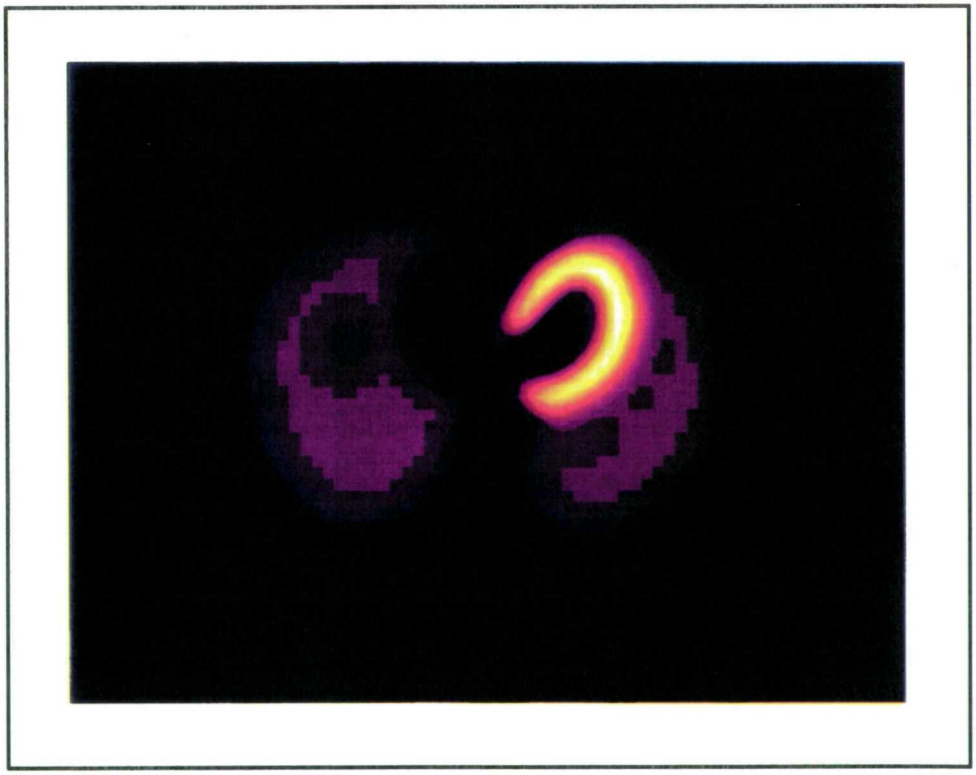

Figure 6.8. Theoretical prediction of source distribution using a Gaussian blurring (FWHM=1.4 cm).

6.4. Results of the Transmission Study

6.4.1. Attenuation Maps for ^{99m}Tc

The program ran for 400×10^6 histories per projection divided between 4 computers (typically Sun SPARCstation IPX) processing 100×10^6 events each. The total study required an average of 700 hours (29 days) of computing time per machine. Considering the solid angle employed in the collimated line source, 100×10^6 events corresponded to an activity of 385.2 MBq (10.41 mCi) on the basis of 30 seconds per projection. This activity produced approximately 2×10^6 counts in the simulation of the blank image (that is, with the thorax phantom removed) corresponding to a count rate of 67 kcps. This value seems to be within the limit of the count rate capability of a gamma camera (e.g. IGE XCT gamma camera). However, the reconstructed attenuation maps were very noisy. These images improved considerably when the initial number of photons in the external source was increased (corresponding to an increase in source activity). An activity of 1540.6 MBq (41.64 mCi) produced sharp images with considerably less noise. However, this activity would produce theoretical counting rates of approximately 240 kcps, a value that present gamma cameras cannot process. Similarly, it was calculated that an activity of 1540.6 MBq would produce a maximum counting rate of 40 kcps at any projection angle when imaging the thorax phantom. This value is within the limit of the count rate capability of the gamma camera.

To overcome counting rate problems while performing the blank study, several authors have suggested either to delay the acquisition of the blank image or to place a filter (e.g. copper or lead filter) between the collimated line source and the gamma camera (Jaszczak *et at* 1993, Ficaro *et al* 1994). This procedure should be such that the incident photon flux is reduced to an acceptable level.

The attenuation maps were calculated for two cases: primary and primary plus scattered photons. However, because the contribution of scattered photons into the projections was negligible (scatter fraction of the order of 3.6%) the attenuation maps were essentially equivalent. An example of a reconstructed transmission map is presented in figure 6.9. The finite detector spatial response produced blurred images with anatomic structure very difficult to perceive. Only the lungs and the muscular tissue were easily distinguishable from the rest of the tissues.

The attenuation coefficients for these two materials were calculated by selecting regions of interest in the lung and heart within the cross sectional images. Attenuation coefficients of 0.041 ± 0.002 cm^{-1} and 0.165 ± 0.002 cm^{-1} were obtained for lung and muscle, respectively, figures which are in agreement with theoretical values for narrow beam geometry (0.040 cm^{-1} and 0.161 cm^{-1}, respectively). A maximum attenuation coefficient in all the cross sectional images of 0.243 ± 0.008 cm^{-1} was obtained indicating the effect of partial volume in regions containing cortical and spongiosa tissues (the attenuation coefficient for cortical bone at 140 keV is 0.297 cm^{-1}).

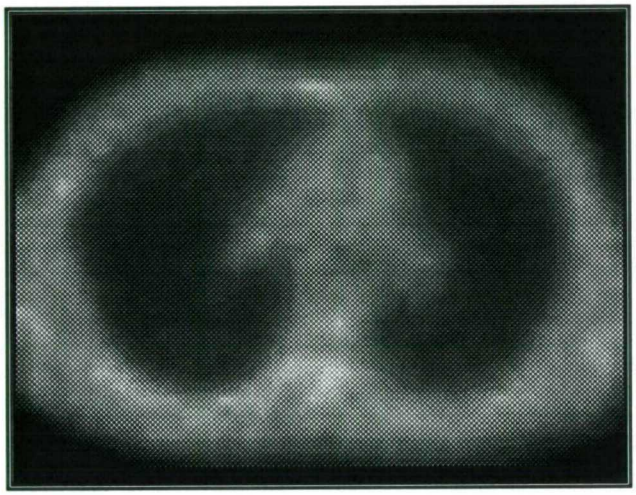

Figure 6.9. Typical attenuation map obtained with the Monte Carlo simulation of a transmission tomographic system. The image corresponds to the CT slice shown in figure 6.5.

6.4.2. Attenuation Maps for ^{201}Tl

Attenuation maps for ^{201}Tl were obtained directly from the data generated for ^{99m}Tc. A second order polynomial transformation of the form:

$$\mu_{^{201}Tl} = 0.012 + 0.752\mu_{^{99m}Tc} + 2.630\left(\mu_{^{99m}Tc}\right)^2 \qquad (6.4)$$

was applied to the ^{99m}Tc attenuation maps as suggested in Chapter 4, section 4.3.2. The coefficients in equation 6.4 were obtained using the results of the transmission study with a line source presented in table 4.4. To this end, the attenuation coefficients for 75 keV photons were plotted *versus* the attenuation coefficients for 140 keV. A quadratic regression algorithm provided the values shown in equation 6.4. It is important to note that because the thorax transmission study produced a scatter

fraction of less than 3.6%, only primary events generated with the collimated line source study were used. The attenuation coefficients for lung and muscle were also calculated from the ^{201}Tl attenuation maps by selecting regions of interest within the cross sectional images. Attenuation coefficients of $0.048 \pm 0.002\ cm^{-1}$ and $0.208 \pm 0.003\ cm^{-1}$ were obtained for lung and muscle, respectively, in agreement with the narrow beam values ($0.049\ cm^{-1}$ and $0.200\ cm^{-1}$, respectively). A maximum attenuation coefficient in all the cross sectional images of $0.343 \pm 0.010\ cm^{-1}$ was obtained indicating the effect of partial volume in regions containing cortical and spongiosa tissues (the attenuation coefficient for cortical bone at 75 keV is $0.465\ cm^{-1}$).

6.5. Results of the Emission Study

The number of photon histories simulated in the program was chosen so as to produce between one and two million detected events, summed over the 64 projections. This value is typical of a myocardial perfusion imaging examination. The same number of emitted photons was simulated for both energies 75 and 140 keV. For 308.7×10^6 photon histories the program produced the output shown in table 6.1. The ^{201}Tl study generated approximately 30% less primary photons than the ^{99m}Tc study. This substantial decrease in the number of primary events had an important effect in the reconstructed images, as will be shown in the next section.

Table 6.1. Output of the emission study using the anthropomorphic phantom.

Energy (keV)	Size of data file (MB)	CPU time[a] (hours)	Detected events ($\times 10^6$)	Scatter fraction
75	855	125	1.3	0.58
140	974	105	1.6	0.33

[a] Running on a Sun SPARCstation 10.

6.5.1. Analysis and Discussion

The Monte Carlo generated images are shown in figures 6.10 and 6.11 for the two photon energies and the three reconstruction algorithms: FBP with a Ramp-Hanning filter (cut-off frequency of 0.8 cycles/cm), ML-EM without attenuation compensation and ML-EM with attenuation compensation, separated in terms of primary and total events. The images correspond to the theoretical image shown in figure 6.8.

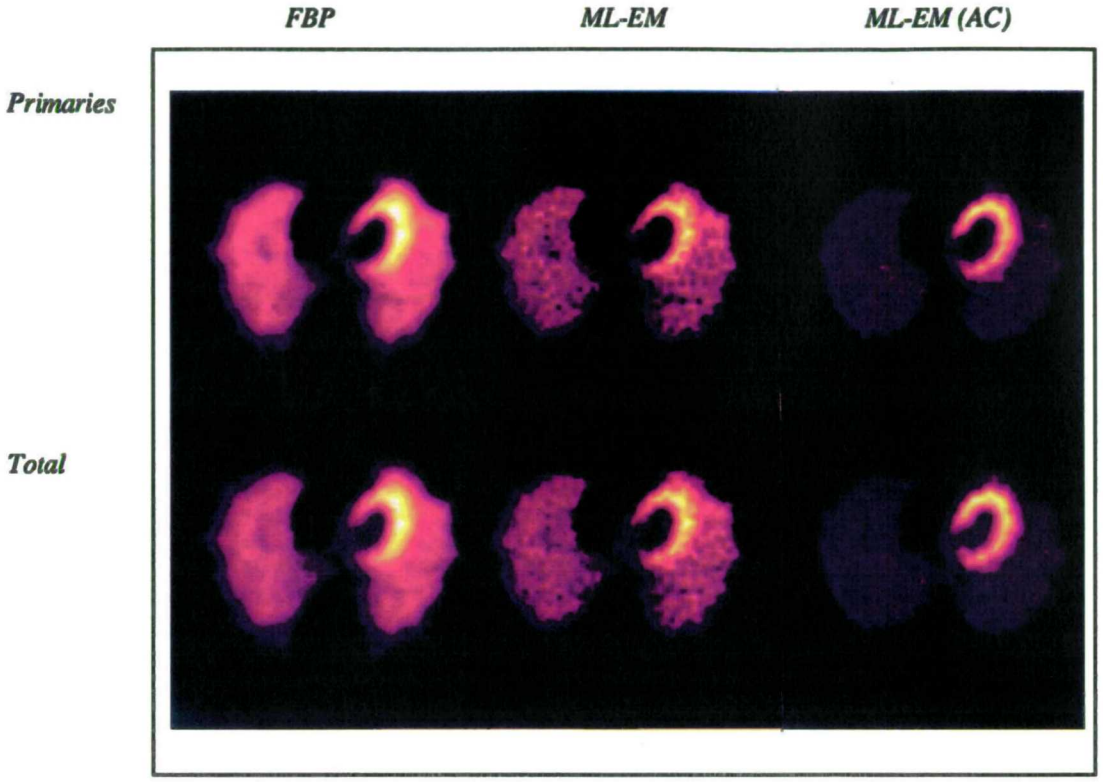

Figure 6.10. Monte Carlo results for the ^{201}Tl emission study.

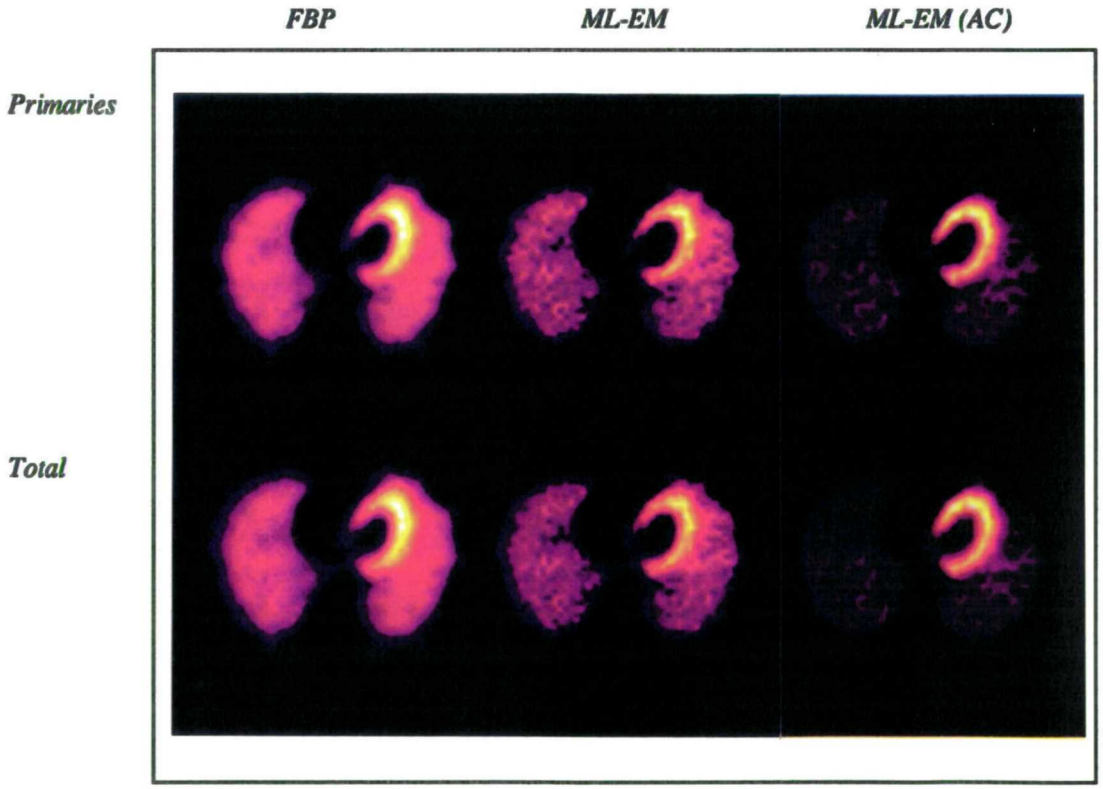

Figure 6.11. Monte Carlo results for the ^{99m}Tc emission study.

A qualitative examination of these images clearly shows that the ML-EM algorithm with attenuation compensation produced images with the highest quality, especially when using scatter-free data. The effect of scattered photons resulted in a degradation of the image quality by blurring the edges and reducing the image contrast. The FBP and the ML-EM without attenuation compensation algorithms produced equivalent images, although the FBP images generated smoother images due to effect of the filter. Another interesting feature of the ^{201}Tl images was due to the low number of primary events which resulted in large statistical fluctuations.

The image properties described above can be better investigated by examining a set of horizontal profiles (shown in figures 6.12 and 6.13) drawn across the myocardium. Each profile was normalised with respect to the maximum number of counts. The features of the profiles can be summarised as follows:

- ^{201}Tl images presented larger statistical fluctuations than ^{99m}Tc images due to the loss of primary photons through absorption and scatter in the thorax.
- The most important characteristic of the image profiles without attenuation compensation is that the number of counts in the lungs appear to be substantially higher than expected. There is also a decreased number of counts in the inner wall of the myocardium. These two artificial effects disappeared almost completely when attenuation compensation was performed.
- The presence of scattered photons in the reconstructed images produced a non-uniform background in regions where originally there was no activity at all. In spite of this, the quality of the images is substantially improved when attenuation correction is applied since the relative number of counts between the myocardium and lung is closer to the theoretical prediction.
- A comparison between the profiles generated with the ML-EM with attenuation correction (only primary events) and the theoretical prediction produced correlation coefficients of 0.989 and 0.992 for ^{201}Tl and ^{99m}Tc, respectively. The corresponding correlation coefficients for image profiles generated with primary plus scattered events were 0.961 and 0.974. The maximum correlation coefficient associated with the reconstructed images without attenuation compensation was 0.916. These values show that the ML-EM algorithm with attenuation compensation produced the best estimation of activity distributions when applied to scatter-free data.
- The corrected ^{99m}Tc images were of higher quality than the corresponding ^{201}Tl images.

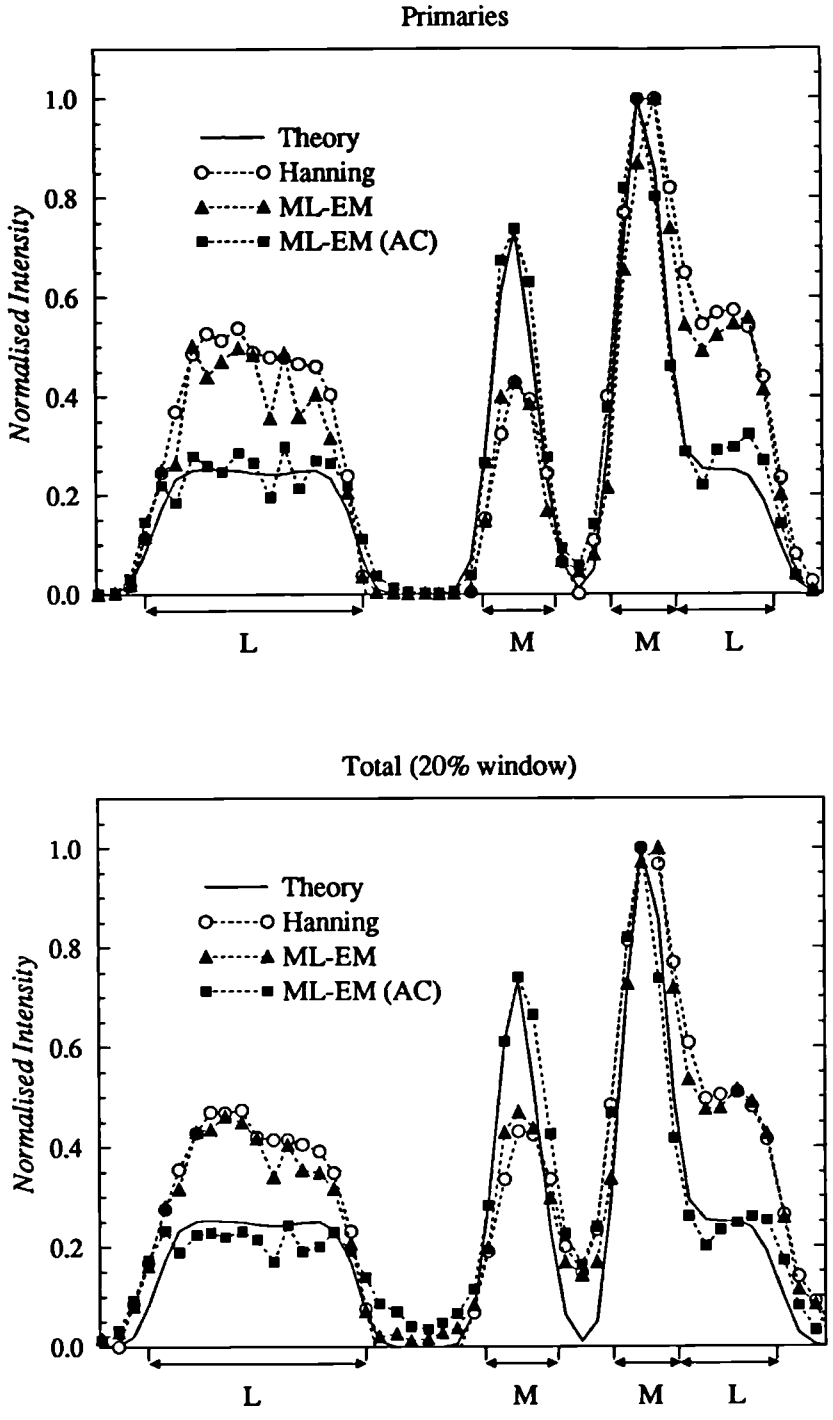

Figure 6.12. Profiles drawn across the theoretical prediction shown in figure 6.8 and the Monte Carlo ^{201}Tl images shown in figure 6.10. The symbols L and M represent lung and myocardium regions, respectively.

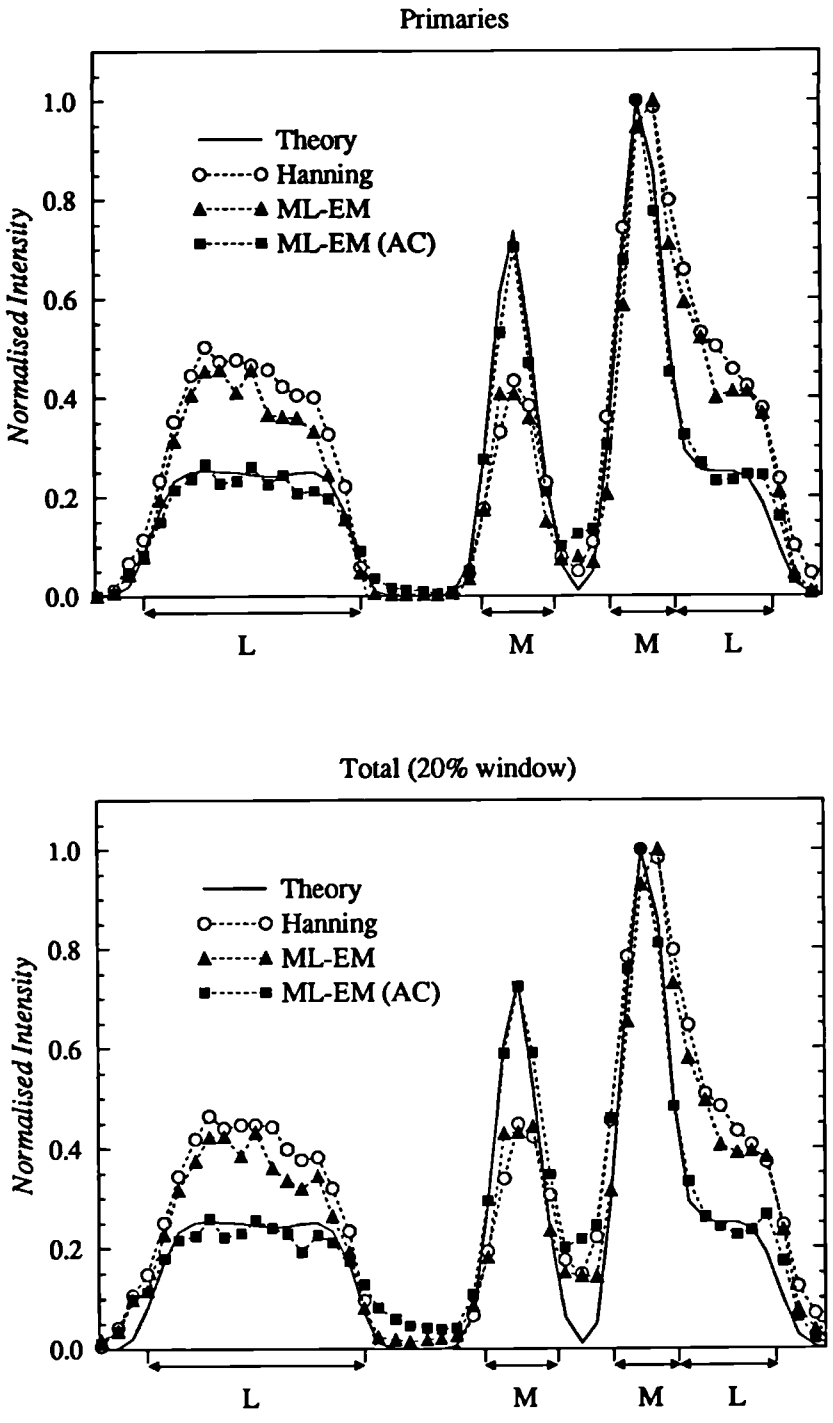

Figure 6.13. Profiles drawn across the theoretical prediction shown in figure 6.8 and the Monte Carlo ^{99m}Tc images shown in figure 6.11. The symbols L and M represent lung and myocardium regions, respectively.

6.6. Conclusions

This chapter presented the Monte Carlo simulation of a transmission-emission computed tomography system for a myocardial imaging examination with both thallium 201 and technetium 99m. The mathematical representation of the thorax enabled a realistic anatomic structure of the patient with appropriate myocardial and lung radionuclide uptakes to be simulated.

The transmission study produced narrow beam attenuation coefficients for ^{99m}Tc which were used together with the ML-EM algorithm to perform non-uniform attenuation compensation of an emission study with the same radionuclide. The attenuation maps for ^{201}Tl were produced through a second order polynomial transformation of the ^{99m}Tc attenuation maps, as given in Chapter 4. These attenuation coefficients showed an excellent agreement with theoretical values reported in table 4.4, Chapter 4. Emission data generated with ^{201}Tl were reconstructed with the ML-EM with non-uniform attenuation compensation.

Comparisons between the different reconstruction algorithms indicated that non-uniform attenuation compensation with the ML-EM algorithm substantially improved the quality of the images, particularly when applied to scatter free data. The Monte Carlo results showed that a large fraction of ^{201}Tl primary photons are attenuated before reaching the detector causing a decreased number of counts in the reconstructed images. This effect produced larger statistical fluctuations in the reconstructed images than the ^{99m}Tc images. It is then expected that the development of new ^{99m}Tc-labelled radiopharmaceuticals would considerably improve the quality of the images in cardiovascular nuclear imaging, since it would overcome this problem.

The simulation of the thorax presented in this chapter is a realistic mathematical representation of a human thorax; anatomic structure and tissue composition were modelled very accurately. However, the major disadvantage of the method is due to the large computing times and hard-disk storage required to perform either transmission or emission studies. If time is not a major limiting factor and disk space is available, many examinations can be studied with the Monte Carlo simulation technique presented in this chapter. This can be the subject of future work.

CHAPTER 7

Conclusions

The results obtained from a Monte Carlo simulation of an emission-transmission tomographic system based on a rotating gamma camera fitted with a parallel hole LEGP collimator and an external source have been presented in this thesis. Validations of the collimator program using theoretical and experimental methods indicated that the simulation produced reliable results. The experimental validation also indicated that the program could be used to simulate a realistic environment.

A transmission study using a non-uniform phantom and two different external sources, a flood source and a collimated line source, showed that the attenuation maps were highly dependent on the geometry and photon energy of the source. Attenuation coefficients for different media were measured in regions not affected by partial volume effects. Attenuation coefficients predicted with the collimated line source were very close to narrow beam attenuation coefficients whilst the flood source predicted smaller values. It was found that a non-linear relationship exists between attenuation coefficients and source energy for a range of substances. A second order polynomial transformation provided the best relationship between attenuation coefficients at different energies.

The attenuation coefficients generated in the transmission study were used to perform non-uniform attenuation compensation of an emission study. A source distribution consisting of a series of activity concentrations was simulated. The results showed that the ML-EM algorithm with non-uniform attenuation compensation significantly improved the quality of the data. Absolute quantification was feasible when applied to scatter-free data and when narrow beam attenuation coefficients were used during image reconstruction. Quantification was performed using the air sensitivity criterion indicating that the largest difference between the theoretical and the Monte Carlo reconstructed images was of the order of 8%.

The inclusion of scattered photons in the reconstructed images degraded the image quality. They produced an over-estimation of activity concentrations, particularly in regions of low activity, when narrow beam attenuation coefficients were used for non-uniform attenuation compensation. The use of effective attenuation coefficients during attenuation compensation produced both under-estimation and over-estimation in the number of counts in different regions of the images.

The Monte Carlo simulation of the thorax phantom showed that quantification in myocardial imaging is feasible. The ML-EM algorithm provided the best estimation of activity concentrations, once again, when using scatter-free data and narrow beam attenuation coefficients obtained with a collimated line source. In this case, comparison between the profiles generated with attenuation compensation and the theoretical prediction produced correlation coefficients of the order of 0.99. This is an indication of the capability of the attenuation compensation algorithm to produce quantitative data.

Non-uniform attenuation compensation of emission data contaminated with scattered photons produced a non-uniform background in cold regions. The comparison between the predicted and theoretical profiles produced correlation coefficients of the order of 0.96.

The quality of the emission images was highly dependent on the energy of the primary photons. Simulations of lung and myocardial uptake with ^{201}Tl and ^{99m}Tc (same activity in both cases) showed that the ^{201}Tl images had more statistical fluctuations than the ^{99m}Tc images, resulting in poorer image quality. The quadratic relationship suggested in Chapter 4 relating the attenuation coefficients at different energies was used in the thorax simulation to produce the attenuation maps for ^{201}Tl. Good agreement between the reconstructed source distributions with attenuation compensation and the theoretical prediction was observed, indicating that the suggested relationship is appropriate.

Non-uniform attenuation compensation with the ML-EM algorithm and narrow beam attenuation coefficients produced an excellent prediction of activity concentrations when applied to scatter-free data. The presence of scattered photons produced image blurring, extraneous activity in cold regions and an unpredictable over-estimation or under-estimation of activity concentrations. Partial volume effects also resulted in a deterioration of the image for small objects and precluded the accurate determination

of activity concentrations. Finally, statistical fluctuations in the reconstructed images degraded their quality. Clearly, quantification in SPECT imaging requires the simultaneous correction of all these factors.

The results presented in this thesis indicate that it is not possible to accomplish accurate attenuation correction in general situations where scatter correction is not applied.

7.1. Future Work

A number of suggestions could be made to extend the present work:

a) The Monte Carlo program allowed all the photon histories to be followed and permitted their classification in terms of the number and type of photon interaction within the patient. This could be used to assess the accuracy of scatter correction techniques.

b) The use of a highly collimated source in the determination of the attenuation maps is desirable due to its efficiency and minimum contribution of scattered radiation reaching the detector. High photon fluxes can be obtained using a very active source. However, a source of this kind is normally expensive and could cause count rate problems in the gamma camera. An investigation on the collimation of the line source can be performed in order to obtain an optimum performance at a reasonable cost.

c) An alternative method to produce the attenuation maps is to use tissue contours determined from the segmentation of a transmission scan. Different regions in the image are assigned with *a priori* determined attenuation coefficients. This method can be assessed with the Monte Carlo simulation. Also, the minimum requirements in the transmission scan to obtain an appropriate segmentation of the image can be investigated.

d) When ^{201}Tl is used in myocardial perfusion imaging it could be necessary to perform a transmission study with a higher photon energy to allow separation of the data. This situation could arise, for example, when performing a simultaneous emission-transmission protocol. In this case the high energy transmission photons could produce characteristic x-rays in the collimator material that could be detected in the ^{201}Tl window. Since the Monte Carlo code used in this study allows the production

and transport of characteristic x-ray photons, an investigation could be performed to assess the effect of these photons on the reconstructed images.

e) The Monte Carlo simulation of the thorax phantom required extremely large computing times, particularly for the transmission study. An optimisation of the program could be accomplished in two different ways:

- The image format of the original CT images was 128x128, whereas the Monte Carlo simulation generated images in a 64x64 format. A reduction in the resolution of the CT image would produce smaller number of regions and, therefore, a reduction in computing time. This would require the effect of reducing the CT image resolution on the emission and transmission studies to be investigated.
- The segmentation method applied to the CT images to produce the box representation can be optimised.

f) An important disadvantage of the thorax simulation is that the CT images did not provide sufficient sensitivity to differentiate between cardiac muscle and blood in the cavities of the heart. Because of this, the myocardium had to be drawn manually. This process was difficult and time consuming. An alternative option would be to combine magnetic resonance (MRI) and CT images. The MRI images could provide a detailed structure of the myocardium and the CT images the anatomic structure of the transverse section. This would require to register the images to correct for geometric (translation, rotation or scaling) and grey scale differences.

APPENDIX 1

Photon Interactions with Matter

When x-ray or γ-ray photons travel through matter, individual photons are removed (attenuated) from the primary beam of radiation by interactions with electrons, atoms or nuclei. This attenuation takes place by two competing processes: scattering and absorption. The probability of these processes depends strongly on both photon energy ($h\nu$) and the atomic number (Z) of the scattering medium. For nuclear medicine applications the choice of the radionuclide must fulfil certain physical requirements: the radionuclide must have a minimum of particulate emissions in order to minimise the dose to the patient, the half-life must be greater than the time required to prepare the material for injection, the energy of the emitted photons should be sufficiently high so as to penetrate through several centimetres of tissue and, at the same time, it should not be so high that it cannot be efficiently detected. In practice, γ-ray or x-ray emitters are chosen with photon energy emissions between 50 keV and 360 keV. For this energy range and low atomic number elements, three types of photon interactions predominate: photoelectric interaction, incoherent (or Compton) scattering and coherent (or Rayleigh) scattering.

A1.1. Photoelectric Effect

The photoelectric effect is the most important interaction of low-energy photons with matter, especially for high atomic number media. In this process the primary photon is totally absorbed by a bound atomic electron usually from the K or L shell. This electron is ejected with a kinetic energy E_k given by the difference between the energy of the primary photon and the binding energy of the electron involved. This type of interaction creates an ionised atom with a vacancy in one of its bound shells that is quickly filled through the rearrangement of electrons from other shells of the atom. In the process, the binding energy is liberated either in the form of a characteristic x-ray or Auger electron.

The theoretical derivation of the interaction cross section for the photoelectric effect is very difficult because of the complications arising from the electron binding energy. However, experiments indicate a dependence of the interaction cross section on the atomic number of the scattering medium and energy of the photons (Attix 1986). This dependence can be written as:

$$\tau_{photo} \propto \frac{Z^n}{(h\nu)^m} \tag{A1.1}$$

where: n≈4 at $h\nu = 0.1$ MeV, gradually rising to about 4.6 at 3 MeV,
m≈3 at $h\nu = 0.1$ MeV, gradually decreasing to about 1 at 5 MeV.

A1.2. Coherent (Rayleigh) Scattering

Coherent scattering involves the elastic collision of a photon with a bound electron. Because the electron is bound to the atom, the recoil momentum is absorbed by the entire atom. The atom is neither ionised nor excited; the energy of the scattered photon is essentially the same as that of the incident photon and no energy is deposited. This process is called coherent scattering and it is most prominent for low-energy photons scattered in high atomic number materials. The photon scattering angle depends on both the atomic number of the scattering medium and on the energy of the incident photon. The photon scattering angle is sampled from the differential cross section for coherent scattering for a molecule of the scattering medium:

$$\frac{d\sigma_{coh,m}}{d\Omega} = \frac{d\sigma_{Th,e}}{d\Omega} F_m^2(\upsilon^2) = \frac{1}{2} r_0^2 (1+\cos^2\theta) F_m^2(\upsilon^2) \tag{A1.2}$$

where: $r_0 = 2.818 \times 10^{-13}$ cm is the classical electron radius,

$d\Omega = 2\pi \sin\theta d\theta$ is the solid-angle element,

$\frac{d\sigma_{Th,e}}{d\Omega}$ is the Thompson differential cross section per electron,

$F_m^2(\upsilon^2)$ is the square of the form factor of a molecule

The form factor of a molecule accounts for the effect of wave interference between scattered photons from different electrons. The form factor of a molecule is obtained under the assumption that coherent cross sections of individual atoms combine independently and represent the probability that the Z electrons of the atom take up a

recoil momentum without absorbing any photon energy. The variable υ combines the dependence of the form factor on the scattering angle and the photon energy $h\nu$.

A1.3. Incoherent (Compton) Scattering

In materials of low atomic number, incoherent scattering is the most important interaction for photons of medium energies. In an incoherent scattering process, a photon collides with an atomic electron and imparts some of its energy and momentum to the struck electron. The incoming photon is deflected through a given angle with respect to its original direction. The fraction of energy which a photon transfers to the electron is a function of the scattering angle. Because all angles of scattering are possible, the energy transferred to the electron can vary from zero to a large fraction of the primary photon energy.

According to the kinematics of the Compton effect, a photon of energy hν collides with an unbound stationary electron imparting some of its energy. During the collision the electron acquires a kinetic energy T and starts travelling along a trajectory at angle θ relative to the incident photon's direction. The photon loses energy during the interaction and its trajectory is deviated from the original path an angle ϕ in the same scattering plane.

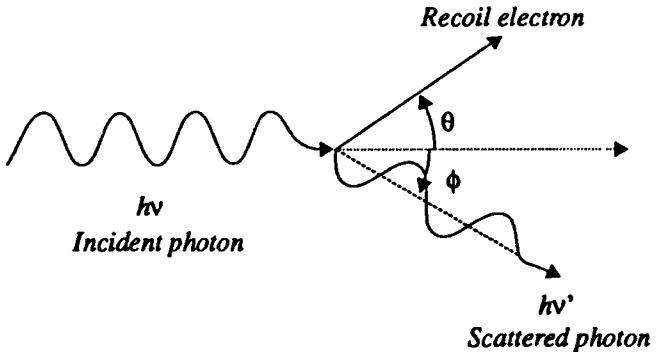

Figure A1.1. Kinematics of the Compton effect.

The energy of the scattered photon can be calculated using conservation of both energy and momentum and can be written as:

$$h\nu' = \frac{h\nu}{1+\frac{h\nu}{m_0c^2}(1-\cos\phi)} \qquad \text{(A1.3)}$$

where m_0c^2 is the rest mass of the electron. The kinetic energy carried by the electron is simply $T = h\nu - h\nu'$. The relationship between the scattering angles θ and ϕ is given by:

$$\cot(\theta) = \left(1 + \frac{h\nu}{m_0c^2}\right)\tan\left(\frac{\phi}{2}\right) \qquad \text{(A1.4)}$$

The angular distribution of the scattered photons is predicted by the Klein and Nishina formula. This can expressed as the collision differential scattering cross section per electron:

$$\frac{d_e\sigma}{d\Omega_\phi} = \frac{r_0}{2}\left(\frac{h\nu'}{h\nu}\right)^2\left(\frac{h\nu'}{h\nu} + \frac{h\nu}{h\nu'} - \sin^2\phi\right) \qquad \text{(A1.5)}$$

where r_0 is the classical electron radius, $h\nu$ is the energy of the primary photon, $h\nu'$ is the energy of the scattered photon, ϕ is the angle of deflection and $d\Omega_\phi$ is the solid-angle element.

A1.4. Total Attenuation Coefficient

When a photon interacts with matter, any of the previously described photon interactions can take place. Each of the interaction processes remove the photon from the beam either by absorption (photoelectric effect) or scatter (incoherent or coherent). The probability per unit path length that the photon is removed from a photon beam is given by the linear attenuation coefficient which can be expressed as the sum of the individual photon probabilities:

$$\mu = \tau_{photo} + \sigma_{incoh} + \sigma_{coh} \qquad \text{(A1.6)}$$

The number of transmitted photons I through an absorber of thickness t is given by Beer's law for the attenuation of the primary beam:

$$I = I_0e^{-\mu t} \qquad \text{(A1.7)}$$

where I_0 is the incident photon intensity. This equation applies only for absorbers with a single elemental composition and narrow beam geometry. Narrow beam geometry is defined as that geometry that does not allow the detection of scattered photons. This is normally achieved by collimating both the incident photon beam and the detector.

APPENDIX 2

The Monte Carlo Method

Any event that occurs randomly in a given physical process has associated with it a probability distribution. If this probability is known, then it is possible to simulate mathematically the physical process by making use of random number and sampling techniques. The Monte Carlo method is a numerical analysis technique that makes use of random sampling to solve a problem that depends on a certain probability law. A sequence of high quality random numbers in conjunction with the probability distributions that govern the phenomena under investigation simulate what occurs in nature (Raeside 1976). A random number sequence is said to be of high quality if its elements are distributed uniformly within the unit interval and if the sequence satisfies certain statistical criteria (Morin *et al* 1988). Three methods can be employed to obtain random numbers:

- drawing samples from tables,
- monitoring the output of some process or physical device,
- calculating samples with a mathematical algorithm.

The third method is referred to as a pseudo-random method since the production of random numbers is deterministic. This method is normally preferred due to the high quality of random numbers that some algorithms can produce and ease of implementation. Pseudo-random number generators have the characteristic of periodicity, that is, after a certain number of elements have been produced the sequence begins to repeat over again. It is then desirable that the periodicity of the random number generator is long enough to avoid correlation between the results.

In a Monte Carlo study of photon transport the most commonly used technique involves the simulation of each and every photon interaction. This "direct analogue" approach is reasonable for photons because the number of interactions to reduce their energy is relatively small (e.g. generally no more than 8 Compton interactions are needed to reduce the energy of a photon travelling in water from 140 keV down to

~100 keV). The approach is also justified because any electrons generated during the interaction of low energy photons are normally assumed to be absorbed at the location where they were generated. This is a valid assumption due to the short ranges of the electrons and their negligible bremsstrahlung production (Andreo 1991). For example, the range of a photoelectron produced by a photon of 140 keV in soft tissue is approximately 0.18 mm. This distance can be considered to be very small when compared with the size of a patient.

A2.1. Probability Density Function

The probability density function $f(x)$ of a continuous random variable X is a function whose integral from A to B $(B \geq A)$ gives the probability that X takes a value in the interval (A,B).

$$p(A \leq X \leq B) = \int_A^B f(x)dx \qquad \text{(A2.1)}$$

A probability density function (PDF) must satisfy two conditions:

i) $f(x) \geq 0$ for all the values of x (a probability cannot be negative by definition),

ii) $\int_{-\infty}^{\infty} f(x)dx = 1$

A2.2. Cumulative Probability Function

The cumulative probability function (CPF), $F(x)$, of a continuous random variable X with a PDF given by $f(x)$ is defined as:

$$F(x) = p(X \leq x) = \int_{-\infty}^{x} f(x')dx' \qquad \text{(A2.2)}$$

It follows from the properties of the probability density function that $0 \leq F(x) \leq 1$.

A2.3. Sampling Techniques

Two sampling techniques are normally used to select the value of a random variable based on its probability density function: inverse and rejection methods.

A2.3.1. Inverse (or Direct) Method

Let us assume that a random variable X has a PDF and a CPF represented by $f(x)$ and $F(x)$ $(A \leq x \leq B)$, respectively. The direct method seeks to invert the cumulative probability function $F(x)$ associated with the random variable X. The algorithm makes use of the fundamental inversion theorem that states that if a random number r^* is generated in the interval $0 \leq r^* \leq 1$ a random sample x^* $(A \leq x^* \leq B)$ can be obtained from the distribution $F(x)$ such that the PDF associated to x^* is $f(x^*)$ (Williamson 1988). The inversion of the CPF may be analytical or numerical. Figure A2.1 shows the concepts of PDF, CPF and how the selection of a random number r^* $(0 \leq r^* \leq 1)$ can generate a random sample x^* $(A \leq x^* \leq B)$.

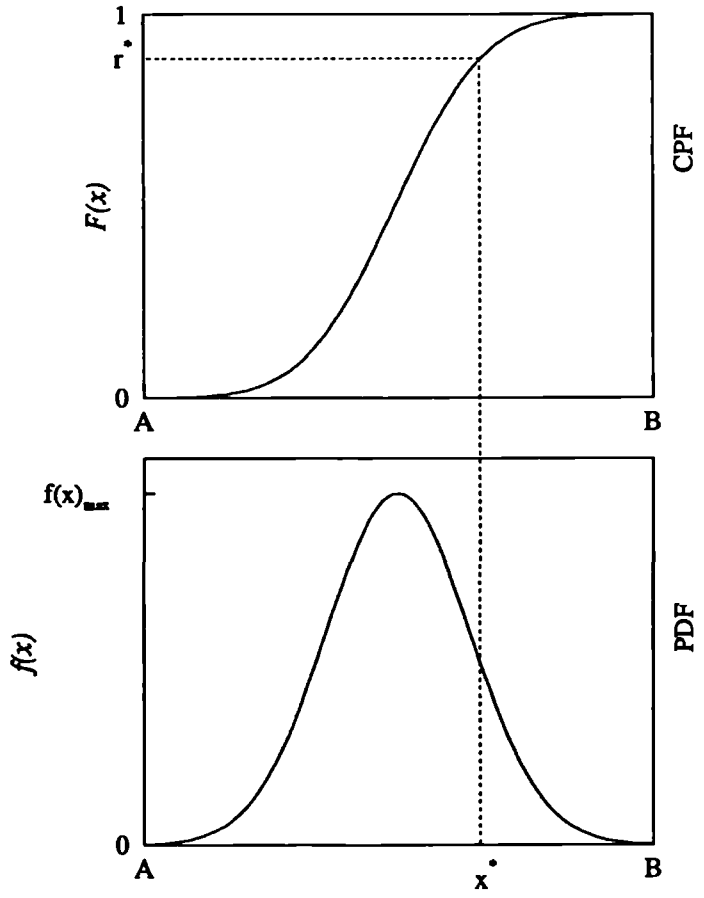

Figure A2.1. The sampling of a random variable x^* with PDF $f(x)$, can be carried out with the inversion of its CPF, $F(x)$.

The simplest and probably the most relevant example of direct sampling in photon transport is the selection of the distance to the next photon interaction (free path length). The probability that a photon travels a distance x ($x \geq 0$) without suffering an interaction is given by:

$$e^{-\mu x} \tag{A2.3}$$

where μ is the linear attenuation coefficient for the appropriate photon energy and composition of the attenuating medium. The probability that a photon interacts within a layer of thickness Δx a distance x from its origin is

$$\mu e^{-\mu x} \Delta x \tag{A2.4}$$

The CPF is generated in the following manner

$$F(x) = \int_0^x \mu e^{-\mu x'} dx' = 1 - e^{-\mu x} \tag{A2.5}$$

The inversion of equation A2.5 is simply

$$x = -\frac{1}{\mu} \ln(1 - F(x)) \tag{A2.6}$$

Therefore, the selection of the free path length reduces to the generation of random numbers r^* and selecting values of x such that

$$x = -\frac{1}{\mu}\left(1 - r^*\right) \tag{A2.7}$$

A2.3.2. Rejection Method

The idea behind the rejection sampling technique is fairly simple. Let us assume that a random variable has a PDF given by $f(x)$, $(A \leq x \leq B)$, and that it reaches its maximum value at $f(x)_{max}$. The technique requires the generation of two random numbers r_1^* and r_2^* within the unit interval. A random variable x^* (which is contained in the x-region of interest between A and B) is calculated in the following manner:

$$x^* = A + (B - A) \cdot r_1^* \tag{A2.8}$$

If the point (x^*,r_2^*) lies below the normalised PDF $f(x^*)/f(x)_{max}$, that is, if $r_2^* \leq f(x^*)/f(x)_{max}$, then x^* is accepted as a successful event, otherwise it is rejected. The rejection method technique is illustrated in figure A2.2.

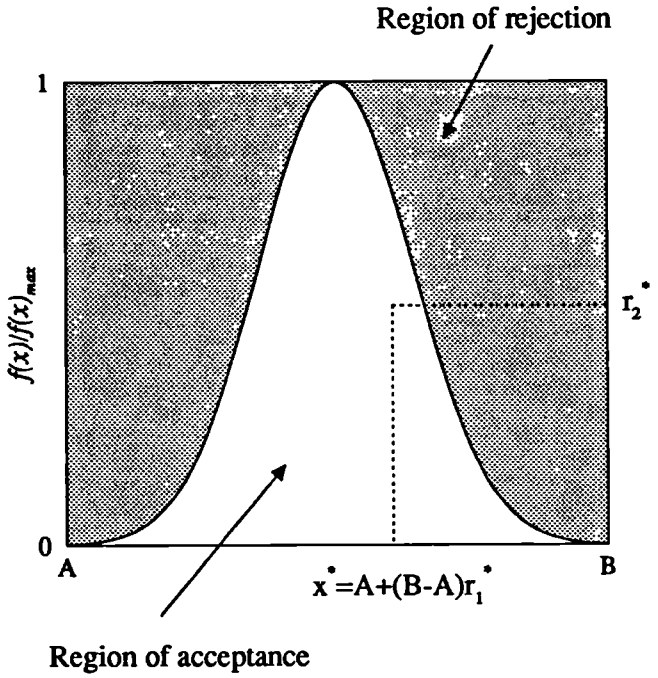

Figure A2.2. Illustration of the rejection technique.

A2.4. The Electron-Gamma-Shower Code (EGS4)

The Electron-Gamma-Shower (EGS) Monte Carlo system was developed to study coupled electron and gamma transport problems for high energy physics applications. However, a growing need to extend the lower energy limits led to the development of the current version, the EGS4 code system (Nelson *et al* 1985). EGS is an analogue Monte Carlo program in which the radiation transport of electrons, positrons and photons can be simulated in any element, compound or mixture. EGS follows each individual charged particle or photon until either it is absorbed, escapes from the system geometry or its energy falls below a given cut-off energy. During the course of particle transport, the step size, energy loss, interaction type, energy and angle of the emerging particle from an interaction are sampled by EGS from appropriate probability distributions and other relevant physical data.

The EGS Code System requires a driver program written in a FORTRAN-like structured language called Mortran3. The driver program is most commonly referred to as an EGS user code. The user code generally consists of a MAIN routine, and two subroutines: AUSGAB and HOWFAR. The purpose of MAIN is to set up various initialisations and to bring in the various media data created at an earlier time by a pre-processor called PEGS. The pre-processor PEGS computes various physical quantities using theoretical and empirical formulae and prepares them to be used in an efficient way by EGS. AUSGAB must be written in order to obtain output results from EGS during the simulation and HOWFAR is required in order to provide information to EGS about the geometry of the system. An interesting characteristic of the EGS code is that it provides subroutines that allow creation of relatively sophisticated geometries. It contains subprograms to calculate the intersection of a given trajectory with planes, cylinders (circular or elliptical in cross section), spheres, cones and a series of combinations of these geometries.

EGS uses a pseudo-random number generator developed by Marsaglia *et al* (1990). It has a period of $2^{144} \approx 2 \times 10^{43}$, it is completely portable (that is, it generates exactly the same sequence of numbers on different machines) and generates 32 bit floating-point numbers in the range from zero to one, excluding one.

References

Andreo P 1991 Monte Carlo Techniques in Medical Radiation Physics *Phys. Med. Biol.* **36** 861-920

Anger H O 1958 Scintillation Camera *Rev. Sci. Instrum.* **29** 27-33

Anger H O 1964 Scintillation Camera with Multichannel Collimators *J. Nucl. Med.* **5** 515-531

Appledorn C R, Oppenheim B E, and Wellman H N 1980 An Automated Method for the Alignment of Image Pairs *J. Nucl. Med.* **21** 165-167

Attix F H 1986 *Introduction to Radiological Physics and Radiation Dosimetry* (New York: Wiley) pp 124-157

Axelsson B, Israelsson A and Larsson S A 1987 Studies of a Technique for Attenuation Correction in Single Photon Emission computed Tomography *Phys. Med. Biol.* **32** 737-749

Bailey D L, Hutton B F and Walker P J 1987 Improved SPECT Using Simultaneous Emission and Transmission Tomography *J. Nucl. Med.* **28** 844-851

Bailey D L and Hutton B F 1988 Simultaneous Emission and Transmission Tomography *Information Processing in Medical Imaging* eds C N de Graaf and M A Viergever (New York: Plenum Press) pp 559-575

Barrett H H and Swindell W 1981 *Radiological Imaging: The Theory of Image Formation, Detection and Processing* (New York: Academic Press)

Beck R N and Redtung L D 1985 Collimator Design Using Ray-Tracing Techniques *IEEE Trans. Nucl. Sci.* **32**-1 865-869

Bo W J, Wolfman N T, Krueger W A and Meschan I 1990 *Basic Atlas of Sectional Anatomy with Correlated Imaging* (Philadelphia: Saunders)

Budinger T F, Derenzo S E, Gullberg G T, Greenberg W L and Huesman R H 1977 Emission Computer Assisted Tomography with Single-Photon and Positron Annihilation Photon Emitters *J. Comp. Assist. Tomog.* **1** 131-145

Budinger T F, Gullberg G T and Huesman R H 1979 Emission Computed Tomography *Image Reconstruction from Projections* ed G T Herman (Berlin: Springer Verlag) pp 147-246

Budinger T F 1980 Physical Attributes of Single-Photon Tomography *J. Nucl. Med.* **21**-6 579-592

Budinger T F and Gullberg G T 1974 Three-Dimensional Reconstruction in Nuclear Medicine Emission Imaging *IEEE Trans. Nucl. Sci.* **21** 2-20

Cao Z J and Tsui B M W 1992 Performance Characteristics of Transmission Imaging Using a Uniform Sheet Source with Parallel-Hole Collimation *Med. Phys.* **19** 1205-1212

Chan H and Doi K 1988 Monte Carlo Simulation in Diagnostic Radiology *Monte Carlo Simulation in The Radiological Sciences* ed R L Morin (Boca Raton FL: CRC Press) pp 103-191

Chang L T 1978 A Method for Attenuation Correction in Radionuclide Computed Tomography *IEEE Trans. Nucl. Sci.* **25** 638-643

Cho Z A, Ahn I, Bohm C and Huth G 1974 Computerized Image Reconstruction: Methods with multiple Photon/X-ray Transmission Scanning *Phys. Med. Biol.* **19** 511-522

Datz F L, Gullberg G T, Zeng G L, Tung C H, Christian P E, Welch A and Clack R 1994 Application of Convergent-Beam Collimation and Simultaneous Transmission Emission Tomography to Cardiac Single-Photon Emission Computed Tomography *Seminars in Nuclear Medicine* **24** 17-37

DePuey E G and Garcia E V 1989 Optimal Specificity of Thallium-201 SPECT Through Recognition of Imaging Artifacts *J. Nucl. Med.* **30** 441-449

deVries D J, Moore S C, Zimmerman RE, Mueller SP, Friedland B and Lanza RC 1990 Development and Validation of a Monte Carlo Simulation of Photon Transport in an Anger Camera *IEEE Trans. Med. Imag.* **9** 430-438

Eichling J O, Higgins C S and Ter-Pogossian M M 1977 Determination of Radionuclide Concentrations with Positron CT Scanning (PETT): Concise Communication *J. Nucl. Med.* **18** 845-847

Elliott A T, Short M D and Barnes K J 1986 *Performance Assessment of Gamma Cameras-Part IV* Report STB/86/9 Department of Health and Social Security, London

Evans R D 1968 X-ray and γ-ray Interactions *Radiation Dosimetry* eds F H Attix and W C Roesch Vol. 1 Chap. 3 (New York: Academic Press)

Ficaro E P, Jeffrey J A, Rogers W L and Schwaiger M 1994 Comparison of Americium-241 and Technetium-99m as Transmission Sources for Attenuation Correction of Thallium-201 SPECT Imaging of the Heart *J. Nucl. Med.* **35** 652-663

Floyd C E, Jaszczak R J, Harris C C and Coleman R E 1984 Energy and Spatial Distribution of Multiple Order Compton Scatter in SPECT: A Monte Carlo Investigation *Phys. Med. Biol.* **29** 1217-1230

Floyd C E, Jaszczak R J, Greer K L and Coleman R E 1986 Inverse Monte Carlo as a Unified Reconstruction algorithm for ECT *J. Nucl. Med.* **27** 1577-1585

Floyd C E, Jaszczak R J and Coleman RE 1988 Scatter Detection in SPECT Imaging: Dependence on Source Depth, Energy and Energy Window *Phys. Med. Biol.* **33** 1075-1081

Frey E C, Tsui B M W and Perry J R 1992 Simultaneous Acquisition of Emission and Transmission Data for Improved Thallium-201 Cardiac SPECT Imaging Using a Technetium-99m Transmission Source *J. Nucl. Med.* **33** 2238-2245

Galt J R, Cullom S J and Garcia E V 1992 SPECT Quantification: A Simplified Method of Attenuation and Scatter Correction for Cardiac Imaging *J. Nucl. Med.* **33-12** 2232-2237

Gilland D R, Jaszczak R J, Turkington T G, Greer K L and Coleman R E 1991 Quantitative SPECT Imaging with Indium-111 *IEEE Trans. Nucl. Sci.* **38** 761-766

Gillen G J 1992 A Simple Method for the Measurement of Local Statistical Noise Levels in SPECT *Phys. Med. Biol.* **37** 1573-1579

Gonzalez R C and Wintz P 1987 *Digital Image Processing*, Adison Wesley (Reading MA: Adisson Wesley) pp 423-428

Gray H 1988 *Anatomy, Descriptive and Surgical* eds T P Pick and R Howden (New York: Galley Press) pp 460-471

Gullberg G T, Huesman R H, Malko J A, Pelc N J and Budinger T F 1985 An Attenuated Projector-Backprojector for Iterative SPECT Reconstruction *Phys. Med. Biol.* **30** 799-816

Gullberg G T, Zeng G L, Datz F L, Christian P E, Tung C H and Morgan H T 1992 Review of Convergent Beam Tomography in Single Photon Emission Computed Tomography *Phys. Med. Biol.* **37** 507-534

Harris C C, Greer K L, Jaszczak R J, Floyd C E, Fearnow E C and Coleman R E 1984 Tc-99m Attenuation Coefficients in Water-Filled Phantoms Determined with Gamma Cameras *Med. Phys.* **11** 681-685

Harrison N E 1993 The Effects of Collimation on Image Formation in Anger Gamma Cameras *PhD Thesis* University of London

Hoffman E J, Huang S C and Phelps M E 1979 Quantitation in Positron Emission Computed Tomography: 1. Effects of Object Size *J. Comput. Assist. Tomogr.* **3** 299-308

Hounsfield G N 1973 Computerized Transverse Axial Scanning (Tomography) Part 1: Description of System *Br. J. Radiol.* **46** 1016-1022

Huesman R H, Gullberg G T, Greenberg W L and Budinger T F 1977 *RECLBL Library Users Manual-Donner Algorithms for Reconstruction Tomography* Lawrence Berkeley Laboratory Publication PUB 214

Jarritt P H and Ell P J 1984 *Gamma Camera Emission Tomography: Quality Control & Clinical Applications* (Oxford : Alden Press) pp 64-78

Jaszczak R J, Li J, Wang H and Coleman R E 1992 Three-dimensional SPECT Reconstruction of Combined Cone Beam and Parallel Beam Data *Phys. Med. Biol.* **37** 535-548

Jaszczak R J, Gilland D R, Hanson M W, Jang S, Greer K L and Coleman R E 1993 Fast Transmission CT for Determining Attenuation Maps Using a Collimated Line Source, Rotatable Air-Copper-Lead Attenuators and Fan-Beam Collimation *J. Nucl. Med.* **34** 1577-1586

Kay D B and Keyes J W 1975 First Order Correction for Absorption and Resolution *J. Nucl. Med.* **16** 540-541

King M A, Glick S J and Penney B C 1991 Activity Quantitation in SPECT: A Comparison of Three Attenuation Correction Methods in Combination with Pre-Reconstruction Restoration Filtering *IEEE Trans. Nucl. Sci.* **38-2** 755-760

Knešaurek K, King M A, Glick S J and Penney B C 1989 Investigation of Causes of Geometric Distortion in 180° and 360° Angular Sampling in SPECT *J. Nucl. Med.* **30** 1666-1675

Knoll G F 1989 *Radiation Detection and Measurements* (New York: Wiley) pp 287-336

Lalush D S and Tsui B M W 1993 MAP-EM and WLS-MAP-CG Reconstruction Methods for Transmission Imaging in Cardiac SPECT *Conference Record of the 1993 Nuclear Science Symposium*, San Francisco, California, in press

Lang T F, Hasegawa B H, Liew S C, Brown J K, Blankespoor S C, Reilly S M, Gingold E L and Cann C E 1992 Description of a Prototype Emission-Transmission Computed Tomography Imaging System *J. Nucl. Med.* **33** 1881-1887

Lange J and Carson R 1984 EM Reconstruction Algorithms for Emission and Transmission Tomography *J. Comput. Assist. Tomogr.* **8** 306-316

Larsson S A, Kimiaei S and Ribbe T 1993 Simultaneous SPECT and CT with Shutter Controlled Radionuclide Sources and Parallel Collimator Geometry *IEEE Trans. Nucl. Sci.* **40** 1117-1122

Liow J S and Strother S C 1991 Practical Tradeoff Between Noise, Quantitation and Number of Iterations for Maximum Likelihood-Based Reconstructions *IEEE Trans. Med. Imag.* **10** 563-571

Ljungberg M and Strand S E 1990a Attenuation Correction in SPECT Based on Transmission Studies and Monte Carlo Simulations of Build-Up Functions *J. Nucl. Med.* **31** 493-500

Ljungberg M and Strand S E 1990b Scatter and Attenuation Correction in SPECT Using Density Maps and Monte Carlo Simulated Scatter Functions *J. Nucl. Med.* **31** 1560-1567

Maddahi J, Kiat H and Berman D S 1991 Myocardial Perfusion Imaging with Technetium-99m-Labeled Agents *Am. J. Cardiol.* **67** 27D-34D

Madsen M T, Kirchner P T, Edlin J P, Nathan MA and Kahn D 1993 An Emission-Based Technique for Obtaining Attenuation correction Data for Myocardial SPECT Studies *Nucl. Med. Commun.* **14** 689-695

Mahmood S, Buscombe J R and Ell P J 1992 The Use of Thallium-201 Lung/Heart Ratios Eur. *J. Nucl. Med.* **19** 807-814

Malko J A, Van Heertum R L, Gullberg G T and Kowalsky W P 1986 SPECT Liver Imaging Using an Iterative Attenuation Correction Algorithm and an External Flood Source *J. Nucl. Med.* **27** 701-705

Manfredotti C, Nastasi U, Marchisio R, Ongaro C, Gervino G, Ragona R, Anglesio S and Sannazzari G 1990 Monte Carlo Simulation of Dose Distribution in Electron Beam Radiotherapy Treatment Planning *Nucl. Ins. Meth.* **A291** 646-654

Manglos S H, Thomas F D, Gagne G M and Hellwig B J 1993 Phantom Study of Breast Tissue Attenuation in Myocardial Imaging *J. Nucl. Med.* **34** 992-996

Manglos S H, Floyd C E, Jaszczak R J, Greer K L, Harris C C and Coleman R E 1987a Experimentally Measured Scatter Fractions and Energy Spectra as a Test of Monte Carlo Simulations *Phys. Med. Biol.* **32** 335-343

Manglos S H, Jaszczak R J, Floyd C E, Hahn L J, Greer K L and Coleman R E 1987b Nonisotropic Attenuation in SPECT: Phantom Tests of Quantitative Effects and Compensation Techniques *J. Nucl. Med.* **28** 1584-1591

Manglos S H, Bassano D A, Thomas F D and Grossman Z D 1992 Imaging of the Human Torso Using Cone-Beam Transmission CT Implemented on a Rotating Gamma Camera *J. Nucl. Med.* **33** 150-156

Marchand E W 1964 Derivation of the Point Spread Function from the Line Spread Function *J. Opt. Soc. Am.* **54** 915-919

Marsaglia G, Zaman A and Tsang W W 1990 Toward a Universal Random Number Generator *Stat. Prob. Lett.* **9** 35-39

Meikle S R, Dahlbom M and Cherry S R 1993 Attenuation Correction Using Count-Limited Transmission Data in Positron Emission Tomography *J. Nucl. Med.* **34** 143-150

Mettler F A and Guiberteau M J 1991 *Essentials of Nuclear Medicine Imaging* (Philadelphia : W. B. Saunders) pp 95-140

Metz C E, Atkins F B and Beck R N 1980 The Geometric Transfer Function Component for Scintillation Camera Collimators with Straight Parallel Holes *Phys. Med. Biol.* **25** 1059-1070

Moore S C, Kouris K and Cullum I 1992 Collimator Design for Single Photon Emission Tomography Eur. *J. Nucl. Med.* **19** 138-150

Moore S C 1982 Attenuation Compensation *Computed Emission Tomography* eds P J Ell and B L Holman (Oxford : University Press) pp 339-360

Morin R L, Raeside D E, Goin J E and Widman J C 1988 Random Number Generation and Testing *Monte Carlo Simulation in the Radiological Sciences* ed R L Morin (Boca Raton FL: CRC Press) pp 103-192

Muehllehner G 1985 Effect of Resolution Improvement on Required Count Density in ECT Imaging: A computer Simulation *Phys. Med. Biol.* **30** 163-173

Muehllehner G and Luig H 1973 Septal Penetration in Scintillation Camera Collimators *Phys. Med. Biol.* **18** 855-862

National Electrical Manufacturers' Association 1980 *Standards for Performance Measurements of Scintillation Cameras*, NEMA, USA

Nelson W R, Rogers D W O and Hirayama H 1985 *The EGS4 Code System* Stanford Linear Accelerator Center Report SLAC-265

Plummer D L 1992 DispImage a Display and Analysis Tool for Medical Images *Rivista Di Neuroradiologica* **5** 489-495

Pratt W K 1974 Correlation Techniques for Image Registration *IEEE Trans. Aeros. Elec. Syst.* **10** 353-358

Radon J 1917 Über die Bestimmung von Funktionen durch ihre Integralwerte längs gewisser Mannigfaltigkeiten *Ber. Verh. Sachs. Akad. Wiss.* **69** 262-277

Raeside D E 1976 Monte Carlo Principles and Applications *Phys. Med. Biol.* **21** 181-197

Rosenfeld A and Kak A C 1982 *Digital Picture Processing* (New York: Academic Press)

Rosenthal M S and Henry L J 1990 Scattering in Uniform Media *Phys. Med. Biol.* **35** 265-274

Rossmann K 1969 Point Spread Function, Line Spread Function and Modulation Transfer Function: Tools for the Study of Imaging Systems *Radiology* **93** 257-272.

Rowe R W, Merhige M E, Bendriem B and Gould K L 1988 Regions of Interest Determination for Quantitative Evaluation of Myocardial Ischemia from PET Images *Information Processing in Medical Imaging* eds C N de Graaf and M A Viergerer (New York: Plenum Press) pp 591-600

Sharp P F, Dendy P P and Keyes W I 1985 *Radionuclide Imaging Techniques* (London: Academic Press)

Shepp L A and Vardi Y 1982 Maximum Likelihood Reconstruction for Emission Tomography *IEEE Trans. Med. Imag.* **1** 113-122

Snyder D L, Miller M I, Thomas L J and Politte D G 1987 Noise and Edge Artifacts in Maximum-Likelihood Reconstructions for Emission Tomography *IEEE Trans. Med. Imag.* **6** 228-238

Sorenson J A and Phelps M E 1987 *Physics in Nuclear Medicine* (Philadelphia: Saunders)

Storm E and Israel H I 1970 Photon Cross Sections from 1 keV to 100 MeV for Elements Z=1 to 100 *Nuclear Data Tables* A7 565

Svedlow M, McGillem C D and Anuta P E 1978 Image Registration: Similarity Measure and Preprocessing Method Comparison *IEEE Trans. Aeros. Elec. Syst.* **14** 141-149

Tan P, Bailey D L, Meikle S R, Eberl S, Futon R R and Hutton B F 1993 A Scanning Line Source for Simultaneous Emission and Transmission Measurements in SPECT *J. Nucl. Med.* **34** 1752-1760

Tsui B M W, Zhao X, Frey E C and McCartney W H 1994 Quantitative Single-Photon Emission Computed Tomography: Basics and Clinical Considerations *Seminars in Nuclear Medicine* **24** 38-65

Tsui B M W, Hu H B, Gilland D R and Gullberg G T 1988 Implementation of Simultaneous Attenuation and Detector Response Correction in SPECT *IEEE Trans. Nucl. Sci.* **35** 778-783

Tsui B M W, Gullberg G T, Edgerton E R, Ballard J G, Perry J R, McCartney W H and Berg J 1989 Correction of Nonuniform Attenuation in Cardiac SPECT Imaging *J. Nucl. Med.* **30** 497-507

Tsui B M W and Gullberg G T 1990 The Geometric Transfer Function for Cone and Fan Beam Collimators *Phys. Med. Biol.* **35** 81-93

Venot A, Lebruchec J F and Roucayrol J C 1984 A New Class of Similarity Measures for Robust Image Registration *Computer Vision, Graphics and Image Processing* **28** 176-184

Venot A, Liehn J C, Lebruchec J F and Roucayrol 1986 Automated Comparison of Scintigraphic Images *J. Nucl. Med.* **27** 1337-1342

Webb S, Flower M A, Ott R J and Leach M O 1983 A Comparison of Attenuation Correction Methods for Quantitative Single Photon Emission Computed Tomography *Phys. Med. Biol.* **28** 1045-1056

Williamson J F 1988 Monte Carlo Simulation in Diagnostic Radiology *Monte Carlo Simulation in the Radiological Sciences* ed R L Morin (Boca Raton FL: CRC Press) pp 53-102

Woodard H Q and White DR 1986 The Composition of Body Tissues *Br. J. Radiol.* **59** 1209-1219

Yanch J C, Dobrzeniecki A B, Ramanathan C and Behrman R 1992 Physically Realistic Monte Carlo Simulation of Source, Collimator and Tomographic Data Acquisition for Emission Computed Tomography *Phys. Med. Biol.* **37** 853-870

Yanch J C and Dobrzeniecki A B 1993 Monte Carlo Simulation in SPECT: Complete 3D Modeling of Source, Collimator and Tomographic Data Acquisition *IEEE Trans. Nucl. Sci.* **40** 198-203

Zeng G L, Gullberg G T, Tsui B M W and Terry J A 1991 Three-Dimensional Iterative Reconstruction Algorithms with Attenuation and Geometric Point Spread Response Correction *IEEE Trans. Nucl. Sci.* **38** 693-702